Technical Physics Letters, Vol. 27, No. 8, 2001, pp. 619–621. Translated from Pis'ma v Zhurnal Tekhnicheskoĭ Fiziki, Vol. 27, No. 15, 2001, pp. 1–8.

High-Speed Plasma Jet Modification and Doping of α-Fe

A. D. Pogrebnyak*, Yu. N. Tyurin, and A. P. Kobzev*****

** Institute of Surface Modification, Sumy, Ukraine*

*** Paton Institute of Electric Welding, National Academy of Sciences of Ukraine, Kiev, Ukraine*

**** Joint Institute for Nuclear Research, Dubna, Moscow oblast, 141980 Russia*

In final form received March 20, 2001

Abstract—Iron (α-Fe) samples were treated in a high-speed (up to 6 km/s) pulsed plasma jet using a plasmatron with a consumable (eroded) Mo electrode operated in specially selected regimes. As the number of jet pulses increases, the concentration of Mo within a 10-μm-thick surface layer of α-Fe varies in a nonmonotonic manner. In a 2-μm-thick layer, the oxygen content increases up to 50 at.%, while the concentrations of carbon and nitrogen do not exceed 10 at.%. The plasma jet treatment leads to the formation of a bcc Fe phase and the Fe_7Mo_6 and FeMo intermetallic phases in the surface layer. Doping the surface iron layer with molybdenum, as well as the formation of oxides and carbides, results in a 2.5-fold increase in the hardness of samples and in a decrease of wear under dry friction conditions. © *2001 MAIK "Nauka/Interperiodica".*

In recent years, the working characteristics of metals and alloys have been frequently improved by processing articles in pulsed beams of charged particles [1–4] or plasma [5–7]. Such treatments involve the rapid heating of the surface metal layer with a fast heat transfer into the bulk of the target (this is equivalent to quenching) and lead to the formation of disperse nanoinclusions, metastable phases, amorphous layers, etc. [4–5]. The concentrated fluxes of energy are typically provided by laser, electron, and ion beams, as well as by plasma flows [1–7].

In addition to the energy fluxes of these types, the solid surfaces can be subjected to detonation or plasma-detonation processing [6–9]. This process also improves the mechanical characteristics of articles made of metals and alloys. For this purpose, we designed and constructed a plasmatron (Fig. 1) comprising a detonation chamber *1* (featuring the formation of an inflammable gas mixture and the initiation of the detonation combustion), central electrode (anode) *2*, cone-shaped electrode (cathode) *3*, interelectrode gap *4*, consumable electrode *5*, and an electric power supply unit *6*.

The system operation is as follows. The inflammable gas mixture components are admitted into chamber *1*, from which the combustion products enter the interelectrode gap *4* to close the electric circuit of power source *6*. This results in the formation of a conducting gas column *7* composed of the combustion products. Particles in this column are accelerated by the gasodynamic and electromagnetic forces. A consumable metal rod *5* is mounted on the axis of the central electrode *2*; heating of this rod leads to evaporation of the doping elements from the rod tip. The evaporated dopants enter the plasma jet *8* ejected from the plasmatron to close the electric circuit between the central electrode (anode) and the surface of a processed article (cathode) *9*. The electric current passing in this circuit heats the plasma by supplying the Joule heat $Q = \sigma E^2$ (W/m^3). Gaseous dopants are introduced immediately into the interelectrode gap of the plasmatron.

At the first instant, the article surface experiences an elastic-detonation action of the shock wave and pulsed plasma jet, which is followed by the action of the electric current. The current (with an amplitude of 5 kA) gives rise to a magnetic field with a strength of up to

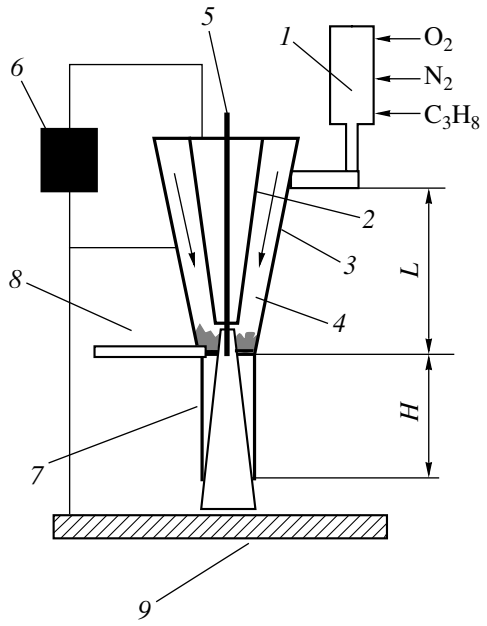

Fig. 1. A schematic diagram of the plasmatron for the high-speed pulsed plasma jet processing of articles (see the text for explanations).

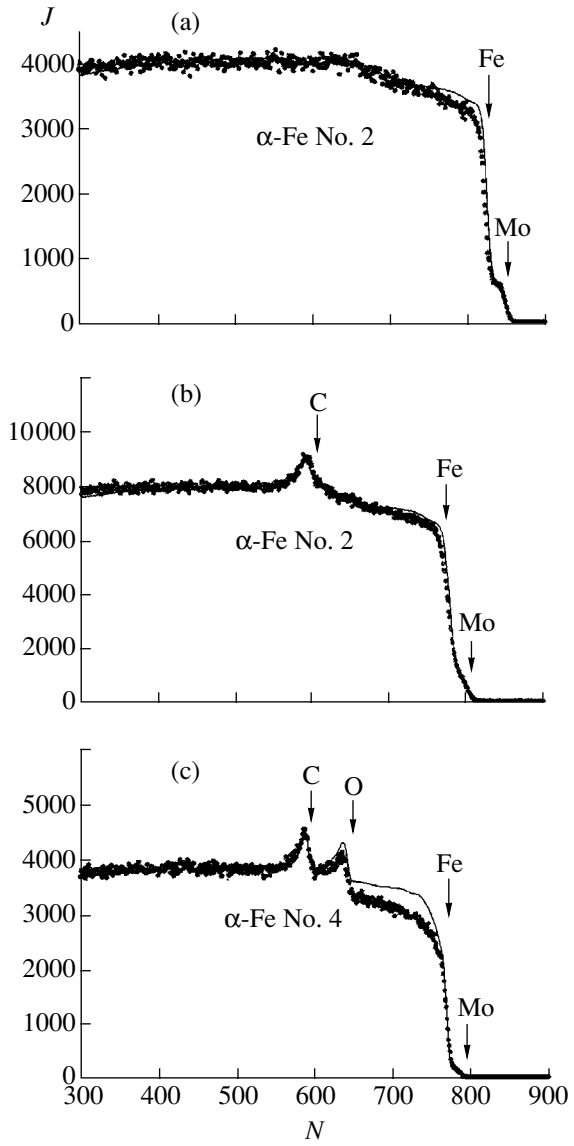

Fig. 2. The energy spectra of scattered ions for α-Fe samples doped with Mo in a pulsed plasmatron: (a) 1.847 MeV $^4He^+$ RBS of a sample exposed to 10 pulses; (b, c) the elastic resonance of 1.745-MeV protons for the samples exposed to 10 plasmatron pulses (determination of carbon and nitrogen) and 20 pulses (determination of carbon and oxygen), respectively. The measurements were performed for Θ = 170°; ν = 60°; No. is the channel number.

2000 Oe. During the subsequent 3–5 ms, the surface accepts the combustion products and eroded electrode material. Thus, exposing the α-Fe samples to the pulsed plasma jet containing doping elements is accompanied by a complex (thermal, electromagnetic, and deformation) action. This combined action ensures the doping of the surface layer with elements contained in the plasma and leads to strengthening of this layer. The plasma jet is characterized by a temperature reaching 2×10^3 K and a power density of about 10^7 W/cm^2 (for a jet velocity of 6 km/s). The sets of parameters used in various regimes of α-Fe treatment (for a system with Mo electrode) are listed in the table.

The X-ray diffraction study of the phase composition of plasma-treated α-Fe samples showed that the main phase is bcc Fe (with d = 2.866 Å). The other phases are Fe_7Mo_6 with the lattice parameters 2.157 (2.15) Å, 2.086 (2.08) Å, 1.811 (1.80) Å and, probably, FeMo with the parameters 2.157 (2.14) Å and 2.086 (2.09) Å.

Figure 2 shows the energy spectra of Rutherford backscattering (RBS) obtained using (a) the scattering of $^4He^+$ ions for α-Fe upon the plasma jet treatment and (b, c) the elastic resonance of 1745-keV protons for the same sample treated under various conditions. The spectra exhibit a boundary (of the kinetic factor) for Fe and a small step for Mo to the right of iron. The peak due to Mo indicates that the sample surface layer with a thickness of about 300 nm contains a compound with the composition $FeMo_2$. The spectrum of proton resonance clearly indicates the presence of carbon.

Figure 2c presents the proton elastic resonance spectrum measured upon treating the α-Fe sample with a greater number of plasma jet pulses. As is seen, the growth in the concentrations of carbon and nitrogen is accompanied by the appearance of a considerable amount of oxygen (~40 at.%) in the uppermost surface layer. Further growth in the number of pulses still increases the amount of oxygen at the surface. A different pattern is observed in Fig. 3 for the doping element (introduced by the electrode erosion and evaporation). The maximum Mo concentration is observed in a subsurface layer with a thickness D of about 10 μm. After a 10-pulse treatment, the limiting Mo concentration is 8 at. %, this maximum being observed at a depth of about 7 μm from the surface.

It was found that the carbon concentration increases rather insignificantly with the number of pulses, while the oxygen content reaches 40 at.% after the first 15 pulses. The content of Mo in the doped surface layer exhibits a maximum when the number of pulses increases from 4 to 20, with a peak of 8 at.% observed

Parameters of the plasma jet processing of samples (Mo electrode)

Sample No.	Material processed	Number of pulses	Distance, mm	ν, Hz	Electrode consumption, mm	Capacitance, μF
1	α-Fe	4	40	1.5	30	800
2	α-Fe	10	40	1.5	30	800
3	α-Fe	15	40	1.5	30	800
4	α-Fe	20	40	1.5	30	800

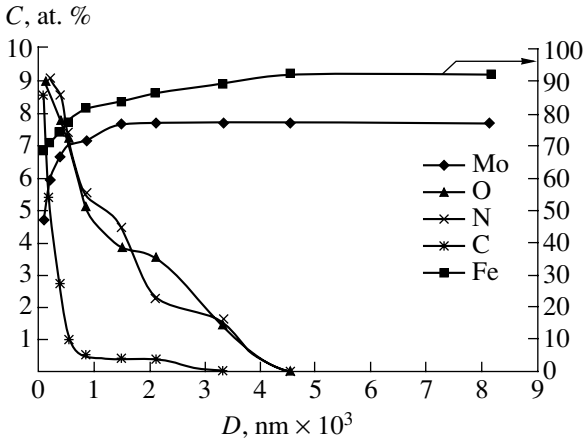

Fig. 3. Depth–concentration profiles of Mo, Fe, O, C, and N determined from the RBS spectra of an α-Fe sample exposed to 10 plasmatron pulses.

for the α-Fe sample exposed to 10 pulses of the high-speed plasma jet. An analysis of the cross section of such a sample showed that the region of fused material extends down to a depth of 50 μm.

The results of the microhardness measurements on the surface of an α-Fe sample modified by 20 plasma jet pulses showed an increase in the hardness, reaching in some areas up to 750 ± 40 kgf/mm^2. The same measurements performed in the cross section gave the value of 250 ± 27 kgf/mm at a depth exceeding 70 μm, which is still significantly higher as compared to the hardness of the initial sample (90 ± 12 kgf/mm^2). The average hardness across the entire modified layer was about 2.5 times the initial value.

Thus, the results of our experiments showed that, using a plasmatron with consumable Mo electrode, it is possible to dope the subsurface layer of an α-Fe sample with a thickness of at least 10 μm. The uppermost surface layer can be additionally saturated (doped) with oxygen and carbon. Moreover, the article can be fused down to a depth markedly exceeding the doped layer thickness.

Acknowledgments. The authors are grateful to O. Kolisnichenko for the plasma-jet treatment of the samples and the V.S. Kshnyakin and O.P. Kul'ment'eva for their help in conducting X-rat phase analysis and microhardness measurements.

This study was partly supported by the Ukrainian Scientific-Technological Center (project no.1472) and by the State Committee of Science and Technology of Ukraine (project no. 2M/076-2000.

REFERENCES

1. J. M. Poate, G. Foti, and D. C. Jacobsen, *Surface Modification and Compounding by Laser, Ion and Electron Beams* (Plenum, New York, 1983).
2. J. K. Hirvonen, *Ion Implantation* (Academic, New York, 1980).
3. V. I. Boĭko, A. N. Valyaev, and A. D. Pogrebnyak, Usp. Fiz. Nauk **163**, 1243 (1999).
4. A. N. Valyaev, A. D. Pogrebnyak, and Naoki Kishimoto, *Modification of Materials Properties and Synthesis of Thin Films under Irradiation by Intense Electron and Ion Beams* (Vostochno-Kazakhstanskiĭ Tekhnicheskiĭ Univ., Ust'-Kamenogorsk, 2000).
5. A. D. Pogrebnjak, S. Bratushka, V. I. Boyko, *et al.*, Nucl. Instrum. Methods Phys. Res. B **145**, 373 (1998).
6. Yu. N. Tyurin and A. D. Pogrebnjak, Surf. Coat. Technol. **111**, 269 (1999).
7. A. D. Pogrebnyak, Yu. N. Tyurin, Yu. F. Ivanov, *et al.*, Pis'ma Zh. Tekh. Fiz. **26** (21), 53 (2000) [Tech. Phys. Lett. **26**, 960 (2000)].
8. A. Khasuĭ, *Technique of Evaporation* (Mashinostroenie, Moscow, 1985).
9. V. V. Kudinov, *Plasma Coatings* (Nauka, Moscow, 1977).

Translated by P. Pozdeev

Technical Physics Letters, Vol. 27, No. 8, 2001, pp. 622–625. Translated from Pis'ma v Zhurnal Tekhnicheskoĭ Fiziki, Vol. 27, No. 15, 2001, pp. 9–14.

Noise-Induced Transitions in a System of Coagulating Particles

V. M. Loginov and O. É. Leshakov

Institute for the Complex Exploration of Natural Resources, Russian Academy of Sciences, Kyzyl, Tuva, Russia

e-mail: v_loginov@mail.ru

Received February 16, 2001

Abstract—Rigorously solvable models of the system of coagulating particles in a stochastic medium are proposed. It is demonstrated that such systems are featuring additional noise-induced stationary states. The results are considered from the standpoint of using this phenomenon for evaluating the effective parameters of the medium. © *2001 MAIK "Nauka/Interperiodica".*

Nonlinear dynamical systems experiencing the external noise influence have been extensively studied in recent years. Of special interest is the case of a "color" noise (the noise possessing a finite correlation radius) frequently encountered in both natural phenomena and technological applications. Dynamics of a system occurring in the field of such a noise exhibits certain interesting features very interesting from the standpoint of physics [1]. In particular, an important circumstance is the appearance of additional stationary states impossible in the case of completely deterministic external actions.

In this study, various dynamic regimes induced by the color noise are revealed by an analysis of a system of coagulating particles descried within the framework of rigorously solvable models. A source of the stochastic action is represented as a combined effect of a variety of factors, including both external (related to the medium) and internal. A significant simplification of the problem is provided by an approach treating these factors in terms of effective sources and fields acting upon the system of coagulating particles under consideration. Mathematically, the stochastic factors are taken into account via fluctuations of the parameters entering into the dynamic equations of the coagulation process.

As will be demonstrated below, the correlation radius of the color noise plays the role of the order parameter and influences a stationary coagulation regime established in the system in a nontrivial manner. Another important circumstance is that parameters of the effective stochastic medium can be reconstructed using the measurable characteristics of distribution of the coagulating particle concentration.

The coagulation processes are frequently studied based on the phenomenological Smoluchowski equation [2] describing the temporal dynamics of the j-mer concentration C_j in the system. In the presence of an external particle source and the time-dependent coagulation, this equation can be written as follows:

$$\frac{dC_j}{dt} = I_j f(t) + \frac{1}{2}\sum_{n=1}^{j-1} K(j-n, n; t) \times C_{j-n}C_n - C_j \sum_{n=1}^{\infty} K(j, n; t)C_n, \quad (1)$$

where $K(x, y; t)$ is the coagulation nucleus (or constant). By its physical meaning, the function $K(x, y; t)$ characterizes the coagulation rate and is considered as preset. The first term in Eq. (1) describes the supply of j-mers to the system; the function $f(t)$ is considered as random. Let us assume that the function $K(j, n; t)$ is independent of the indices j and n, so that $K(j, n; t) = a(t)$, and that only monomers are supplied to the system studied ($I_j = I\delta_{j,1}$, where $\delta_{j,1}$ is the Kronecker delta). These assumptions are not too rigid and are frequently used in the descriptions of coagulation in systems with sources (see, e.g., [2, 3]).

The stochastic dynamics of the external factors is modeled by a jumplike Markoff dichotomic process (D-noise) in the form of $\alpha(t) = \pm 1$ with an exponentially decaying correlation function $K(t) = \langle\alpha(t)\alpha(t+\tau)\rangle = \exp(-2\nu|\tau|)$ (the symbol $\langle\ldots\rangle$ denotes averaging over the ensemble of realizations of the $\alpha(t)$ process). For the D-noise, the values of $\alpha(t) = \pm 1$ are equiprobable and $\langle\alpha(t)\rangle = 0$, while the time instants of changing the $\alpha(t)$ sates form a Poisson flux of events [4]. The time $\tau \sim 1/\nu$, on the one hand, sets a characteristic time of decay of the $\alpha(t)$ process correlations and, on the other hand, determines the average "lifetime" of a certain state.

Let us analyze behavior of the countable concentration $N = \sum_{j=0}^{\infty} C_j$. This is an important generalized characteristic of the coagulation process that can be

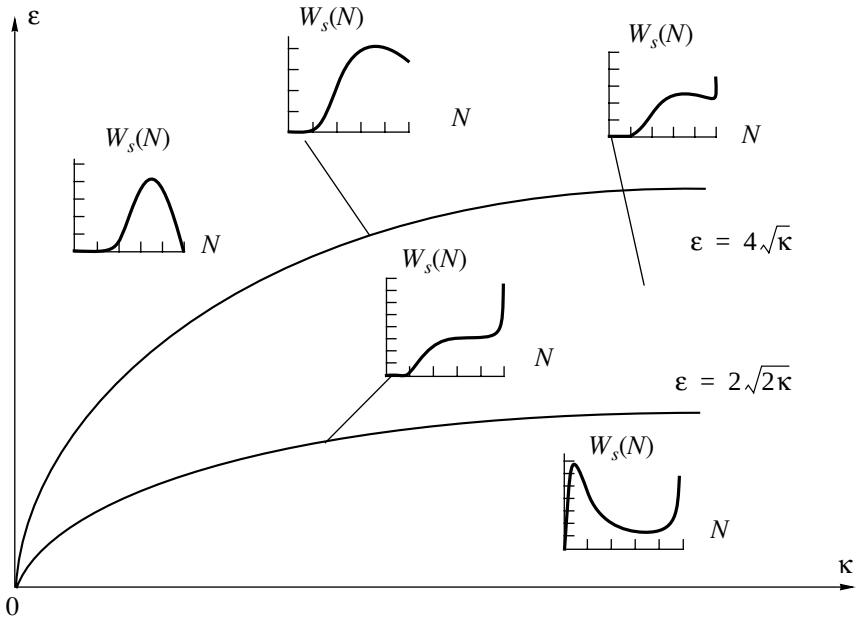

Fig. 1.

measured in experiment. A stochastic equation for the countable concentration acquires, assuming a linear dependence of $f(t)$ and $a(t)$ on $\alpha(t)$, the following form:

$$\dot{N} = p(N) + q(N)\alpha(t). \tag{2}$$

In view of the nonlinearity of Eqs. (1) and (2), a statistical description of the coagulation process will be conducted within the framework of the kinetic equations for the N probability distribution. The consideration will be restricted to a single-point distribution $W(N, t)$ of the countable concentration in system (1) under the action of a Markoff D-noise with arbitrary ν. The quantity $W(N, t)dN$ is the probability that the countable concentration at the instant t falls within the interval $(N, N + dN)$.

Equations of the type (2) are well studied in the theory of noise-induced phase transitions. A rigorous stationary solution $W_s(N)$ in the case when $\alpha(t)$ represents a Markoff D-noise is known (see, e.g., [1, 5]). The distribution is $W_s(N) \equiv 0$ outside the carrier representing a closed interval $0 \le N \le N_b$ with the boundaries determined by stable stationary states (described by Eq. (2) for $\alpha = \pm 1$ and $\dot{N} = 0$).

Stochastic source, constant nucleus $a(t) = \text{const} = a$. Consider a typical situation when monomers are supplied to the system at a constant rate within random time intervals, $f(t) = \frac{1}{2}(1 + \alpha(t))$, which corresponds to Eq. (2) with $p(N) = \frac{1}{2}(I - a(t)N^2)$, $q(N) = \frac{I}{2}$.

A solution $W_s(N)$ to Eq. (2) (with the dimensionless parameters $\varepsilon = 4\nu/a$, $\kappa = 2I/a$) is

$$W_s(N) = CN^{-2}\exp\left(-\frac{\varepsilon}{2N}\right) \times (\sqrt{\kappa} - N)^{\frac{\varepsilon}{4\sqrt{\kappa}} - 1} (\sqrt{\kappa} + N)^{-\left(\frac{\varepsilon}{4\sqrt{\kappa}} + 1\right)}, \tag{3}$$

where C is a normalization constant. The parameters ε and κ compare a characteristic source switching frequency and the frequency of particle supply from the source to the frequency of coagulation events. The distribution $W_s(N)$ is determined on the interval $N \in [0, N_b]$, $N_b = \sqrt{\kappa}$.

An important consequence of solution (3) is the division of the phase space of the system parameters into regions with significantly different "geometric" images of the stationary probability density. The structure of the phase plane is determined by the relationship between the parameters ε and κ, which may lead to stationary distributions of several possible types, including monotonic, single-mode (a distribution with one maximum), or a distribution with two extrema (maximum and minimum) (Fig. 1). The extrema of $W_s(N)$ are determined by the relationships

$$N_1 = \frac{\nu}{a} = \frac{\varepsilon}{4} \quad \text{and} \quad N_2 = \sqrt{\frac{I}{a}} + \sqrt{\frac{\kappa}{2}}. \tag{4}$$

Note that the extremal values of $W_s(N)$ (correspond-

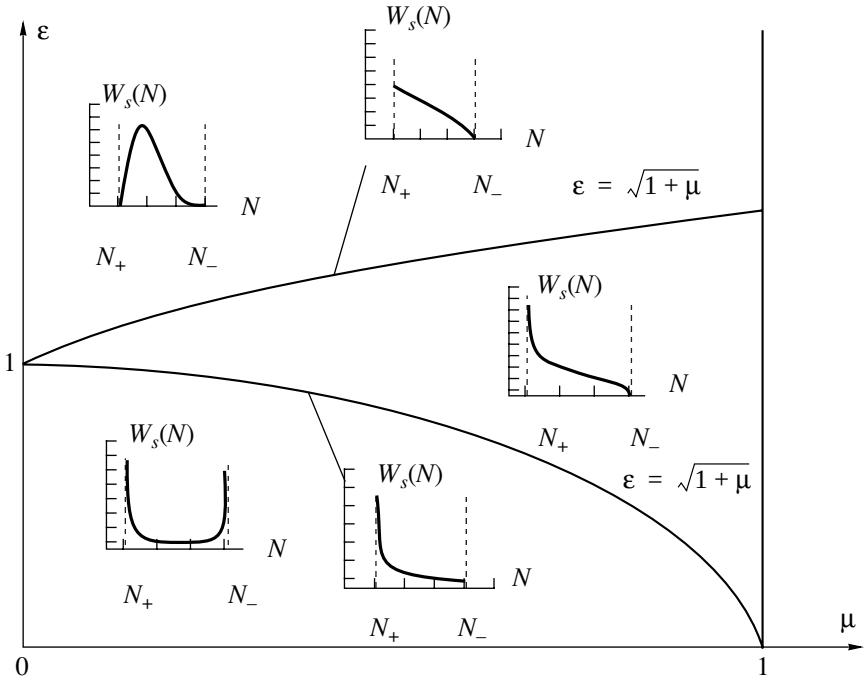

Fig. 2.

ing to the measurable N values) are determined by various parameters. As the frequency of source switching (on and off) increases, the system moves from the bottom region of the phase diagram (where a maximum $W_s(N)$ value is determined by the frequency) to the top region (where the same value is determined by the source intensity). During this transition, the system exhibits a series of "geometric" transformations for the $W_s(N)$ function, which correspond to different variants of the macroscopic behavior (i.e., the noise-induced phase transitions take place).

The established sequence of transitions from the distribution with a minimum inside the carrier to the opposite situation of the distribution with a maximum physically implies the following: by varying the frequency of switching of a stochastic source of particles, we may effectively control the average size of clusters (related to the position of the distribution maximum) in a system of coagulating particles.

Constant source $f(t) = \text{const} = I_0$, stochastic nucleus. Consider a system of coagulating particles in which nonstationary external conditions lead to jumplike fluctuations in the coagulation nucleus (e.g., switch on additional aggregation mechanisms such as the inertial sedimentation, turbulent coagulation, etc., see [6]). Let $a = a(t) = a_0 + a_1\alpha(t)$, where $\alpha(t)$ is the aforementioned D-noise. Physical considerations lead to the relationship $a_1 \le a_0$.

A stationary solution for $W_s(N)$ with the dimensionless parameters $\kappa = 2I_0/a_0$, $\varepsilon = \nu/a_0$, and $\mu = a_1/a_0$ is

$$W_s = C\frac{N^2(N-N_+)^{\frac{\varepsilon}{\sqrt{\kappa(1+\mu)}}-1}(N_--N)^{\frac{\varepsilon}{\sqrt{\kappa(1-\mu)}}-1}}{(N+N_+)^{\frac{\varepsilon}{\sqrt{\kappa(1+\mu)}}+1}(N_-+N)^{\frac{\varepsilon}{\sqrt{\kappa(1-\mu)}}+1}}, \quad (5)$$

where $N_\pm = \sqrt{\frac{\kappa}{1\pm\mu}}$ and the parameter μ characterizes a "kinetic contrast" of the coagulation processes corresponding to various $\alpha(t)$ Obviously, $\mu \le 1$; the case of $\mu = 1$ corresponds to the maximum "contrast" representing a situation when the coagulation process dynamics possesses a "switching" character. The distribution is determined on the interval $N \in [N_+, N_-]$ with a nonzero left boundary. As is seen from the solution (6), the external noise again generates a subdivision of the phase space of the system parameters into regions corresponding to different macroscopic states of the system (Fig. 2).

In conclusion, it should be noted that a description of the stochastic medium acting upon a coagulating system in terms of the effective particle sources (as well as sinks and effective fluctuations of the nucleus) is sufficiently physical, especially in the case of atmospheric coagulation. This circumstance is important from the standpoint of obtaining essential information about the state of the external medium, which is difficult to evaluate by experimental methods (see Eq. (4)). Additional

interest is related to the possibility of solving inverse problems, for example, of determining the coagulation constant from the known ν and I and observed N values. In addition, the dependence of the stationary value of the countable concentration on the average process frequency $\alpha(t)$ indicates that there are certain possibilities to control the average size of clusters formed by the coagulating particles.

REFERENCES

1. W. Horsthemke and R. Lefever, *Noise Induced Transitions: Theory and Applications in Physics, Chemistry and Biology* (Springer-Verlag, Heidelberg, 1984; Mir, Moscow, 1987).
2. V. M. Voloshchuk, *Kinetic Theory of Coagulation* (Gidrometeoizdat, Leningrad, 1984), p. 284.
3. A. A. Lushnikov, V. N. Piskunov, and I. G. Osidze, Dokl. Akad. Nauk SSSR **287** (3), 679 (1986).
4. R. Bourret, U. Frisch, and A. Pouquet, Physica **65** (3), 409 (1973).
5. V. M. Loginov, Acta Phys. Pol. B **27** (3), 693 (1996).
6. Yu. A. Dovgalyuk and L. S. Ivlev, *Physics of Aqueous and Other Atmospheric Aerosols* (Sankt-Peterb. Gos. Univ., St. Petersburg, 1998).

Translated by P. Pozdeev

Technical Physics Letters, Vol. 27, No. 8, 2001, pp. 626–628. Translated from Pis'ma v Zhurnal Tekhnicheskoĭ Fiziki, Vol. 27, No. 15, 2001, pp. 15–21.

Anisotropy of the Electromechanical Properties and a High Piezoelectric Sensitivity of the 1–1 Type Ferroelectric Piezocomposites

S. V. Glushanin and V. Yu. Topolov

Institute of Physics, Rostov State University, Rostov-on-Don, Russia

e-mail: topolov@phys.rnd.runnet.ru

Received February 12, 2001

Abstract—The electromechanical properties of ferroelectric piezocomposites of the 1–1 and 1–0–1 types were studied for the first time. The effect of the geometric factor on the piezocoefficients, electromechanical coupling coefficients, detection parameters, and piezosensitivity was studied. Exhibiting a nonmonotonic concentration dependence of these parameters, the materials studied have no analogs among piezocomposites with the connectivities of other types. © *2001 MAIK "Nauka/Interperiodica".*

Problems encountered in the creation of new piezoactive composites and in the prediction and optimization of their physical properties are still waiting for solution [1–3]. The modern methods of the computer structure design and property simulation facilitate the search for components ensuring the further effective use of the composite materials as elements in various piezoelectric devices such hydrophones, microphones, sensors, actuators, etc. Despite relatively simple microscopic geometry, piezocomposites of the 1–1 connectivity type (with the two interacting components analogous to parallel rods [4] continuously distributed in the same direction) have not been studied as yet. The purpose of this study was to analyze the electromechanical properties of two- and three-component piezocomposites with connectivity elements of the 1–1 type.

In the proposed model, a 1–1 piezocomposite is modeled by a system of rectangular parallelepipeds, representing a ferroelectric piezoceramics (FEPC) and a polymer, alternating in the OX_1 and OX_2 directions (Fig. 1). The bases of all parallelepipeds occur on the X_1OX_2 plane and their heights (measured along the polarization axis OX_3) are equal to h ($h \gg |LN|$, $h \gg |LU|$). In addition, the model takes into account the porosity of the polymer, which is represented as a matrix divided into the Banno cubic cells of unit volume [5, 6] containing air inclusions in the form of a rectangular parallelepiped with the edges parallel to the OX_i axes. This height of such a parallelepiped amounts to the νth fraction of the Banno cell edge and the base area amounts to the rth fraction of the cell base area. The physical constants of the porous polymer component are determined as descried in [6, 7] as functions of ν and r. The FEPC–porous polymer composite is characterized by the 1–0–1 connectivity.

Averaging of the constants of the FEPC and polymer (homogeneous or porous) components is performed in two stages using the formulas from [7, 8]: first, with respect to the concentration parameter t along the OX_1 axis (assuming the electro- and elastostatic boundary conditions to be valid for layers of the *LMSR*, *RSVU* and *MNTS*, *STWV* types, extended along OX_3; everywhere x_1 = const); second, with respect to the parameter n along the OX_2 axis (assuming analogous conditions for the layers bounded by *LU*, *MV* and *MV*, *NW* lines). The 1–1 (Fig. 1) and 1–0–1 type structures belong to the point symmetry group *mm*2 and exhibit the following feature: the electromechanical properties determined for a particular connectivity (1–1 or 1–0–1) remain unchanged on the passage from parameters (t; n) to (1–t; 1–n).

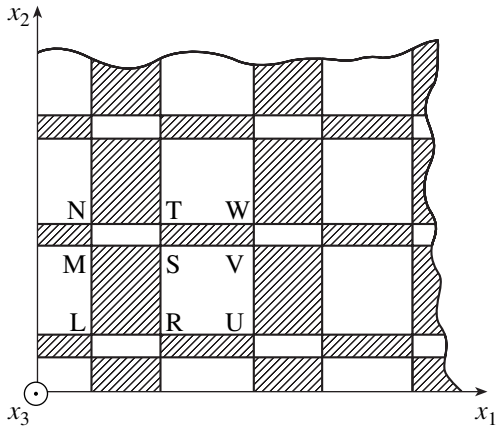

Fig. 1. A cross section of the 1–1 piezocomposite polarized along the OX_3 axis. Dashed areas indicate the FEPC component; $t = |MS|/|MN|$ and $n = |RS|/|RT|$ are the parameters determining the volume concentration of components.

1063-7850/01/2708-0626$21.00 © 2001 MAIK "Nauka/Interperiodica"

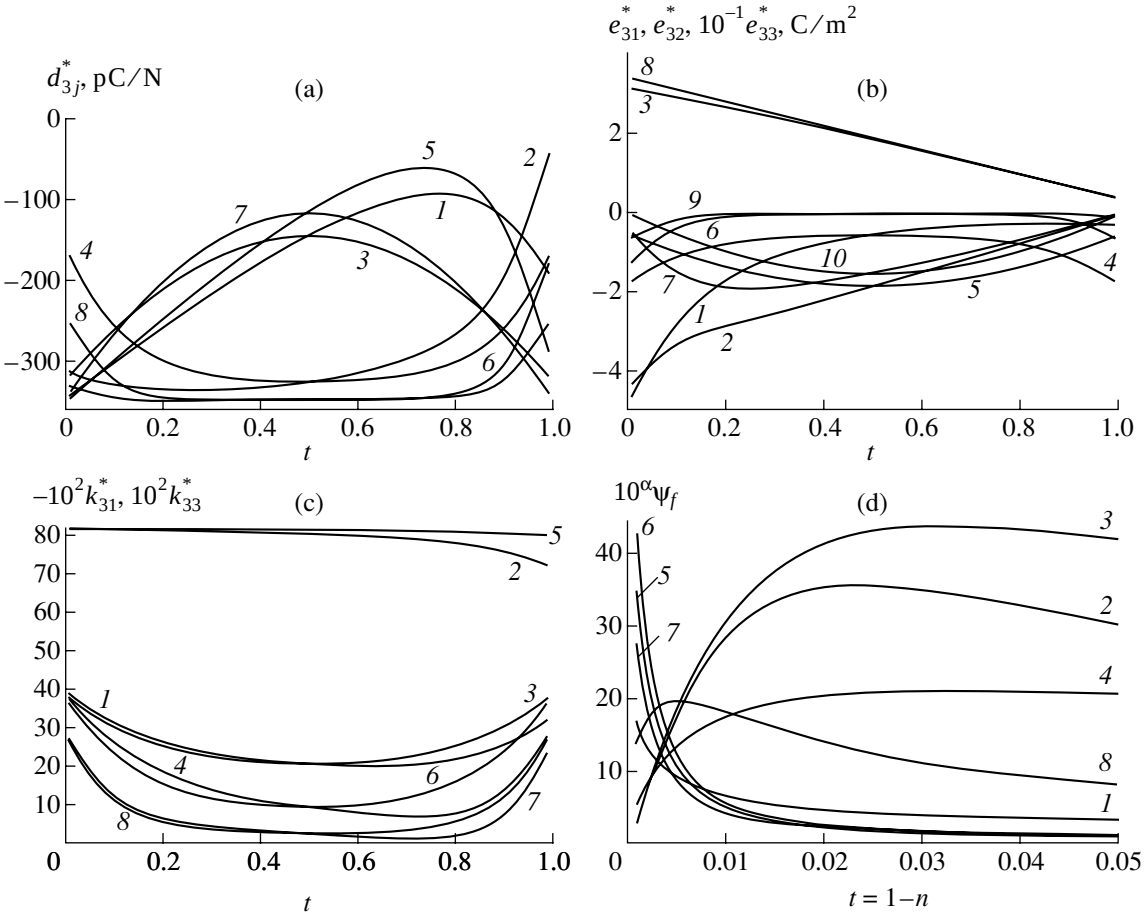

Fig. 2. Concentration dependences of (a) d^*_{3j}, (b) e^*_{31}, e^*_{32}, $10^{-1}e^*_{33}$, (c) $-10^2k^*_{31}$, $10^2k^*_{33}$, and (d) $10^\alpha\psi_f$ calculated for piezocomposites of the FEPC(PKR-7M)–araldite (1–1 connectivity) and FEPC(PKR-7M)–porous araldite (1–0–1 connectivity) types. (a): d^*_{31} (*t*, 0.1) (*1*, *5*), d^*_{31} (*t*, 0.5) (*3*, *7*), d^*_{32} (*t*, 0.1) (*2*, *6*), d^*_{32} (*t*, 0.5) (*4*, *8*), curves *1–4* and *5–8* refer to 1–0–1 composites with matrices A and B, respectively; d^*_{33} (*t*, 0.5) = 747 pC/N (matrix *A*) and 758 pC/N (matrix *B*; (b): e^*_{31} (*t*, 0.1) (*1*, *6*), e^*_{31} (*t*, 0.5) (*4*, *9*), e^*_{32} (*t*, 0.1) (*2*, *7*), e^*_{32} (*t*, 0.5) (*5*, *10*), $10^{-1}e^*_{33}$ (*t*, 0.1) (*3*,*8*), curves *1–5* and *6–10* refer to 1–1 and 1–0–1 composites, respectively; e^*_{33} (*t*, 0.5) = 18.5 C/m^2 (1–1 composite) and 19/1 C/m^2 (1–0–1 composite); a porous polymer component in 1–0–1 composites represents matrix *B*; (c): $(-10^2)k^*_{31}$ (*t*, 0.1) (*1*, *4*, *7*), $(-10^2)k^*_{31}$ (*t*, 0.5) (*3*, *6*, *8*), $10^2k^*_{33}$ (*t*, 0.1) (*2*, *5*), $10^2k^*_{33}$ (*t*, 0.5) (*5*), curves *1–3* and *4–8* refer to 1–1 and 1–0–1 composites, respectively; k^*_{33} (*t*, 0.5) = 0.803 C/m^2 (1–1 composite), 0.813 C/m^2 (1–0–1 composite, matrix *A*), 0.815 C/m^2 (1–0–1 composite, matrix *B*); a porous polymer component in 1–0–1 composites represents matrix *A* (*4–6*) and matrix *B* (*7*, *8*); (d) ψ_1 (*5*), ψ_1 (*8*), $10^{-3}\psi_2$ (*6*), ψ_2 (*2*), $10^{-1}\psi_3$ (*7*), $10\psi_3$ (*3*), ψ_4 (*1*), $10\psi_4$ (*4*), curves *1*, *5–7* refer to 1–0–1 composite (matrix *A*), curves *2–4*, *8* refer to 1–1 composite.

An active piezoelectric component for the 1–1 and 1–0–1 composites will be represented by a perovskite FEPC of the PCR-7M type characterized by high values of the piezomoduli d^{FC}_{ij} and the piezocoefficient e^{FC}_{33} (maximum among $Pb(Zr,Ti)O_3$ based piezoceramics) [9].[1] This component accounts for a record piezosensitivity of the composites with the 1–3 connectivity elements [1]. The second component of the 1–1 structure is represented by the nonpiezoactive polymer araldite. In the 1–0–1 structure, araldite is porous and represents a matrix of the type described above, containing a system of plane-parallel (v = 0.10; *r* = 0.99, matrix *A*) or elongated (along OX_3) air-filled pores (v = 0.99; *r* = 0.10, matrix *B*) with the same bulk concentration ν*r*.

Figure 2 shows the plots of some calculated relationships between the system parameters and the concentrations (*t*; *n*), effective piezomoduli d^*_{3j}, piezocoef-

[1] Here and below, the electromechanical constants of FEPC and piezocomposites are indicated by superscripts *FC* (X^{FC}) and asterisk (X^*), respectively. The transition from X^* to X^{FC} corresponds to $t = n = 0$ or $t = n = 1$.

ficients e^*_{3j}, electromechanical coupling coefficients $k^*_{3m} = d^*_{3m}/(\varepsilon^{*\sigma}_{33} s^{*E}_{mm})^{1/2}$, and factors ψ_f (s^{*E}_{iq} and $\varepsilon^{*\sigma}_{33}$ are the elastic compliance and dielectric permittivity parameters, respectively):

$$\psi_1 = g^*_{33}/g^{FC}_{33}; \quad \psi_2 = (Q^*_h/Q^{FC}_h)^2; \quad \psi_3 = (Q^*_{33}/Q^{FC}_{33})^2; \quad \psi_4 = Q^*_d/Q^{FC}_d. \tag{1}$$

In relationships (1), the piezocoefficients g^*_{33}, the squared hydrostatic (hydrophone) figure of merit (HFOM) $(Q^*_h)^2 = (d^*_{31} + d^*_{32} + d^*_{33})^2/\varepsilon^{*\sigma}_{33}$, and the squared parameter $(Q^*_{33})^2 = d^*_{33}g^*_{33}$ describe the piezosensitivity of a composite, while the quantity $Q^*_d = d^*_{33}/(\varepsilon^{*\sigma}_{33}/\varepsilon_0)^{1/2}$ characterizes a specific sensitivity taking into account the internal resistance of the piezodetector. In the calculations, we used the room-temperature electromechanical constants from [7. 9].

The fact that $d^*_{3j}(t, n)$, $e^*_{3j}(t, n)$, and $k^*_{31}(t, n)$ for $n = 0.1$ vary in a wider interval than for $n = 0.5$ (Figs. 2a– 2c is related to a large redistribution of the internal mechanical and electric fields in the layers of significantly different thicknesses alternating along OX_1 and OX_2. Nevertheless, the data reveal a more pronounced anisotropy ($e^*_{33}(t, n)/|e^*_{3j}(t, n)| > 10$; $j = 1, 2$) for $n = 0.5$ than for $n = 0.1$, although the e^*_{31} and e^*_{32} values near $b = 0.5$ differ by a factor of 3–40. The concentration dependences analogous to that for $e^*_{3j}(t, n)$ were never studied before (see, e.g., [1, 3, 6, 10, 11]) and may be of interest for some applications. Differences between the shapes of $d^*_{3j}(t, 0.1)$ and $e^*_{3j}(t, 0.1)$ curves (cf. Figs. 2a and 2b) are related to the behavior of elastic pliabilities $s^{*E}_{iq}(t, 0.1)$. The influence of these values (especially pronounced in the case of $q = 3$) increases on the passage from homogeneous to porous araldite (i.e., from matrix *A* to *B*). The constancy of $d^*_{33}(t, 0.5)$, $e^*_{33}(t, 0.5)$, and $k^*_{33}(t, 0.5)$ is related to the fact that a change in the thicknesses of layers $|RU|$ and $|LR|$ for $|LR| = |MN|$ (Fig. 1) affects neither the volume concentration of FEPC component nor the composite response in the OX_3 direction to the external action along the same axis (due to the boundary conditions at $x_j = \text{const}$, $j = 1, 2$).

The presence of pores leads to significant changes in the composite parameters (1). For $t = 1 - n \ll 1$, an analysis showed a sharp increase in piezosensitivity of the 1–0–1 structure ($\psi_f \approx 10\ldots4.2 \times 10^4$) as compared to the 1–1 type. The passage from matrix *A* to *B* does not significantly affect the values of $d^*_{33}(t, n)$, $e^*_{33}(t, n)$, $k^*_{33}(t, n)$ and $\psi_f(t, n)$, which is an important advantage of the given 1–0–1 composite. In contrast to a 1–3 composite of the FEPC rod–polymer type (∞mm symmetry) [4, 6, 7], the 1–0–1 composite ($mm2$ symmetry) with $t = 1 - n \ll 1$ features a system of rods representing the porous polymer surrounded by thin FEPC layers parallel to the X_1OX_3 or X_2OX_3 planes. Of certain interest are the $k^*_{31}(t, n)$ relationships, the behavior of which (cf. curves *1*, *3*, *4*, *6–8* in Fig. 2c) is significantly influenced by the elastic compliance parameter s^{*E}_{11} (depending to a considerable extent on the elastic properties of the porous polymer). This influence is manifested by a significant difference between the anisotropy factors d^*_{3j} and k^*_{31} (e.g., for $t = 0.5$, $d^*_{33}/d^*_{31} \approx -6.6\ldots-5.2$ and $k^*_{33}/k^*_{31} \approx -34\ldots-9.1$) not characteristic of the composites belonging to the ∞mm symmetry group [3, 4, 6, 7, 11].

Thus, the results presented above increase our knowledge of the factors favoring an increase in the piezoelectric anisotropy [3, 6, 11] and the HFOM values [1, 2, 12]. These data are indicative of the good prospects for using structures of the 1–1 type with large $e^*_{33}/|e^*_{3j}|$, k^*_{33}, k^*_{33}/k^*_{31}, and ψ^*_f values.

REFERENCES

1. V. Yu. Topolov and A. V. Turik, Pis'ma Zh. Tekh. Fiz. **27** (2), 84 (2001) [Tech. Phys. Lett. **27**, 81 (2001)].
2. O. Sigmund, S. Torquato, and I. A. Aksay, J. Mater. Res. **13** (4), 1038 (1998).
3. V. Yu. Topolov and A. V. Turik, Pis'ma Zh. Tekh. Fiz. **24** (11), 65 (1998) [Tech. Phys. Lett. **24**, 441 (1998)].
4. R. E. Newnham, MRS Bull. **22** (5), 20 (1997).
5. H. Banno, Ceram. Bull. **66** (9), 1332 (1987).
6. F. Levassort, V. Yu. Topolov, and M. Lethiecq, J. Phys. D **33** (16), 2064 (2000).
7. F. Levassort, M. Lethiecq, D. Certon, and F. Patat, IEEE Trans. Ultrason. Ferroelectr. Freq. Control **44** (2), 445 (1997).
8. E. Akcakaya and G. W. Farnell, J. Appl. Phys. **64** (9), 4469 (1988).
9. *High-performance Piezoceramic Materials (Handbook)* (Kniga, Rostov-on-Don, 1994).
10. A. A. Grekov, S. O. Kramarov, and A. A. Kuprienko, Ferroelectrics **76** (1-4), 43 (1987).
11. V. Yu. Topolov and A. V. Turik, J. Appl. Phys. **85** (1), 372 (1999).
12. V. M. Petrov, Zh. Tekh. Fiz. **57** (11), 2273 (1987) [Sov. Phys. Tech. Phys. **32**, 1377 (1987)].

Translated by P. Pozdeev

Technical Physics Letters, Vol. 27, No. 8, 2001, pp. 629–631. Translated from Pis'ma v Zhurnal Tekhnicheskoĭ Fiziki, Vol. 27, No. 15, 2001, pp. 22–26.

Dielectric Characteristics of Biocompatible $Ca_{10}(PO_4)_6(OH)_2$ Ceramics

N. A. Zakharov and V. P. Orlovskiĭ

Institute of General and Inorganic Chemistry, Russian Academy of Sciences, Moscow, 117907 Russia

Received February 21, 2001

Abstract—The temperature dependence of the dielectric permittivity and losses of biocompatible $Ca_{10}(PO_4)_6(OH)_2$ ceramics were studied in a temperature range from 20 to 500°C. An approach to the interpretation of anomalies (bending points) observed in the dielectric characteristics of the ceramic samples is proposed, which takes into account features of the crystal structure of calcium hydroxyapatite and the defects formed in the course of thermal treatments. © *2001 MAIK "Nauka/Interperiodica".*

The synthesis and characterization of calcium hydroxyapatite (CHA) $Ca_{10}(PO_4)_6(OH)_2$ has drawn an increasing attention of chemists and physicists [1]. This is explained to a considerable degree by the fact that this compound is close in composition to the inorganic component of bone tissues of both animals and humans, which allows CHA to be used as an implant material in medicine [2]. The problems related to the identification of the CHA implants and the possibility of electric stimulation of the implantation process make a thorough investigation of the physicochemical properties of CHA a very important task.

Below, we present the results of experimental measurements of the dielectric permittivity (ε) and the dielectric loss tangent ($\tan\delta$ of CHA synthesized from solution as described elsewhere [3]. The synthesized product had a Ca/P atomic ratio of 1 : 6, the unit cell parameters a = 9.376 ± 0.004 Å and c = 6.862 ± 0.005 Å (space group $P6_3/m$), and the CHA content of not less than 98%. The samples for the dielectric measurements had the shape of cylindrical tablets prepared by pressing (without binders) and then annealed in air at ~1000°C. The electrodes were obtained by fusing a silver paste at 600°C. The ε and $\tan\delta$ values were measured using an automated ac bridge operated in a dynamic regime with the sample temperature varied at a rate of ~0.5 K/s and an applied probing voltage below 15 V.

Figure 1 shows the temperature dependence of ε measured at the frequencies f = 1 and 5 kHz. The curves exhibit anomalies in the form of bending points at 60, 200, and 300°C. As the probing field frequency increases, the ε values tend to decrease (Fig. 2) and two of the above anomalies shift from 60 and 200°C toward higher temperatures.

The temperature dependence of $\tan\delta$ also exhibits a feature (local maximum) at about 60°C, but this feature exhibits virtually no shift with increasing frequency. At the same time, a more pronounced maximum of $\tan\delta$ at ~150°C tends to shift towards higher temperatures. A step observed in the $\tan\delta(T)$ curve at ~210°C (Fig. 1, f = 5 kHz) almost vanishes when the frequency is increased.

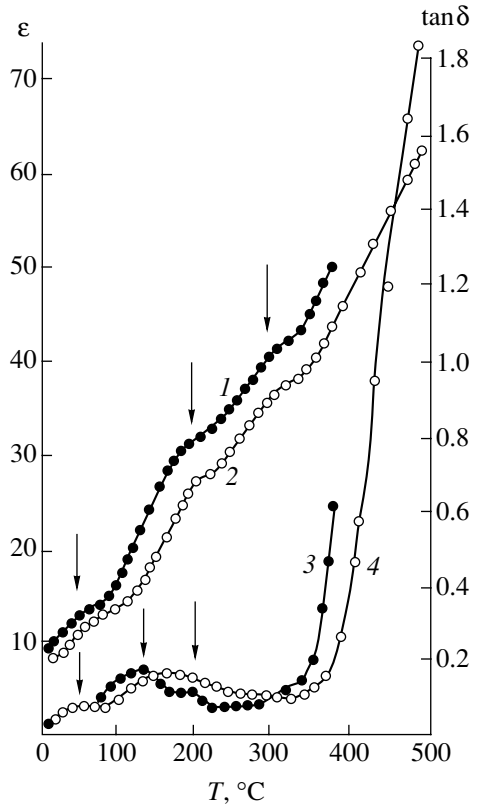

Fig. 1. The temperature variation of the permittivity ε (*1*, *2*) and the loss factor $\tan\delta$ (*3*, *4*) of CHA measured at f = 10^3 (*1*, *3*) and 5×10^3 Hz (*2*, *4*).

1063-7850/01/2708-0629$21.00 © 2001 MAIK "Nauka/Interperiodica"

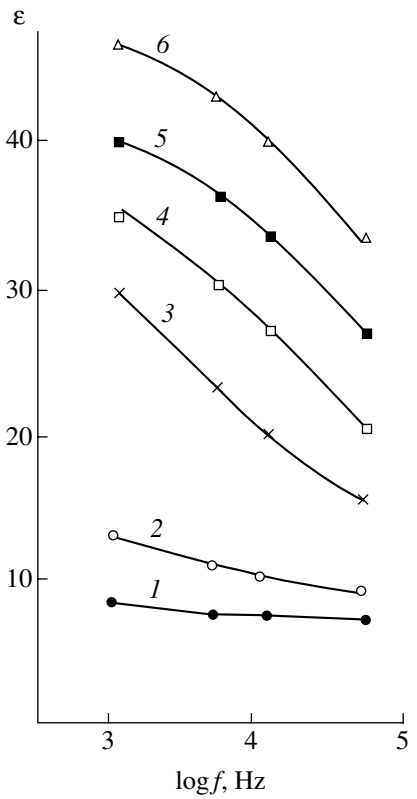

Fig. 2. The frequency dependence of the permittivity ε of CHA measured at T = 20 (*1*), 60 (*2*), 180 (*3*), 240 (*4*), 300 (*5*), and 360°C (*6*).

An analysis of the results of dielectric measurements must take into account peculiarities of the CHA crystal structure and the defects appearing in the samples during preparation. According to the structural data [1], the aforementioned features of $\varepsilon(T)$ and $\tan\delta(T)$ are most probably determined by the weakly bound hydroxy groups OH^- oriented perpendicularly to the Ca triangles forming channels in the apatite structure.

The temperature region of the structural transition in CHA at 200°C [4], which is related to predominant orientation of the OH^- groups in the same direction in the calcium channels [5, 6], corresponds to the most labile crystal structure and maximum electrical losses. A less pronounced contribution to the growth of these losses is related to the establishment of the antiparallel orientation of OH^- groups in adjacent channels [5, 6]. This process only leads to an insignificant anomaly of the $\varepsilon(T)$ curve at 300°C.

Above 300°C, the behavior of the dielectric characteristics of CHA is apparently determined by polarization processes of the migration type. These may be related both to the formation of thermal defects and to a change in the sample composition. The possible pathways [7, 8] include topochemical reactions leading to the formation of a defective CHA of the type $Ca_9(HPO_4)(PO_4)_5(OH)$ in the bulk of the sample; decomposition of the defective and stoichiometric CHA phases by the reactions

$$Ca_9(HPO_4)(PO_4)_5(OH) = 3Ca_3(PO_4)_2 + H_2O,$$

$$Ca_{10}(PO_4)_6(OH)_2 = 3Ca_3(PO_4)_2 + CaO + H_2O;$$

and the formation of oxoapatite $Ca_{10}(PO_4)_6O$ and vacancies [7],

$$Ca_{10}(PO_4)_6(OH)_2 = Ca_{10}(PO_4)_6O\square + H_2O$$

(the symbol □ denotes a vacancy).

The large variety of structural defects produced by these reactions allows a number of factors to be responsible for the dielectric anomalies observed at 60 and 150°C. The most significant factors are the presence of species (water and oxygen molecules, OH^- and O^- radicals) absorbed from air by the defective CHA structure and the participation of water (structurized and formed as a result of CHA decomposition) in the orientation processes proceeding in the applied ac electric field.

In this stage of research, reliable identification of the anomalies observed in the dielectric characteristics at 60 and 150°C is hardly possible. However, solving this task is facilitated by the fact that there are certain characteristic features in common for CHA and compounds containing hydroxide groups. Indeed, micas containing a large proportion of hydroxide groups also exhibit several $\tan\delta(T)$ maxima depending on the number and the degree of binding of these groups. For example, the $\tan\delta$ measured at 50 Hz for phlogopite (a mica possessing a layered structure with OH "crosslinks") increases from 0.05 to 0.2 on heating above room temperature, with a maxima at 80 and 180°C [9]. At higher temperatures, the $\tan\delta$ growth rate significantly drops. The low-temperature anomalies in the dielectric characteristics of CHA occur approximately in the same temperature interval as the analogous features of phlogopite; moreover, the values of losses are also close in magnitude.

In conclusion, it must be noted that particular values of the permittivity and loss factors of CHA may vary depending on the conditions of sample preparation, apparently, under the action of the aforementioned factors affecting the dielectric characteristics [7, 8]. However, the general character of the temperature variation of ε and $\tan\delta$ determined by the structural features and typical defects formed during preparation of the CHA samples are well reproduced.

The obtained results may be used in various applications, in particular, for identification of the CHA

implants and the optimization of electric stimulation of the implantation process.

REFERENCES

1. A. M. Smolegovskiĭ, *History of Crystal Chemistry of Phosphates* (Nauka, Moscow, 1986), pp. 49–98.
2. L. L. Hench, J. Am. Ceram. Soc. **74** (7), 1487 (1991).
3. V. P. Orlovskiĭ, Zh. A. Ezhova, and G. V. Rodicheva, Zh. Neorg. Khim. **37** (4), 881 (1992).
4. H. Suda, M. Yashima, L. Kakihana, *et al.*, J. Phys. Chem. **99** (6), 6752 (1995).
5. N. Hitmi, C. LaCabanne, and R. A. Younq, J. Phys. Chem. Solids **45** (6), 701 (1984).
6. N. Hitmi, C. LaCabanne, and R. A. Younq, J. Phys. Chem. Solids **47** (6), 533 (1986).
7. J. Zhan, X. Zhanq, J. Chen, *et al.*, J. Mater. Sci. **4**, 83 (1993).
8. E. C. M. Driessens, *Bioceramics of Calcium Phosphate*, Ed. by K. de Groot (CRC Press, Boca Raton, 1983).
9. G. M. Skanavi, *Physics of Dielectrics (Weak Field Region)* (Fizmatgiz, Moscow, 1958).

Translated by P. Pozdeev

Technical Physics Letters, Vol. 27, No. 8, 2001, pp. 632–634. Translated from Pis'ma v Zhurnal Tekhnicheskoĭ Fiziki, Vol. 27, No. 15, 2001, pp. 27–32.

Acoustic Emission during Heating of Strained Aluminum

V. A. Plotnikov

Altai State University, Barnaul, Russia

e-mail: phys@dcn-asu.ru

Received January 19, 2001

Abstract—The phenomenon of acoustic emission during annealing of preliminarily strained polycrystalline aluminum was observed. Although processes accompanying the metal annealing belong to thermoactivated (microscopic motion, diffusion) phenomena, the acoustic oscillations are generated in the events of spontaneous macroscopic motions of grain boundaries. This is confirmed by the results of analyzing the effective activation energy and the investigation of the grain boundary structure. © *2001 MAIK "Nauka/Interperiodica".*

Introduction. Among the large variety of the acoustic activity manifestations observed the course of a moderate-rate annealing of deformed aluminum samples, a special place belongs to the process of recrystallization in the material preliminary strained to a nearly critical level. Figure 1 shows fragments of the acoustic emission intensity dN/dt (count rate) kinetics demonstrating the case when the emission is caused by this process development. The curves presented in Fig. 1 were recorded during three cycles of a short-time heating to 600°C followed by cooling to 20°C.

An important feature of the acoustic emission generation and, hence, of the metal structure evolution is the presence of two special regions in the curves corresponding to the low-temperature (20–250°C) and high-temperature (250–600°C) intervals. In the high-temperature region, the emission intensity grows with the temperature to reach a maximum value at 600°C. The isothermal treatment at 600°C led to a gradual decrease in the intensity, which is apparently explained by the decreasing rate of migration of the grain boundaries. Another feature is that the acoustic emission intensity is retained on a high level during the second cycle of heating to 600°C. A significant decrease in the emission intensity level is observed only on the third cycle. This behavior of the acoustic signal reflects certain features of the recrystallization process in aluminum strained on a critical level.

Eventually, the thermal treatment of strained polycrystalline aluminum leads to the degradation of the acoustic emission observed during repeated thermal cycles. Figure 1d shows the curve of the acoustic response measured after subsequent anneals. As expected, only a monotonic growth in the acoustic emission intensity, rather than a peak, is observed in the temperature range from 350 to 600°C.

Experimental methods. The acoustic emission data were analyzed so as to determine the effective activation energy of processes responsible for the acoustic signal generation. A procedure used to calculate the activation parameters from the analysis of the acoustic emission measured in a single nonisothermal annealing cycle was described elsewhere [1].

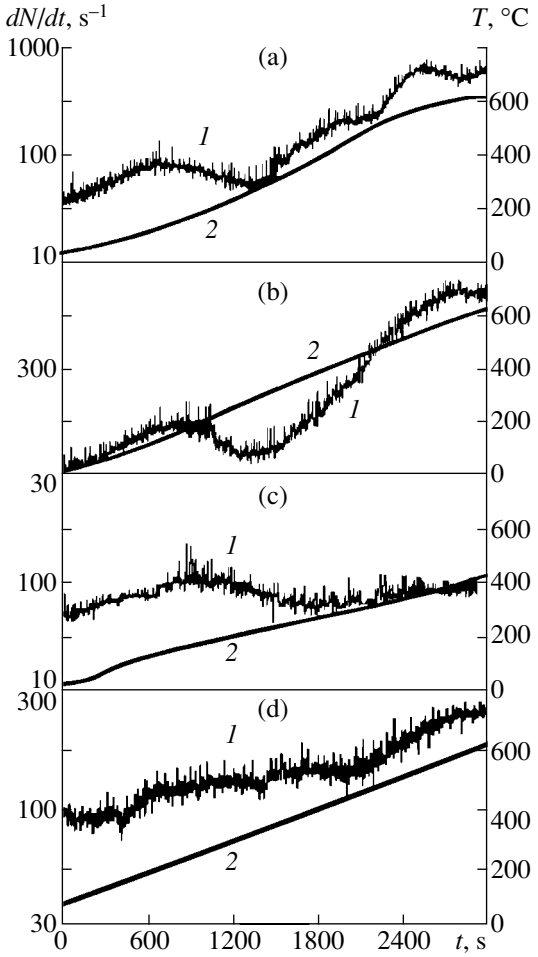

Fig. 1. Evolution of the acoustic emission manifestations in a strained aluminum sample in the course of (a–c) first to third sequential heating–cooling cycles, respectively, and (d) subsequent cycles: (*1*) time variation of the acoustic signal intensity (count rate); (*2*) time variation of the sample temperature.

1063-7850/01/2708-0632$21.00 © 2001 MAIK "Nauka/Interperiodica"

The results of this analysis are presented in Fig. 2 and summarized in the table. The activation energy values (see table) calculated for the low- and high-temperature regions are 19.0 and 47.2 kJ/mol, respectively; in the third cycle, the activation energy in the low-temperature region decreased to 13.4 kJ/mol, while the value in the high-temperature region increased up to 65.9 kJ/mol. Subsequent annealing cycles revealed two processes (Fig. 2d) characterized by low (8.3 kJ/mol) and high (74.3 kJ/mol) activation energies.

Discussion of results. Figure 3 shows a curve describing variation of the aluminum grain size with the temperature in the course of heating to 600°C at a rate of 1 K/s. A comparative analysis of the data presented in Figs. 1–3 and in the table shows that the behavior of the acoustic emission intensity in the 300–600°C temperature range is correlated with evolution of the grain boundary structure in the course of annealing of a strained aluminum sample. The character of variation of the calculated activation energies and the grain size in the temperature interval from 350 to 600°C is consistent with the process of grain boundary migration in the course of recrystallization [2].

Annealing of the aluminum samples in the 20–250°C temperature interval is accompanied by a low-intensity acoustic emission, while the process responsible for this emission is characterized by a low activation energy (see table). The existence of the low-temperature acoustic emission in aluminum is apparently related to a high energy of defects (stacking faults), which leads to the intensive migration of dislocations and their interactions with each other and with the grain boundaries [3–5].

On heating to high temperatures, only the migration of grain boundaries is possible with an activation energy close to that of the self-diffusion process [4, 5]. It should be noted, however, that equality of the activation energies by no means implies that the grain boundary migration reduces to diffusion. We may only speak of the diffusion-controlled processes. The group processes considered in this context include the collective and cooperative transitions shifting a grain boundary (considered as a macroscopic object) to a new position [6, 7].

According to [3], the average velocity of migration of a single grain boundary may vary between 10^{-2} and 10^{-5} cm/s. However, actual migration in the frontal direction proceeds by spontaneous movements of the whole boundary or its fragments [2–4], so that the average velocity values do not correspond to the real velocities of these spontaneous (jumplike) displacements. The velocity of spontaneous motions is large and, probably, comparable with the velocity of elastic waves in a given crystalline medium (this conclusion is indirectly confirmed by observations of the "instantaneous" appearance of a recrystallization nucleus up to 1 μm in size [3]). The range of such boundary movements may vary, especially at low temperatures [2].

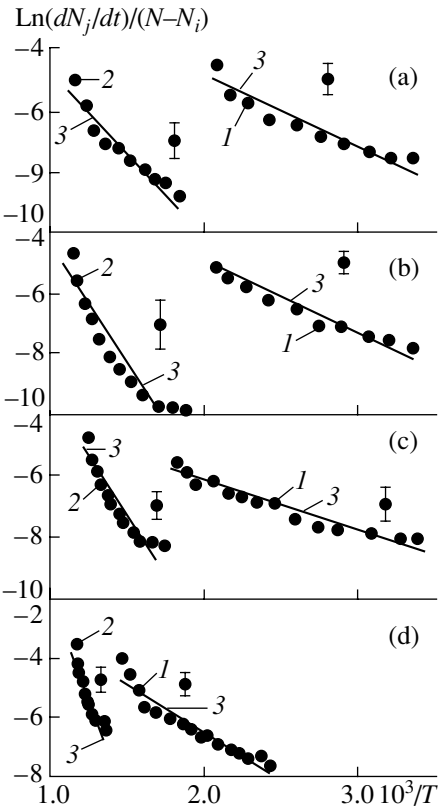

Fig. 2. Diagrams illustrating determination of the effective activation energy of (*1*) low-temperature and (*2*) high-temperature processes involved in the sample annealing (parts a–d refer to Figs. 2a–2d, respectively); solid lines *3* show linear approximations of the experimental plots.

The above considerations suggest that the observed acoustic emission is most probably generated at special time instants in response to the spontaneous motion of a grain boundary related to its stopping. In this case, there are two possible variants of the acoustic pulse production which are related to the stopping and transition processes. The relative contributions of these variants depend significantly on the ratio of the spontane-

Effective activation energies of the acoustic emission during annealing of strained aluminum

Annealing stage	Activation energy, kJ/mol		Temperature interval	
	Q_1	Q_2	ΔT_1, °C	ΔT_2, °C
Cycle 1	19.3 ± 1.0	47.2 ± 3.7	25–260	270–600
Cycle 2	19.0 ± 1.0	61.9 ± 3.7	25–270	270–600
Cycle 3	13.4 ± 0.7	65.9 ± 3.3	20–280	300–600
Subsequent cycles	8.4 ± 0.6	74.3 ± 8.2	60–350	400–600

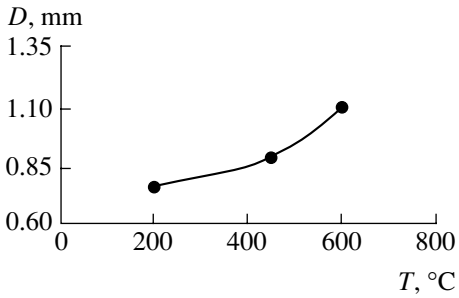

Fig. 3. The plot of grain size versus nonisothermal annealing temperature (heating rate, 1 K/s) for a polycrystalline aluminum sample strained to 5%.

ous boundary motion velocity to the elastic wave velocity. This mechanism coincides with the dynamic mechanism of acoustic signal generation in the events of spontaneous (microexplosion) motion of the phase boundary in the course of martensite transformations [8]. Moreover, the acoustic signal observed in the course of annealing confirms the data [6, 7] concerning specific collective and cooperative (correlated) group events in the course of migration of a grain boundary considered as a macroscopic object.

REFERENCES

1. V. A. Plotnikov, *The Nature of Acoustic Emission during Annealing of Metallic Materials* (Tomsk, 1992), Available from VINITI No. 606-B92.
2. B. S. Bokshteĭn, Ch. V. Kopetskiĭ, and L. S. Shvindlerman, *Thermodynamics and Kinetics of Grain Boundaries in Metals* (Metallurgiya, Moscow, 1986).
3. S. S. Gorelik, *Recrystallization of Metals and Alloys* (Metallurgiya, Moscow, 1978).
4. Ch. V. Kopetskiĭ, A. N. Orlov, and L. K. Fionova, *Grain Boundaries in Pure Metals* (Nauka, Moscow, 1987).
5. O. A. Kaĭbyshev and R. Z. Valiev, *Grain Boundaries and Properties of Metals* (Metallurgiya, Moscow, 1987).
6. Ch. V. Kopetskiĭ, V. G. Sursaeva, and L. S. Shvindlerman, Fiz. Tverd. Tela (Leningrad) **21** (2), 401 (1979) [Sov. Phys. Solid State **21**, 238 (1979)].
7. D. A. Molodov, B. B. Straumal, and L. S. Shvindlerman, Fiz. Tverd. Tela (Leningrad) **26** (4), 1033 (1984) [Sov. Phys. Solid State **26**, 629 (1984)].
8. V. A. Plotnikov, Pis'ma Zh. Tekh. Fiz. **25** (13), 15 (1999) [Tech. Phys. Lett. **25**, 512 (1999)].

Translated by P. Pozdeev

Technical Physics Letters, Vol. 27, No. 8, 2001, pp. 635–637. Translated from Pis'ma v Zhurnal Tekhnicheskoĭ Fiziki, Vol. 27, No. 15, 2001, pp. 33–37.

The Wave Collapse Analyzed for the Nonlinear Klein–Gordon Equation with Periodic Boundary Conditions

N. M. Zubarev

Institute of Electrophysics, Ural Division, Russian Academy of Sciences, Yekaterinburg, 620016 Russia
e-mail: nick@ami.uran.ru

Received February 2, 2001

Abstract—The integral estimation method is used to study the wave collapse dynamics for the Klein–Gordon equation with a nonlinearity of the general form in the case of periodic boundary conditions. Sufficient integral criteria (generalizing the known ones) for the wave collapse are formulated. © *2001 MAIK "Nauka/Interperiodica".*

The Klein–Gordon equation for the complex field $A(x, t)$ involving a destabilizing nonlinearity is used to describe explosive instabilities of the surface of a liquid metal placed in an external electric field [1], the charged surface of a dielectric liquid [2], the tangential discontinuity according to the Kelvin–Helmholtz mechanism [3], etc. Earlier [3, 4], it was demonstrated that constructing ordinary differential inequalities majorizing the original partial differential equation is an effective method for studying the wave field singularities (i.e., the wave collapses) described by the Klein–Gordon equation.

Here, we consider the case of periodic boundary conditions: the field A evolves within an interval of $0 \le x \le L$, where L is the period. Using the integral estimation method, a differential inequality can be derived for the period-averaged field $a(t) = (L^{-1}\int_0^L |A|^2\,dx)^{1/2}$. This inequality offers a generalization to formulas proposed in [3, 4] and allows us to formulate sufficient integral criteria of the wave collapse, that is, to determine the initial distributions of the fields A and A_t leading to the unbounded growth of the average field a over a limited period of time. Based on these general conditions, it is possible to carry out a comparative analysis of the previously known criteria.

Let the nonlinear Klein–Gordon equation be written as

$$A_{tt} = A_{xx} + AU'(|A|^2), \tag{1}$$

where $U'(y) = dU/dy$ and $U(y)$ is a function such that $F(y, s) = zU'(y) - sU(y)$ is a function of the variable $y > 0$, which is convex downward within the parameter interval $1 \le s_1 \le s \le s_2$. Note that conditions imposed on the function U do not restrict the generality of the problem under study: these conditions are naturally satisfied in almost all cases of interest (see, e.g., [4]). In particular, the complex Klein–Gordon equation with a cubic nonlinearity (the $|\phi|^4$ model), corresponds to $s_1 = 1$ and $s_2 = 2$.

By analogy with [3, 4], we consider the time evolution of the norm $X(t) = \int_0^L |A|^2\,dx \ge 0$. Differentiating the norm X twice with respect to t and summing up the resulting relationships with the expression for the energy of complex field

$$H = \frac{1}{2}\int_0^L [|A_t|^2 + |A_x|^2 - U(|A|^2)]\,dx$$

(representing an integral of motion for Eq. (1)) multiplied by $4s$, we obtain:

$$X_{tt} + 4sH = 2(1+s)\int_0^L |A|_t^2\,dx$$
$$+ 2(s-1)\int_0^L |A_x|^2\,dx + 2\int_0^L F(|A|^2, s)\,dx.$$

Applying the Cauchy–Bunyakowsky inequality to functions $|A|$ and $|A|_t$ yields $4X\int_0^L |A|_t^2\,dx \ge X_t^2$. Next, since F is a convex downward function, we obtain from the Jensen integral inequality that $\int_0^L F(|A|^2, s)dx \ge LF(X/L, s)$. It is also evident that $\int_0^L |A_x|^2\,dx \ge 0$. As a result, we arrive at the differential inequality

$$X_{tt} + 4sH \ge \frac{1+s}{2}\frac{X_t^2}{X} + 2LF(X/L, s), \tag{2}$$

which is valid for arbitrary $s_1 \le s \le s_2$.

1063-7850/01/2708-0635$21.00

It should be noted that inequalities such as (2) appear in formulating sufficient collapse conditions for the nonlinear Schrödinger equation [5, 6], various modifications of the Boussinesq equation [7], etc. Earlier, Maslov and Shagalov [4] considered the dynamics of the wave collapse for the scalar nonlinear Klein–Gordon equation under the assumption that the perturbation is localized in a certain finite domain and derived Eq. (2) for the particular case of $s = 1$. Kuznetsov and Lushnikov [3] derived an inequality corresponding to the particular case of $s = s_2 = 2$ in the $|\phi|^4$ model. A distinctive feature of inequality (2) is the free parameter s, which will be used below to optimize approximation (2) of Eq. (1).

Let us analyze differential inequality (2) under the assumption that norm X monotonically increases with time, that is, $X_t \geq 0$ for $t \geq t_0$, where t_0 is the initial time instant. Multiplying this inequality by X_t/X^{s+1}, we obtain

$$\frac{d}{dt}\frac{\Delta(t)}{X^s} \geq 0,$$

where

$$\Delta(t) = \frac{1}{4}\frac{X_t^2}{X} - 2H - LU(X/L).$$

Then, evidently, the following inequality is valid:

$$\Delta(t) \geq \frac{X^s(t)}{X^s(t_0)}\Delta(t_0). \qquad (3)$$

Now expression (2) can be rewritten as

$$X_{tt} \geq \frac{1}{2}\frac{X_t^2}{X} + 2XU'(X/L) + 2s\Delta(t).$$

In this formula, we grouped together all terms proportional to s. Eliminating function $\Delta(t)$ with the help of formula (3), we obtain

$$X_{tt} \geq \frac{1}{2}\frac{X_t^2}{X} + 2XU'(X/L) + 2s\Delta(t_0)\frac{X^s(t)}{X^s(t_0)}. \qquad (4)$$

Since the norm X is assumed to be monotonically increasing and, consequently, $X(t)/X(t_0) \geq 1$, function $s(X(t)/X(t_0))^s$ also monotonically increases with s. Then, for $\Delta(t_0) > 0$, the right-hand side of inequality (4) will be maximal and, consequently, the approximation will be optimal at the maximum possible value of parameter s (i.e., at $s = s_2$). On the contrary, for $\Delta(t_0) < 0$, inequality (4) will be optimal at the minimum possible s (i.e., at $s = s_1$). This simple criterion uniquely indicates the initial conditions for which one should use the collapse criteria based on the approach proposed in [4] (which must be corrected for the case of the complex field A) and the conditions for which criteria derived by analogy with [3] will be more general.

To alleviate the analysis of inequality (4), we introduce the parameter $a(t) = \sqrt{X/L}$ representing the complex field A averaged over the period L. Then,

$$a_{tt} \geq s_0\delta_0 a^{2s_0-1} + aU'(a^2), \qquad (5)$$

where $\delta_0 = \Delta(t_0)L^{-1}a_0^{-2s_0}$ and s_0 denotes the optimum value of parameter s determined by the expression

$$s_0 = \frac{s_2 + s_1}{2} + \frac{s_2 - s_1}{2}\mathrm{sgn}(\delta_0).$$

Inequality (5) can be conveniently rewritten in the form of the second Newton's law:

$$a_{tt} \geq -\frac{\partial P(a)}{\partial a}, \quad P(a) = -\frac{1}{2}[\delta_0 a^{2s_0} + U(a^2)],$$

where a and P play role of the coordinate and the potential energy of a "particle." Also introduce the quantity $E(t) = a_t^2/2 + P(a)$, which represents the total mechanical energy of this "particle."

Thus, partial differential equation (1) for the complex field $A(x, t)$ with the mean energy density $h = H/L$ can be associated with ordinary differential inequality (5) for the period-averaged field $a(t) = (L^{-1}\int_0^L |A|^2\,dx)^{1/2}$. This inequality describes the motion of a Newtonian particle with the energy E in a given potential. Remarkably, at the initial time instant, the quantities h and E are equal to each other (i.e., $E(t_0) = h$) and expressions (1) and (5) have similar structures. This fact clarifies the results of studying wave-collapse processes described by the nonlinear Klein–Gordon equation which are obtained from considering the motion of an effective "particle." Since the "particle" has positive speed at $X_t > 0$, we can multiply (5) by a_t and integrate the obtained expression with respect to t. As a result, we obtain that $E(t) \geq E(t_0)$; i.e., the "particle" energy increases in the process of motion. It is clear that a sufficient criterion for an infinite growth of the quantity a over a finite time is the condition that the "particle" does not meet a potential wall even if $E_t = 0$; i.e., the condition $P(a) < h$ at $a \geq a_0$.

In conclusion, we should note that all the results of this work can be readily extended to the multidimensional case. As was already noticed in [3] for the $|\phi|^4$ model, the behavior of the system under study is almost independent of the space dimensionality.

Acknowledgments. The author is grateful to E.A. Kuznetsov, P.M. Lushnikov, E.M. Maslov, and A.G. Shagalov for fruitful discussions.

This work was supported by the Russian Foundation for Basic Research (project no. 00-02-17428) and the INTAS Foundation (project no. 99-1068).

REFERENCES

1. N. M. Zubarev, Pis'ma Zh. Tekh. Fiz. **25** (21), 65 (1999) [Tech. Phys. Lett. **25**, 872 (1999)].
2. L. P. Gor'kov and D. M. Chernikova, Dokl. Akad. Nauk SSSR **228** (4), 829 (1976) [Sov. Phys. Dokl. **21**, 328 (1976)].
3. E. A. Kuznetsov and P. M. Lushnikov, Zh. Éksp. Teor. Fiz. **108** (2), 614 (1995) [JETP **81**, 332 (1995)].
4. E. M. Maslov and A. G. Shagalov, Phys. Lett. A **239**, 46 (1998).
5. E. A. Kuznetsov, J. J. Rasmussen, K. Rypdal, and S. K. Turitsyn, Physica D (Amsterdam) **87**, 273 (1995).
6. P. M. Lushnikov, Pis'ma Zh. Éksp. Teor. Fiz. **62** (5), 447 (1995) [JETP Lett. **62**, 461 (1995)].
7. S. K. Turitsyn, Phys. Rev. E **47** (2), R796 (1993).

Translated by A. Kondrat'ev

Technical Physics Letters, Vol. 27, No. 8, 2001, pp. 638–641. Translated from Pis'ma v Zhurnal Tekhnicheskoĭ Fiziki, Vol. 27, No. 15, 2001, pp. 38–45.

The *T–P–H* Effects on the Magnetoresistance of $La_{0.7}Ca_{0.3}Mn_{1.0}O_{3-\delta}$ Ceramics and Films

S. S. Kucherenko, V. I. Mikhaĭlov, V. P. Pashchenko, P. I. Polyakov*, V. A. Shtaba, and V. P. D'yakonov

Donetsk Physicotechnical Institute, National Academy of Sciences of Ukraine, Donetsk, Ukraine

** e-mail: poljakov@host.dipt.donetsk.ua*

Received March 6, 2001

Abstract—Effects of the temperature (T = 77–325 K), high hydrostatic pressures (P = 0–2.1 GPa), and magnetic fields (H = 0–8 kOe) on the electric resistance (R) and magnetoresistance ($\Delta R/R_0$) were studied in $La_{0.7}Ca_{0.3}Mn_{1.0}O_{3-\delta}$ based ceramics and single crystal films. A significant difference between the magnetoresistance peak temperatures (T_P) observed in the ceramic and film samples is explained by their different deviations from the stoichiometry with respect to oxygen, that is, by a greater concentration of anion vacancies in the film perovskite structure. An increase in the magnetic field strength H and the pressure P leads to a decrease in the electric resistance R. The magnetoresistance grows with increasing field strength H and decreasing pressure P. A growth in the hydrostatic pressure leads to an increase in the T_P value by 12 K for the ceramics and by 40 K for the films. © *2001 MAIK "Nauka/Interperiodica".*

Rare-earth (RE) manganites with a perovskite structure exhibiting the giant magnetoresistance (GMR) effect [1, 2] are promising materials for the development of modern technologies. The materials featuring the GMR effect are used both in the form of bulk ceramics [3] or single crystals [4] and in the form of thin films obtained by various methods [5–7]. Among the RE manganites showing a high GMR effect and possessing good technological properties, the best prospects are related with manganite–lanthanum perovskites doped with calcium [8] and strontium [9] with the general formula $La_{1-x}Mn_x^{2+}Mn_{1-x}^{3+}Mn_x^{4+}O_3^{2-}$, where Me^{2+} = Ca^{2+} or Sr^{2+}.

From both the applied and fundamental standpoints, it is especially important to study the effects of temperature T, high hydrostatic pressures P, and applied magnetic field strength H on the magnetoresistance $\left(\frac{\Delta R}{R_0} = \frac{R_0 - R_H}{R_0}\right)$ of polycrystalline targets and single crystal films grown on substrates by laser sputtering of the corresponding ceramic targets [10]. Data on the simultaneous effect of *T–P–H* upon the magnetoresistance of such materials are restricted [11–13]. For this reason, the results of our comparative investigations performed on bulk targets and films in a broad range of temperatures, pressures, and magnetic field strengths are very important.

The experiments were performed on the samples of $La_{0.7}Ca_{0.3}MnO_{3-\delta}$ ceramics synthesized from powder by a double 20-h firing at 900 and 950°C, followed by sintering pressings at T_{SP} = 1220°C. We have also studied the single crystal films of the same cation composition. The films with a thickness of 915 Å were obtained by the laser sputtering of single-phase ceramic targets with deposition onto $LiAlO_3$ substrates.

The phase composition and the crystal structure type and parameters were determined by the X-ray diffraction measurements performed on a DRON-2 diffractometer using Cu$K\alpha$ radiation. According to these data, the samples possessed a nearly cubic perovskite-like structure ($Pm3m$) with a crystal lattice parameter a = 3.878 Å. The saturation magnetization of the samples at 77 K was M = 82 emu/g. The wide-band NMR frequency of ^{55}Mn (F = 375 MHz) falls between the frequencies of Mn^{3+} (F = 420 MHz) and Mn^{4+} (F = 310 MHz), which is indicative of a high-frequency electron exchange between Mn^{3+} and Mn^{4+} ions occurring in the octahedral positions with an average valence close to $\bar{\omega}$ = 3.4. The electric resistance of thin films was measured by the four-point-probe technique in a broad range of temperatures (T = 77–325 K), pressures (P = 0–2.1 GPa), and magnetic field strengths (H = 0–8 kOe). The measurements at high hydrostatic pressures were performed in a high-pressure chamber [14]. The experimental errors of determination were 1% for the temperature, 1.5% for the magnetic field strength, 3% for the pressure, 0.01% for the electric resistance, and 0.1% for the magnetoresistance $\Delta R/R_0$.

According to the experimental data obtained, the effects of the magnetic field strength and high hydrostatic pressures on the electric resistance possess the same character for both ceramics and films: as the H and P values grow, the sample resistance decreases. At the same time, effects of these factors on the magne-

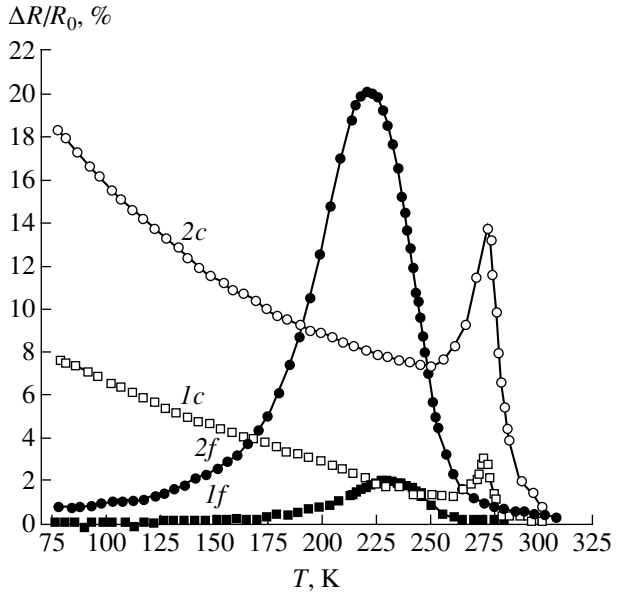

Fig. 1. Temperature dependence of the magnetoresistance of (*1c*, *2c*) ceramic and (*1f*, *2f*) film samples of $La_{0.7}Ca_{0.3}Mn_{1.0}O_{3-\delta}$ measured at $P = 0$ and the magnetic field strengths of $H = 2$ (*1c*, *1f*) and 8 kOe (*2c*, *2f*).

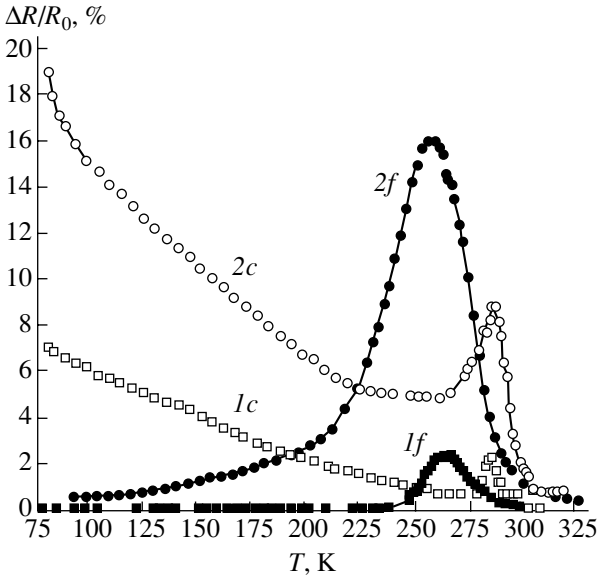

Fig. 2. Temperature dependence of the magnetoresistance of (*1c*, *2c*) ceramic and (*1f*, *2f*) film samples of $La_{0.7}Ca_{0.3}Mn_{1.0}O_{3-\delta}$ measured at the pressures of $P = 1.7$ (*1c*, *2c*) and $P = 2.1$ GPa (*1f*, *2f*) and the magnetic field strengths of $H = 2$ (*1c*, *1f*) and 8 kOe (*2c*, *2f*).

toresistance are opposite: $\Delta R/R_0$ grows with increasing H and drops with increasing P. Figure 1 illustrates the temperature dependence of $\Delta R/R_0$ measured for the ceramic (subscript c) and film (subscript f) samples at $P = 0$ and a field strength of $H = 2$ and 8 kOe. Figure 2 shows the analogous data measured at $P = 1.7$ GPa (for ceramics) and 2.1 GPa (for films) in the same fields. A comparison of these results showed that the $\Delta R/R_0$ peak at $P = 0$ is observed at a higher temperature for the ceramic sample ($T_P' = 275$ K) than for the single crystal film ($T_P'' = 225$ K). The measurements under high hydrostatic pressures $P' = 1.7$ GPa and $P'' = 2.1$ GPa yielded $T_P' = 285$ K and $T_P'' = 265$ K, respectively. In a weak magnetic field ($H = 2$ kOe), the magnetoresistances of ceramic and film samples are close. As the field strength increases ($H = 8$ kOe), the $\Delta R/R_0$ value in the film becomes significantly greater than that in the bulk ceramics. The data in Figs. 1 and 2 show that a maximum variation of the $\Delta R/R_0$ value in response to P and H is observed in the region of the metal–semiconductor phase transition (T_m) and near the magnetoresistance peak (T_P), that is, at temperatures corresponding to the maximum electric resistance and magnetoresistance, respectively. An increase in the magnetic field strength from $H = 2$ to 8 kOe leads to a significant growth of $\Delta R/R_0$. In ceramic samples, the magnetoresistance increases from 3 to 14% at $P = 0$ and from 2 to 9% at $P = 1.7$ GPa. In the film samples, the same change in the field strength increases the magnetoresistance from 2 to 20% at $P = 0$ and from 2 to 16% at $P = 2.1$ GPa.

In films, the magnetoresistance peak temperature changes from $T_P'' = 225$ K ($H = 2$ kOe) to 220 K ($H = 8$ kOe). In the ceramics, this magnetoresistance peak temperature (T_P') is considerably higher and is virtually not affected by the field strength. A significant difference between the T_P values of the ceramic and film samples are explained, in our opinion, by their different deviations from the stoichiometry with respect to oxygen. This is related to the variable oxygen concentration in manganite–lanthanum perovskites of the $La_{0.7}Ca_{0.3}MnO_{3-\delta}$ type: the oxygen content in an underoxidized film must be lower than that in a ceramic ($\delta_f > \delta_c$). This explanation agrees with the data reported for $LaMnO_{3+\delta}$ [15], $La_{1-x}Mn_{1+x}O_{3\pm\delta}$ [16], $La_{0.7}Sr_{0.3}MnO_{3-\delta}$ and $La_{1-x}Ca_xMnO_{3-\delta}$ [17, 18]. It was demonstrated [16] that perovskites may differ both in the oxygen content and in the defect structure possessing anion and cation vacancies. This factor may also contribute to the different temperature variation of $\Delta R/R_0$ observed in ceramics and films in the 77–250 K range.

Figure 3a illustrates the effect of the magnetic field strength on the phase transition temperature T_m of the ceramic samples, while Fig. 3b shows variation of the $T_P$values in both ceramics (open symbols) and films (filled symbols). An increase in H is accompanied by a significant, almost linear growth in T_m. The value of T_P exhibits a more complicated variation with the increasing field strength: the magnetoresistance peak shifts to higher temperatures in the ceramic samples and to lower temperatures in the films.

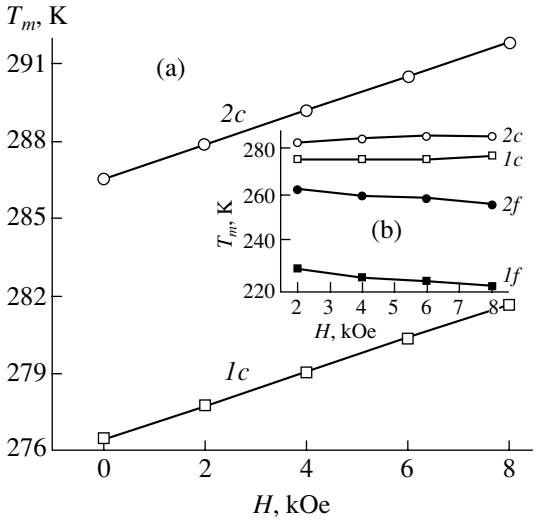

Fig. 3. Effect of the magnetic field strength on the peak temperatures of (a) electric resistance (T_m) and (b) magnetoresistance (T_P) in (*1c*, *2c*) ceramic and (*1f*, *2f*) film samples of $La_{0.7}Ca_{0.3}Mn_{1.0}O_{3-\delta}$ measured at the pressures of P = 0 (*1c*, *1f*), 1.7 GPa (*2c*), and 2.1 GPa (*2f*).

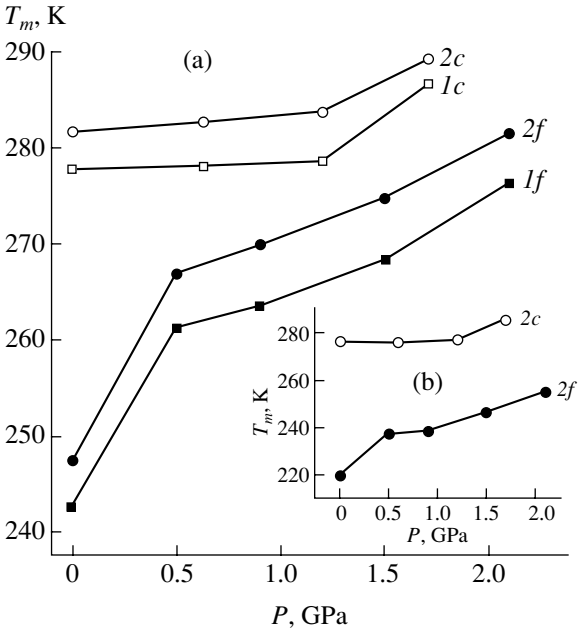

Fig. 4. Effect of the high hydrostatic pressure on the peak temperatures of (a) electric resistance (T_m) and (b) magnetoresistance (T_P) in (*1c*, *2c*) ceramic and (*1f*, *2f*) film samples of $La_{0.7}Ca_{0.3}Mn_{1.0}O_{3-\delta}$ measured for the magnetic field strengths of H = 2 (*1c*, *1f*) and 8 kOe (*2c*, *2f*).

The effect of high hydrostatic pressures on the T_m values of ceramics and films in various magnetic fields is illustrated in Fig. 4a. The pressure dependence of T_P at H = 8 kOe is presented in Fig. 4b. An increase in the hydrostatic pressure more significantly affects the T_m and T_P values of the film, which indicates that the pressure variations have a more pronounced effect upon the phase transitions in films than in ceramics. Note the bending point at P = 0.5 GPa in the plots of phase transition temperatures versus pressure for the film samples. The reasons for this behavior are unclear. We may only suggest that this feature can be explained either by a large anisotropy of the two-dimensional film samples or by the effect of anion vacancies related to a considerable deficit of oxygen ($\delta_f > \delta_c$) in the real structure of manganite–lanthanum perovskites [16]. At low (100–150 K) and high (300–320 K) temperatures ($T_P'' \ll T \ll T_P'$) far from the interval of phase transitions (200–275 K), the high hydrostatic pressures do not affect the magnetoresistance behavior. Near the phase transition (T_m), the applied pressure significantly decreases the magnetoresistance in both ceramics and films.

Thus, an analysis of our experimental results showed that increasing magnetic field strength and high hydrostatic pressures decrease the electric resistance of both ceramic and film samples. The temperatures of the metal–semiconductor phase transitions (T_m) and the magnetoresistance peaks (T_P) for the ceramics are higher by approximately 50 K than the analogous values for the films of the same cation composition $La_{0.7}Ca_{0.3}Mn_{1.0}O_{3-\delta}$. The magnetoresistances of the ceramic and film samples are close in a weak magnetic field (H = 2 kOe) and significantly differ in a stronger field (H = 8 kOe).

High hydrostatic pressures applied in the presence of a strong magnetic field (H = 8 kOe) decrease the magnetoresistance value in ceramics and films by 5% and 4%, and increase the magnetoresistance peak temperature T_P by 12 and 40 K, respectively. The effects of the magnetic field and high hydrostatic pressures are maximum in the vicinity of the phase transitions and decrease at both low and high temperatures (far from T_m and T_P).

Acknowledgments. The authors are grateful to A.V. Klimov for kindly providing the film samples.

REFERENCES

1. H. Y. Hwang, S. W. Cheong, P. G. Radaelli, *et al.*, Phys. Rev. Lett. **75** (5), 914 (1995).
2. É. L. Nagaev, Usp. Fiz. Nauk **166** (8), 833 (1996) [Phys. Usp. **39**, 781 (1996)].
3. G. C. Bhar, U. Chatterjee, K. Isakamoto, *et al.*, J. Magn. Magn. Mater. **188**, 180 (1998).
4. A. M. Kadomtseva, Yu. V. Popov, G. P. Vorob'ev, *et al.*, Fiz. Tverd. Tela (St. Petersburg) **42** (6), 1077 (2000) [Phys. Solid State **42**, 1110 (2000)].
5. V. N. Krivoruchko, V. P. Pashchenko, Yu. V. Medvedev, *et al.*, Phys. Lett. A **245**, 163 (1998).
6. Yu. P. Sukhorukov, N. N. Lashkareva, E. A. Gan'shina, *et al.*, Pis'ma Zh. Tekh. Fiz. **25** (14), 6 (1999) [Tech. Phys. Lett. **25**, 551 (1999)].
7. M. Fath, S. Freisem, A. A. Menovsky, *et al.*, Science **285**, 1540 (1999).

8. X. B. Chen, J. S. Zhu, G. H. Hwang, *et al.*, Phys. Status Solidi A **173**, 451 (1999).
9. X. Xiong, B. Dabrowski, O. Chmaissem, *et al.*, Phys. Rev. B **60** (14), 10186 (1999).
10. V. A. Berezin, V. I. Nikolaĭchik, and V. T. Volkov, Pis'ma Zh. Tekh. Fiz. **25** (10), 42 (1999) [Tech. Phys. Lett. **25**, 398 (1999)].
11. V. E. Arkhipov, V. S. Gaviko, K. M. Demchuk, *et al.*, Pis'ma Zh. Éksp. Teor. Fiz. **71** (3), 169 (2000) [JETP Lett. **71**, 114 (2000)].
12. K. Kamenev, G. Balakrishman, M. R. Lees, *et al.*, Phys. Rev. B **56** (5), 2285 (1997).
13. V. Moshnyaga, S. Klimm, K. Samwer, *et al.*, J. Appl. Phys. **88** (9), 5305 (2000).
14. A. V. Oleĭnik, P. I. Polyakov, and V. G. Synkov, Fiz. Tekh. Vys. Davleniĭ **4** (1), 88 (1994).
15. G. Subias, J. García, J. Blasco, *et al.*, J. Magn. Magn. Mater. **196**, 534 (1999).
16. V. P. Pashchenko, S. I. Khartsev, O. P. Cherenkov, *et al.*, Neorg. Mater. **35** (12), 1509 (1999).
17. H. L. Ju and K. M. Krishnan, Solid State Commun. **104** (7), 419 (1997).
18. L. Ghivelder, I. Abrego Castillo, N. McN. Alfrod, *et al.*, J. Magn. Magn. Mater. **189** (3), 274 (1998).

Translated by P. Pozdeev

Technical Physics Letters, Vol. 27, No. 8, 2001, pp. 642–643. Translated from Pis'ma v Zhurnal Tekhnicheskoĭ Fiziki, Vol. 27, No. 15, 2001, pp. 46–50.

A Water-Vapor Electric-Discharge Vacuum Ultraviolet Source

A. K. Shuaibov, L. L. Shimon, A. I. Dashchenko, and I. V. Shevera

Uzhgorod National University, Uzhgorod, Ukraine

e-mail: ishev@univ.uzhgorod.ua

Received February 21, 2001

Abstract—The optical emission from a longitudinal dc glow discharge in water vapors (P = 0.05–2.5 kPa) was studied in a wavelength range of λ = 130–350 nm. It is shown that the discharge in low-pressure water vapors can be used as a source of the vacuum UV (VUV) radiation in the 140–190 nm wavelength range. As the vapor pressure was increased to 2.5 kPa, the emission intensity decreased by one–two orders of magnitude and the main peaks shifted to λ = 286 and 306–315 nm. The bands of optical emission from the products of water decomposition agree in position with the emission band edges of the hydroxyl molecule. The obtained results are important for the development of a simple water-vapor electric-discharge VUV source. © *2001 MAIK "Nauka/Interperiodica".*

The products of dissociation of water molecules in both glow and high-frequency discharges serve as active media in the ecologically safe sources of UV radiation operating at a wavelength of 306.4 nm corresponding to the OH(A–X; 0–0) transition [1, 2]. Under certain conditions, this band dominates in the spectra of emission in the 300–1000 nm wavelength range of the electric discharges in mixtures of inert gases with water vapors. In order to avoid the formation of complexes based on the OH radicals or H_2O molecules, which reduce the efficiency of emission at the OH resonance frequency and decrease the discharge stability, Milenin *et al.* [3] recently recommended to employ mixtures containing a minimum amount of water vapors. Unfortunately, no optical characteristics of a glow discharge in water vapors (including the room-temperature saturated vapor) were reported in the above-cited papers.

Some medical applications [4] require optical sources operating in the region of wavelengths $\lambda \le 220$ nm. Such bands are present in the system of optical transitions of the OH radical [λ = 179.1 nm, OH(C–A); 122.3 nm OH(D–X)], but their relative intensities with respect to that of the OH(A–X) resonance are unknown. For this reason, it is important to study the optical emission in a broad range of wavelengths from discharge plasmas containing H_2O molecules in a wide interval of water vapor pressures. Below, we report on the results of investigations of the optical characteristics of a dc discharge plasma in water vapors in the 130–350 nm wavelengths range.

A longitudinal dc discharge in a quartz tube with an internal diameter of 7 mm was excited between electrodes spaced by 50 mm. The discharge tube was mounted in a buffer chamber with a volume of 10 dm^3. The chamber was connected via a CaF_2 crystal window to an 0.5-m vacuum monochromator possessing a spectral resolution of 0.7 nm. The emission was detected by a system analogous to that described in [5, 6]. The glow discharge was power supplied from a high-voltage rectifier ($I_{ch} \le 100$ mA). The water vapors were either admitted into the buffer chamber from a special reservoir at a pressure controlled in the P = 50–150 Pa range or obtained by evaporation from a cup with distilled water placed in the chamber (room-temperature saturated vapors, P = 1.5–2.5 kPa).

A normal regime of glow discharge in saturated water vapors was established at a discharge current of $I_{ch} \ge 30$ mA. The electric power supplied to the discharge was 40–50 W. At a low water vapor pressure, the discharge existed in the form of immobile striations with an interval of 5–7 mm between bright columns. Figure 1 shows the emission spectra of a glow discharge plasma in saturated and unsaturated water vapors. At a high vapor pressure, the major emission bands corresponded to λ_{max} = 185, 264, 286, and 306–315 nm. A decrease in the vapor pressure led to a significant redistribution of the relative band intensity, whereby the main emission occurred within broad bands in the vacuum UV (VUV) range at λ_{max} = 180/186 and 156 nm.

Under the experimental conditions, a considerable proportion of water vapors existed in the form of $(H_2O)_n$ clusters [3]. The main products of decomposition of both water molecules and their complexes were OH radicals [7] or molecular hydroxyl clusters. The most pronounced effect of such clusters on the optical characteristics of discharge was observed for saturated water vapors (Fig. 1a). In this case, the most intense band in the emission spectrum was observed at λ = 313 nm with a width of $\Delta\lambda_{1/2}$ = 9 nm. The other bands were shifted relative to edges of the characteristic bands of OH(C–A) at 179.1 nm (for λ_{max} = 180/186 nm) and OH(B–A) at 278 nm (for λ_{max} = 286 nm). The most shortwave band observed at λ = 143–164 nm correlates

Relative intensities J of the emission bands in the spectrum, of dc glow discharge in water vapors at various pressures

λ, nm	156	180–186	286	306–315
J, a.u. (P_{H_2O} = 0.1 kPa)	610	920	54	90
J, a.u. (P_{H_2O} = 2.5 kPa)	≤1	4	10	32

with the OH(B–X) transition. The observed emission bands can be related to the emission from excited complex molecules of the $(OH)_n^* \cdot (H_2O)_m$ type with $n \geq 2$ and $m \geq 0$.

Data on the relative intensities J of the emission bands in the spectra of dc glow discharge in water vapors at two pressures are presented in the table. The vapor pressure most significantly affects the emission intensity in the shortwave region (λ_{max} = 156, 180/186 nm). As can be seen from these data, the glow dc discharge in water vapors at low pressure effectively emits radiation with the wavelengths from 140 to 190 nm, which can be used for the development of simple VUV radiation sources. This source is close to the ArCl excimer lamp (λ = 175 nm) with respect to both efficiency and output power. The proposed sources require no inert gases and are of interest for operation under the working medium flow conditions.

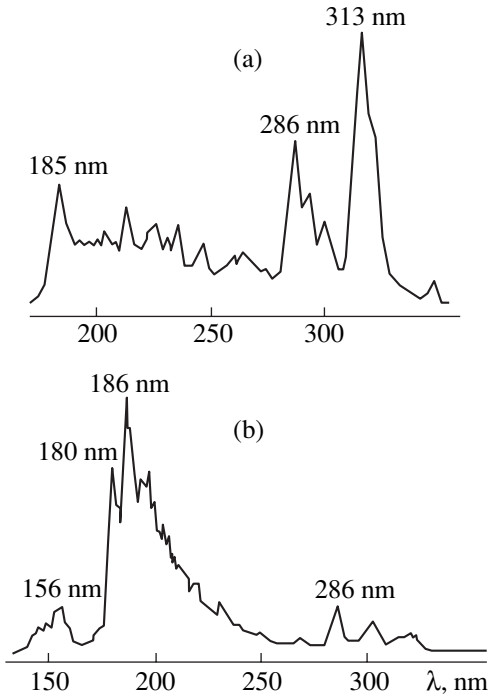

Fig. 1. The spectra of emission from a dc glow discharge plasma observed in water vapors at P = 2.5 (a) and 0.05–0.15 kPa.

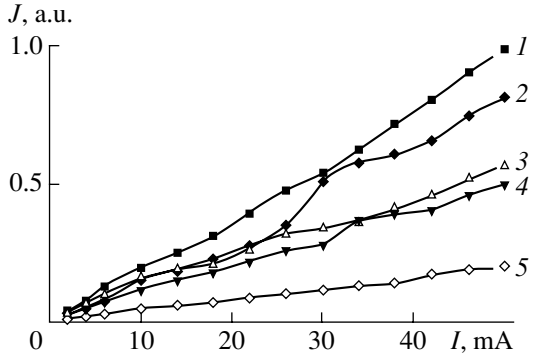

Fig. 2. The plots of emission band intensity versus discharge current in water vapors at P = 0.15 kPa for various bands: λ = 156 (*1*), 180 (*2*), 186 (*3*), 286 (*4*), 306–315 nm (*5*).

The plots of the emission intensity versus discharge current I_{ch} for all characteristic bands of the water-vapor plasma spectrum were close to linear (Fig. 2). When the discharge current increases from 3 to 50 mA, the intensities of all emission bands grow. This fact indicates that direct electron excitation processes dominate in the discharge medium studied.

Thus, we have demonstrated that the optical emission from a dc glow discharge in saturated water vapors is characterized by a number of wide bands in the region from 130 to 350 nm (λ_{max} = 313, 286 nm). As the vapor pressure decreases to within 50–150 Pa, the main emission concentrates in the molecular bands (correlated with the C-A and B-X transitions in OH radicals). This result is of interest for the development of ecologically safe VUV sources operating in the 140–190 nm wavelength range.

REFERENCES

1. A. Ya. Vul', S. V. Kidalov, V. M. Milenin, *et al.*, Pis'ma Zh. Tekh. Fiz. **25** (1), 10 (1999) [Tech. Phys. Lett. **25**, 4 (1999)].
2. A. Ya. Vul', S. V. Kidalov, V. M. Milenin, *et al.*, Pis'ma Zh. Tekh. Fiz. **25** (8), 62 (1999) [Tech. Phys. Lett. **25**, 321 (1999)].
3. V. M. Milenin, N. A. Timofeev, A. Ya. Vul', *et al.*, Pis'ma Zh. Tekh. Fiz. **26** (18), 63 (2000) [Tech. Phys. Lett. **26**, 835 (2000)].
4. I. A. Soloshenko, V. V. Tsiolko, V. V. Khomich, *et al.*, Fiz. Plazmy **26** (9), 845 (2000) [Plasma Phys. Rep. **26**, 792 (2000)].
5. A. K. Shuaibov and A. I. Dashchenko, Kvantovaya Élektron. (Moscow) **30** (3), 279 (2000).
6. A. K. Shuaibov, L. L. Shimon, A. I. Dashchenko, and I. V. Shevera, Teplofiz. Vys. Temp. **38** (3), 386 (2000).
7. G. A. Baranov, A. K. Zinchenko, M. G. Lednev, and F. P. Podtykin, Khim. Vys. Énerg. **22** (6), 532 (1988).

Translated by P. Pozdeev

Technical Physics Letters, Vol. 27, No. 8, 2001, pp. 644–646. Translated from Pis'ma v Zhurnal Tekhnicheskoĭ Fiziki, Vol. 27, No. 15, 2001, pp. 51–56.

Multielement IR Sources with Alternating Contrast

V. K. Malyutenko, S. S. Bolgov, and O. Yu. Malyutenko

Institute of Semiconductor Physics, National Academy of Sciences of Ukraine, Kiev, Ukraine

e-mail: malyut@isp.kiev.ua

Received March 11, 2001

Abstract—An array of InSb-based IR sources, employing the principle of excitation of positive and negative luminescence under conditions of the magnetoconcentration effect, was studied by a thermal imaging technique. The IR array allows a positive, negative, or alternating effective temperature contrast to be simulated in a wavelength range of up to 7 μm. The effective temperature of the negative electroluminescence sources operating at room temperature can be decreased by 20 K. Devices of this type can be used as IR test patterns with controlled contrast for calibrating optoelectronic devices with respect to spatial, temperature, and time resolution. © *2001 MAIK "Nauka/Interperiodica".*

Multielement radiation sources based on semiconductor light-emitting diodes (LEDs) are widely used in data displays operating in the visible spectral range [1]. Progress in infrared (IR) techniques required the development of the multielement sources capable of creating spatially inhomogeneous IR radiation fields for testing the optoelectronic devices, in particular, thermal imaging systems. Recently, Beasley *et al.* [2] reported on the LED arrays operating at a wavelength of up to 4.7 μm based on the positive luminescence excitation. However, modern simulation techniques require more longwave sources with large emitter areas and highly uniform emission from individual elements. In addition, these devices must be capable of creating both positive and negative radiation contrasts relative to the background emission level.

We have used a thermal imaging technique to study an array of IR sources based on a narrow-bandgap semiconductor and operating on the principle of positive and negative luminescence excitation under conditions of the magnetoconcentration effect. A special feature of this effect is the possibility of creating regions considerably enriched with and depleted of charge carriers in a semiconductor plate exposed to crossed electric (E) and magnetic (H) fields [3]. Enrichment of a subsurface region of the emitting crystal face with a small surface recombination rate leads to the excitation of the positive interband luminescence. A change in direction of one of the fields at the same face creates a depletion region and gives rise to a negative luminescence manifested by a decrease in the emission intensity relative to the equilibrium thermal radiation level [4].

The IR emitter elements were made of p-InSb with N_a–$N_d = 10^{15}$ cm^{-3}. The array, based on a thin (60 μm-thick) semiconductor plate with asymmetrically treated surfaces (mechanical polishing vs. etching in an CP-4 etchant), was prepared using a photolithographic technique. The array was composed of 16 elements (see the inset in Fig. 1) sized 0.5 × 16 mm and spaced by 0.5 mm. The ohmic contacts were obtained by vacuum deposition of pure In. The emitting array package with BaF_2 window was placed between poles of an electric magnet.

The room-temperature IR emission was detected in the 3–5 μm working wavelength range with a scanning thermal imaging camera and reproduced in the form of thermograms. The imaging system was calibrating using a blackbody in the same working spectral range, which allowed an effective temperature T_{eff} simulated by the array to be determined. A special software package allowed each thermogram to be displayed by a

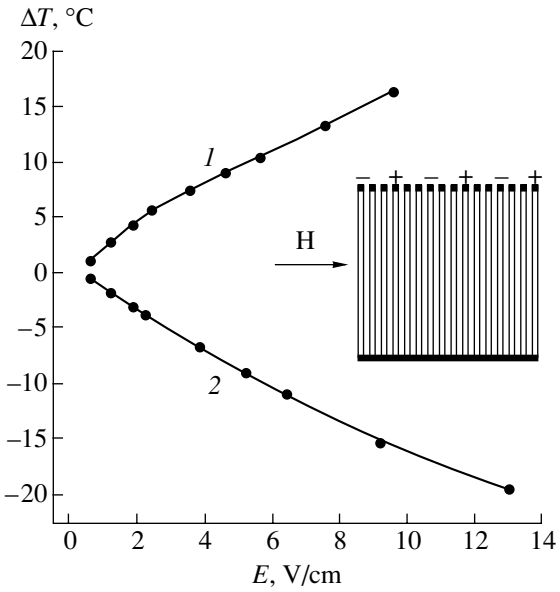

Fig. 1. The field dependence of the effective temperature of an IR array element in the regime of (*1*) positive and (*2*) negative luminescence excitation (H = 3.5 kG). The inset shows a schematic diagram of the array.

1063-7850/01/2708-0644$21.00 © 2001 MAIK "Nauka/Interperiodica"

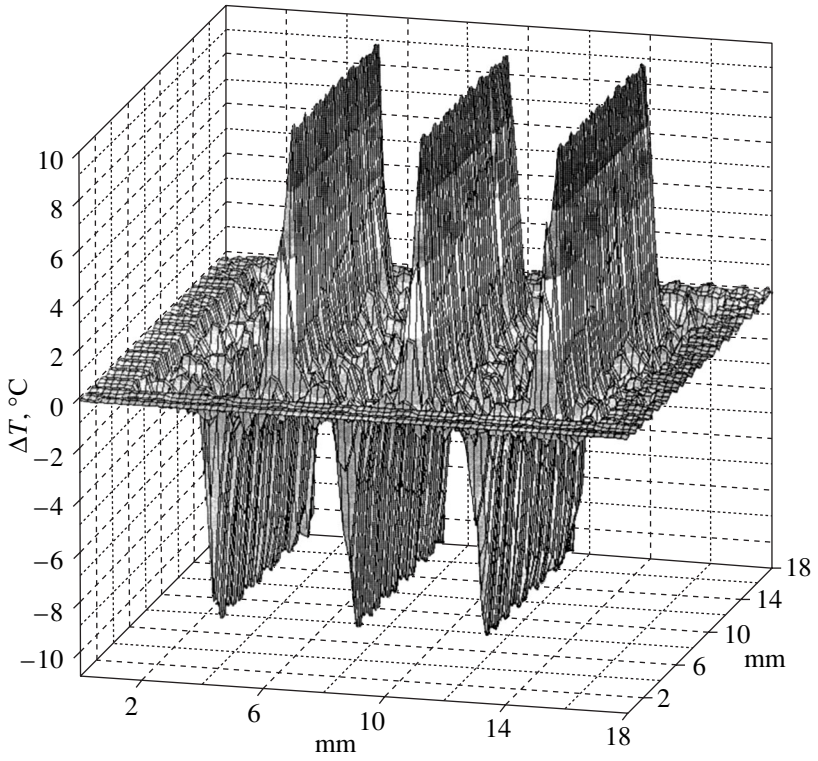

Fig. 2. A typical three-dimensional pattern of the emission power distribution for three pairs of the array elements (every third element is connected) switched in an alternating (positive and negative) luminescence regime (E = 5 V/cm, H = 3.5 kG).

three-dimensional pattern. The image was obtained by subtracting a shot of the disabled array (corresponding to the $T_{\text{eff}}(0)$ value) from a shot of the array at the instant of luminescence excitation ($T_{\text{eff}}(j)$ value). A zero level corresponded to the background emission intensity, relative to which the effective temperature was determined: $\Delta T = T_{\text{eff}}(j) - T_{\text{eff}}(0)$.

In order to reduce the Joule heat evolved in the IR source, the array was powered by a pulsed current source, which provided an energy supply during a single shot (τ = 40 ms). The synchronized shot record start was ensured by a lock-in system. The luminescence sign was determined by the current direction in the element. In order to obtain an IR emission pattern with alternating contrast, the supply voltage was applied in alternating polarity so that the current directions were opposite in each pair of adjacent elements (see the inset in Fig. 1). Since the magnetoconcentration effect in the electric and magnetic field configuration employed is odd with respect to the $\mathbf{E} \times \mathbf{H}$ vector product, the IR array elements exhibited alternating positive and negative luminescence. The pattern contrast changed to opposite with every switch of the magnetic field direction.

Figure 1 shows the field dependence of the effective temperature in the array scene studied for the positive and negative luminescence excitation. The positive luminescence, representing an excess radiation from the semiconductor relative to the thermal emission level, was detected as an increase in the effective temperature of the emitting elements ($\Delta T > 0$, curve *1*), while the negative luminescence was manifested by a decrease in the effective temperature ($\Delta T < 0$, curve *2*). For an applied electric field strength of 13 V/cm and a magnetic induction of 3.5 kG, a decrease in the effective temperature of elements operating in the negative luminescence regime was about 20°C.[1] This result clearly demonstrates the possibilities of using the negative luminescence phenomenon for suppressing the thermal radiation of solids under isothermal conditions. This effect can be used for evaluating the efficiency of semiconductor devices such as thermal screens suppressing background radiation in photodetector systems and radiation coolers [6, 7].

Figure 2 shows a typical three-dimensional pattern of the emission power distribution for three pairs of the array elements switched in the alternating (positive and negative) luminescence regime. As is seen, this device can simulate an alternating IR contrast relative to a background level, showing the hot and cold areas of a model scene.

The spectra of room-temperature positive and negative luminescence, determined by the interband transitions, extend in InSb up to λ = 7 μm. The operation

[1] Recently, Adaraliev *et al.* [5] reported on reaching ΔT = –6°C in reverse-biased InAsSbP/InAs diode structures operating in the same spectral region (λ = 4 μm).

speed is determined by the nonequilibrium carrier lifetime in the system studied ($\tau \geq 2 \times 10^{-8}$ s). Note the relatively large total area of the emitter surface and the high homogeneity of the emission intensity distribution over the individual element surface. On the other hand, a minimal size of the elements in the array is limited only by the diffusion length of nonequilibrium charge carriers (in the narrow-bandgap semiconductors, this value is on the order of a few microns). The absence of *p*–*n* junctions allows the IR arrays to be based on the narrow-bandgap semiconductors such as $Cd_xHg_{1-x}Te$, which would extend the wavelength range up to 12 μm.

Devices of the type described above can be used, for example, as IR test patterns with controlled contrast for calibrating optoelectronic devices with respect to spatial, temperature, and time resolution and for creating model dynamic scenes in the IR spectral range.

Acknowledgments. This study was supported by the Ukrainian Scientific-Technological Center, project no. 394.

REFERENCES

1. N. N. Vaserin, N. K. Daderko, and G. A. Prokof'ev, *Application of Semiconductor Displays* (Énergoatomizdat, Moscow, 1991).
2. D. B. Beasley, J. B. Cooper, and D. A. Saylor, Proc. SPIE **3084**, 91 (1997).
3. H. Welker, Z. Naturforsch. A **6**, 184 (1951).
4. S. S. Bolgov, V. K. Malyutenko, and V. I. Pipa, Pis'ma Zh. Tekh. Fiz. **5** (23), 1444 (1979) [Sov. Tech. Phys. Lett. **5**, 610 (1979)].
5. M. Adaraliev, N. V. Zotova, S. A. Karandashev, *et al.*, Proc. SPIE **4355**, 161 (2000).
6. P. Berdahl, in *Proceedings of the 18th International Conference on Physics of Semiconductors, Stockholm, 1986*, pp. 1595–1598.
7. A. I. Liptuga, V. K. Malyutenko, V. I. Pipa, *et al.*, Fiz. Tekh. Poluprovodn. (St. Petersburg) **31** (4), 498 (1997) [Semiconductors **31**, 423 (1997)].

Translated by P. Pozdeev

Technical Physics Letters, Vol. 27, No. 8, 2001, pp. 647–648. Translated from Pis'ma v Zhurnal Tekhnicheskoĭ Fiziki, Vol. 27, No. 15, 2001, pp. 57–61.

Reversible Recording of Interference Gratings with a Diffraction Efficiency above 50% in an Amorphous Hydrogenized Silicon–Nematic Liquid Crystal Structure

N. L. Ivanova, A. P. Onokhov, and A. N. Chaĭka

Vavilov Optical Institute, State Scientific Center of the Russian Federation, St. Petersburg, 190164 Russia

Received March 5, 2001

Abstract—The properties of a space-time light modulator comprising an a-Si:H based *p–i–n* diode and a nematic liquid crystal layer were studied using a holographic technique. Under certain conditions, an asymmetry of the diffraction efficiency in the +1 and –1 diffraction orders was observed. The maximum diffraction efficiency in one of these orders may reach up to 52%, which is a record value for devices of this type. © *2001 MAIK "Nauka/Interperiodica".*

Optically addressable space-time light modulators (OASTLMs) of the photoconductor–liquid crystal type are widely used in the optical signal processing systems [1], in particular, for the real-time construction of holographic gratings [2]. Since the thickness of an LC layer modulating the light beam usually does not exceed 5–10 μm, the OASTLMs form thin holograms [3]. According to theoretical estimates, the maximum value of the diffraction efficiency of thin phase gratings does not exceed 33.9% for sinusoidal and 40% for the rectangular grating profiles.

Below, we report on the possibility of a real-time construction of interference gratings in OASTLMs with a diffraction efficiency significantly exceeding the indicated theoretical limits.

The OASTLM in this study possesses a sandwich structure comprising a *p–i–n* diode based on amorphous hydrogenized silicon (a-Si:H) with a thickness of 1.2 μm and nematic liquid crystal (NLC) layer with a thickness of 5 μm confined between two glass plates with transparent electrodes. A nearly planar NLC orientation (*S*-effect) was provided by obliquely deposited films of cerium dioxide. The OASTLM structure was powered by unipolar rectangular voltage pulses, so that the *p–i–n* diode operated in a reverse-biased regime.

The gratings were recorded by a modulated beam of a He–Ne laser ($\lambda = 0.633$ μm) synchronized with the control voltage pulses. The synchronization was ensured by an electrically controlled light modulator with a ferroelectric LC [4]. The pulsed pattern of interference between two plane wave fronts of equal intensity was projected onto the photoconductor. This resulted in a spatial modulation of the photoconductivity leading, in turn, to the spatial modulation of the electric field in the NLC with the corresponding NLC director reorientation. As a result, a birefringent phase grating is formed, the diffraction properties of which depend on the writing beam intensity and the control voltage. The maximum phase change for the given NLC (NIOPIK, 1282) with a layer thickness of 5 μm and $\Delta n = 0.164$ was 2.6π.

The readout was performed in a transmission mode with the aid of a linearly polarized light ($\lambda = 0.814$ μm) at an angle of 18° relative to the normal to the OASTLM entrance window. The diffraction efficiency of the grating was determined as $\eta_i = I_i^R/I_0$, where I_i^R is the light beam intensity in the *i*th diffraction order and I_0 is the intensity of light transmitted through the modulator in the absence of the writing beam. The light beam intensities were measured with the aid of a photoelectron multiplier.

An analysis of the characteristics of diffraction gratings constructed in the OASTLM under the conditions described above showed that an asymmetry in the intensities of +1 and –1 diffraction beams appears when the grating vector was parallel to the NLC director and the readout beam polarization direction and the writing beam intensity exceeded 5 μW/cm^2. If the writing pulse frequency was below 10 Hz, the gratings with a spatial frequency of $\nu = 20$ mm^{-1} had a diffraction efficiency in one of the orders considerably exceeding the theoretical limit for a thin phase grating with a sinusoidal profile.

Plots of the diffraction efficiency in the +1 and –1 orders versus the signal beam intensity for a grating with $\nu = 20$ mm^{-1} constructed in the NLC layer are presented in the figure. The measurements were performed in an interferometer arm using the power supply voltage pulses with an amplitude of $U = 32.5$ V, a duration of $\tau = 200$ ms, and a repetition period of $T = 600$ ms. As can be seen from this figure, the asymmetry in the diffraction efficiency in the +1 and –1 diffraction orders appears when the writing beam intensity in the interferometer arm ($I^{1W} = I^{2W}$) exceeds 5 μW/cm^2. The asymmetry determined as $K = \eta_{+1}/\eta_{-1}$ increases with the

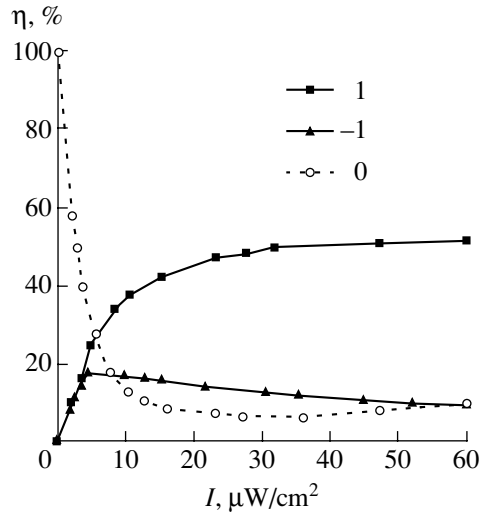

Plots of the diffraction efficiency in the 0th, +1, and –1 orders versus writing signal intensity for the interference grating with $\nu = 20$ mm^{-1} (OASTLM operated at $U = 32.5$ V, $\tau = 200$ ms, $T = 600$ ms).

writing beam intensity and reaches a maximum value of 5.5 for the signal intensity of 60 μW/cm^2. Simultaneously, the beam intensity in the zero diffraction order drops 10.5 times. At the expense of the light intensity redistribution between the zero, +1 and –1 diffraction orders, the diffraction efficiency in the +1 diffraction order reaches a maximum level of 52%. The phenomenon of asymmetry between the diffraction orders was also observed for gratings written with a continuous radiation and those having higher spatial frequencies (up to 85 mm^{-1}, which is the limit for our measuring system). We have intentionally used the low spatial frequency of $\nu = 20$ mm^{-1} in order to realize a limiting model of plane hologram, thus excluding factors such as the modulated layer thickness.

The appearance of asymmetry in the first diffraction orders and an increase in the diffraction efficiency up to 52% in one of these orders can be explained by assuming that a grating with asymmetric phase profile is formed in the NLC layer for the writing conditions employed and an OASTLM of the *p*–*i*–*n* a-Si:H–NLC type in the selected control regime. This assumption is confirmed by the fact that the asymmetry in the diffraction efficiency depends on the angle of the reading beam incidence onto the OASTLM entrance window.

Mukohraka *et al.* [5] used a holographic technique to study the characteristics of a refection OASTLM of the *i*–a-Si:H-NLC type and showed that the process of grating formation exhibited a nonlinear character leading to distortions of the sinusoidal phase profile, although the profile symmetry was retained. He *et al.* [6] also reported that diffraction of a linearly polarized light on a binary phase grating was characterized by equal light intensities in the +1 and –1 beams, while the polarization directions in these diffraction orders were asymmetric. However, more recent publications confirmed the asymmetry in the diffraction efficiency in the first order for the diffraction of a linearly polarized light in electrically-addressed matrix (640 × 480 pixels) LC modulator [7] and for the diffraction on electrically addressed binary phase grating with a planar-oriented NLC [8]. In the latter case, it was demonstrated that the +1 and –1 diffraction beam intensities were equal when the writing beam polarization was parallel to the NLC director and the grating vector was perpendicular to the director (oriented layer rubbed along the electrodes). If the writing beam polarization direction, NLC director, and the grating vector were parallel (oriented layer rubbed perpendicularly to the electrodes), the system exhibited asymmetry in the +1 and –1 beam intensities. In this configuration, the slope of NLC molecules significantly affects the character of their interaction with an inhomogeneous electric field at the electrode edges, which leads to differential reorientation of the director at the opposite electrode ends and, hence, gives rise to an asymmetry in the phase profile. The effect depends both on the NLC slope and on the ratio of the grating pitch (electrode width) to the NLC layer thickness.

In our experimental arrangement with a planar orientation of NLC molecules by obliquely deposited cerium dioxide films, the NLC molecules are sloped at 4°–6° and a mutual orientation of the director, grating vector, and polarization direction is analogous to that described in [8]. Therefore, the reason for the asymmetry in the phase profile of the grating constructed in the NLC layer may be analogous to that encountered in [8].

In concluding, it should be pointed out that the effect of asymmetry in the first diffraction order for the interference gratings constructed in OASTLMs is reported for the first time and the diffraction efficiency of $\eta = 52\%$ is a record value for devices of this type.

REFERENCES

1. A. A. Vasil'ev *et al.*, *Spatial Light Modulators*, Ed. by I. N. Kompanets (Radio i Svyaz', Moscow, 1987).
2. S. Fukushima and T. Kurokawa, Appl. Phys. Lett. **58** (8), 787 (1991).
3. T. K. Gaylord and M. G. Moharan, Appl. Opt. **20**, 3271 (1981).
4. A. N. Chaĭka, N. L. Ivanova, and A. P. Onokhov, Pis'ma Zh. Tekh. Fiz. **3** (8), 20 (1997) [Tech. Phys. Lett. **23**, 303 (1997)].
5. N. Mukohraka, N. Yohida, H. Toyoda, *et al.*, Appl. Opt. **33** (14), 2804 (1994).
6. Z. He, T. Nose, and S. Sato, Mol. Cryst. Liq. Cryst. **301**, 295 (1997).
7. J. A. Davis, P. Tsai, D. M. Cottrell, *et al.*, Opt. Eng. **38** (6), 1051 (1999).
8. M. Bouvier and T. Scharf, Opt. Eng. **39** (8), 2129 (2000).

Translated by P. Pozdeev

Technical Physics Letters, Vol. 27, No. 8, 2001, pp. 649–651. Translated from Pis'ma v Zhurnal Tekhnicheskoĭ Fiziki, Vol. 27, No. 15, 2001, pp. 62–66.

Negative Ion Emission Accompanying the Field Electron Emission from Amorphous Hydrogenated Carbon

D. P. Bernatskiĭ, A. V. Chernyshev, V. I. Ivanov-Omskiĭ, V. G. Pavlov, and T. K. Zvonareva

Ioffe Physicotechnical Institute, Russian Academy of Sciences, St. Petersburg, 194021 Russia
*e-mail: bernatskii@ms.ioffe.rssi.ru; *tag@pop.ioffe.rssi.ru*
Received February 15, 2001

Abstract—It was found that the field electron emission from the surface of amorphous hydrogenated carbon is accompanied by the emission of negative ions of hydrogen and hydrocarbons. This ion emission is explained by the formation and degradation of the local surface emission centers. © *2001 MAIK "Nauka/Interperiodica".*

Investigation of the phenomenon of field-induced electron emission from the flat surface of carbon-based materials such as the films of diamond, carbon nanotubes, and amorphous carbon is important from the standpoint of both practical applications (e.g., with a view to the creation of planar emission displays) and fundamental knowledge. However, despite the increasing number of the publications devoted to the field electron emission from carbon-based materials, processes determining the properties of such emitters are still not clearly understood [1]. This circumstance hinders formulating the requirements to potential materials most suited to the use in particular electron devices. In this context, a detailed study of the field electron emission from flat cathodes based on amorphous carbon is an important task promising useful results.

We have studied the process of electron emission from the surface of flat cathodes based on the films of amorphous carbon. The study deals with the initial portion of the current–voltage (*I–U*) characteristic measured in the small current regime, which corresponds to the initial emission stage. For this purpose, we have developed a special method providing for the simultaneous measurement of the emission current in the chain and the visual observation of the distribution of emission centers over the flat emitter surface.

The main parts of the experimental high-vacuum setup (Fig. 1) are the flat emitter *1*, grid *2*, two microchannel plates *3*, and a fluorescent screen *4*. The emitter surface images formed on the screen were registered with a photo or video camera. The emission current, collected from the whole screen or a particular region selected with the aid of a diaphragm, was measured using a replaceable photoelectron multiplier *5*. A set of two microchannel plates (in a chevron assembly) had a gain of up to 10^7, which provided for a system sensitivity sufficiently high to detect individual charged particles (electrons and ions).

The experimental procedure also allowed the time of the charged particle transit from cathode to microchannel plate to be measured, thus determining the mass composition of the emitted particles. For this purpose, a voltage pulse V_p with a duration of 10 ns and an amplitude of 1–2 kV was applied to the emitter electrode *1* via capacitor *C*. Simultaneously, a synchronizing (lock-in) pulse coinciding with the V_p pulse switched on the sweep of a storage oscillograph regis-

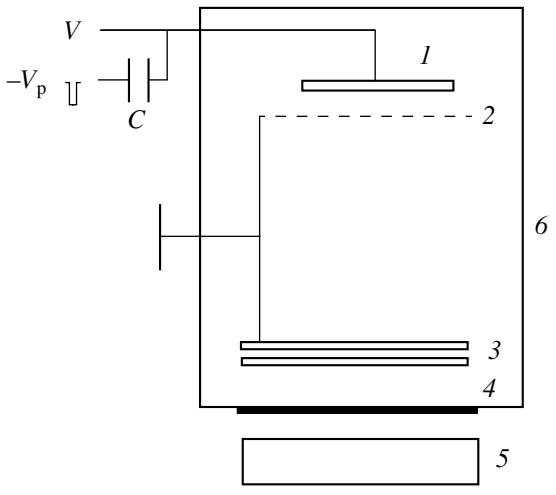

Fig. 1. A schematic diagram of the experimental setup: (*1*) sample emitter (8 × 8 mm); (*2*) grid; (*3*) microchannel plates (diameter, 56 mm); (*4*) luminescent screen; (*5*) photoelectron multiplier; (*6*) vacuum chamber.

1063-7850/01/2708-0649$21.00 © 2001 MAIK "Nauka/Interperiodica"

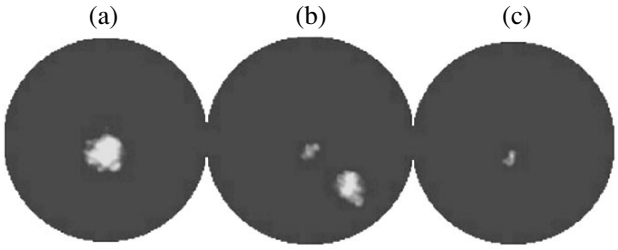

Fig. 2. Typical images showing the emission current distribution observed (a) without and (b, c) with applied transverse magnetic field.

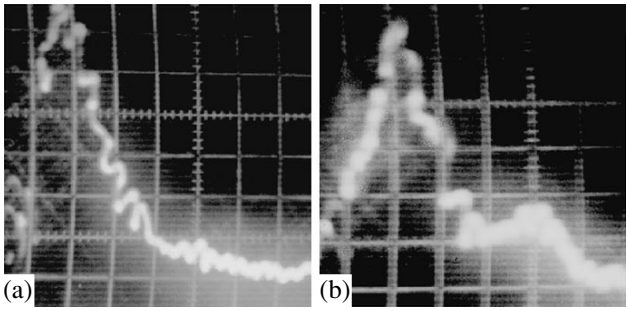

Fig. 3. Typical oscillograms of the emission current (sweep scale, 20 ns/div) containing (a) only the electron component and (b) the electron component and negative ions (H^-) with an arrival time delayed by 6×10^{-8} s relative to electrons.

tering the output pulse from the photoelectron multiplier. The oscillograms obtained in this lock-in mode allowed a time delay to be measured between the V_p pulse front and the emission pulses due to charged particles of various masses arriving at the detector.

The measurements were performed for amorphous hydrogenated carbon (a-C:H) films with a thickness of 500–700 Å obtained by dc reactive magnetron sputtering of a graphite target [2]. The a-C:H layers were deposited onto heavily doped silicon wafers of the KES-0.01 grade, with a Ni film deposited onto the rear side of the substrate. By varying the deposition conditions, it was possible to modify the deposit characteristics such as the hydrogen content, hybridization of bonds, layer thickness, etc.

The pattern of electron emission observed on the luminescent screen *4* had the form of bright spots (Fig. 2a). A lower threshold of the electric field strength at which the emission spots could be observed was 1.5×10^4 V/cm. This threshold was dependent of several factors, mainly the allotropic and chemical composition of the amorphous carbon films. The spatial arrangement, intensity, and size of the bright spots changed in response to variation of the electric field. The *I–U* characteristics of the emission plotted in the Fowler–Nordheim coordinates exhibited deviations from the linearity. When the field strength increased up to 10^5 V/cm and above, some of the samples exhibited an avalanche growth in the emission current, after which new local emission centers formed on the emitter surface.

It was established that the emission current contains several components. The main fraction of particles represented electrons emitted in a strong electric field. A magnetic field applied in the transverse direction readily deflected the electron flow (Fig. 2b); under certain conditions, the electron beam could be driven off the screen area and the emission current detector input so that the electron component was subtracted from the total signal observed on the screen and the current measured in the detector circuit (Fig. 2c).

However, the screen still displayed some bright spots virtually unchanged upon application of the transverse magnetic field. This fact indicated that the plane-parallel detector system continued detecting charged particles, the motion of which was almost not affected by the magnetic field. From this, we may infer that negatively charged ions contribute to the total current. The ion current density increased with the electric field strength. It should be noted that the ion component was detected at a higher field strength (6×10^4 V/cm) as compared to the electron emission threshold.

The experiments with a pulsed electric field allowed us to determine the mass spectrum of the charge carriers contributing to the total emission current. The emission current oscillograms exhibited a pronounced structure (Fig. 3). An analysis of these oscillograms [3] showed, in addition to the electron component, the presence of negative hydrogen ions (H^- and H_2^-) and heavier ions with masses in the 10–20 amu interval (probably, C^- and CH_n^-). The presence of the ion component in the total emission current is indicative of a complicated character of processes occurring on the surface and in the subsurface layer of a-C:H films in the course of the emission center formation and the current collection. The negative ions of carbon and hydrocarbons were repeatedly observed and reported previously (see, e.g., [4]). The mechanism of the negative ion formation in the system studied is not quite clear, but it is probable that the ion emission is related to processes involved in the formation and degradation of the electron emission centers.

A thorough investigation of the effect of negative ion emission accompanying the field electron emission will help elucidating the mechanisms of activation and operation of flat emission cathodes based on amorphous carbon. This will lead to improvements in the carbon cathode technology and expansion of the application field.

Acknowledgments. This study was supported by the Russian Foundation for Basic Research (project no. 00-02-17004) and the Federal Program "Surface Atomic Structures" (project no. 3.14.99).

REFERENCES

1. J. Robertson, in *Proceedings of the XI International Vacuum Microelectronics Conference, IVMC'98, Asheville, 1998*, p. 162.
2. V. L. Aver'yanov, T. K. Zvonareva, A. V. Chernyshev, *et al.*, Fiz. Tverd. Tela (Leningrad) **33** (11), 3410 (1991) [Sov. Phys. Solid State **33**, 1923 (1991)].
3. D. P. Bernatskiĭ, Yu. A. Vlasov, and V. G. Pavlov, Pis'ma Zh. Tekh. Fiz. **12** (13), 806 (1986) [Sov. Tech. Phys. Lett. **12**, 333 (1986)].
4. É. Ya. Zandberg and V. I. Paleev, Zh. Tekh. Fiz. **42** (4), 851 (1972) [Sov. Phys. Tech. Phys. **17**, 671 (1972)].

Translated by P. Pozdeev

Technical Physics Letters, Vol. 27, No. 8, 2001, pp. 652–655. Translated from Pis'ma v Zhurnal Tekhnicheskoĭ Fiziki, Vol. 27, No. 15, 2001, pp. 67–76.

The Effect of Electron Detachment on the Diffusive Decay of a Low-Pressure Electronegative Plasma

E. A. Bogdanov[a], A. A. Kudryavtsev[a]*, and L. D. Tsendin[b]

[a] *St. Petersburg State University, St. Petersburg, Russia*

[b] *St. Petersburg State Technical University, St. Petersburg, Russia*

** e-mail: akud@ak2138.spb.edu*

Received January 30, 2001

Abstract—There are two possible scenarios in the diffusion decay of a low-pressure electronegative plasma in a system featuring the electron detachment effect. In the case of a weak detachment, the system exhibits an initial sharp drop in the electron concentration followed by the ion–ion plasma formation. A small admixture of electrons appearing as a result of the detachment keeps all negative ions within the volume. In this stage, the densities of all charged plasma components decay according to the same exponential law with a characteristic detachment time. In the limit of a strong detachment, a principally different plasma decay regime takes place. In this limiting case, a usual (free of negative ions) rather than ion–ion plasma is formed in the second stage. This can be accompanied by paradoxical phenomena such as the growth of electron density with time, build-up of the near-wall potential jump, and a considerable decrease (up to complete vanishing) of the diffusion electron cooling usually dominating in the electron gas energy balance. © *2001 MAIK "Nauka/Interperiodica".*

The evolution of inhomogeneities in the electron and ion density distribution in a multicomponent plasma is described by nonlinear equations [1, 2]. For this reason, the space-time characteristics of the diffusion decay of a plasma containing negative ions differ significantly from those of a usual plasma free of such ions. At low pressures, when all plasmachemical reactions in the plasma volume can be ignored, a principal feature of this process is the presence of two decay stages [3–5]. In the first stage, negative ions are closed (confined) in the volume where their average concentration remains unchanged: $\bar{n}_n(t) = \text{const}$. Since $\bar{n}_p = \bar{n}_n + \bar{n}_e > \bar{n}_e$, the condition of equality for the fluxes of electrons and positive ions to the walls requires a greater relative rate of loss for electrons. As a result, the $\bar{n}_p/\bar{n}_e$ ratio sharply increases that reflects self-acceleration of the electron loss process. The first stage ends with the formation of an ion–ion (electron-free) plasma [3–5].

The plasma decay scenario can be strongly influenced by plasmachemical reactions. In the presence of attachment at a frequency ν_a, the decay is qualitatively identical to the purely diffusion process [3–5], although the duration of the first stage (in which electrons are lost) may decrease to $t_0 \approx 1/\nu_a$ [5]. The effect of detachment (treated below in more detail) dramatically changes the situation [9]. If this effect is sufficiently pronounced, the first stage (with a duration characterized by the detachment time $t_d \approx 1/\nu_d$, where ν_d is the detachment frequency) ends with the transition from the initial strongly electronegative plasma [with $\bar{n}_p(0) \sim \bar{n}_n(0) > \bar{n}_e(0)$] to a usual electron–ion plasma with a small admixture of negative ions ($\bar{n}_p \sim \bar{n}_e \gg \bar{n}_n$). As a result, the second stage ($t > t_d$) is virtually the same as that in the case of a usual ambipolar electron–ion diffusion. This can be accompanied by paradoxical phenomena such as the growth of electron density with time [6], build-up of the near-wall potential jump, and the diffusion electron cooling vanishing [7, 8].

By analogy with [4, 5], the afterglow in a flat geometry ($|x| < L$) is described by a system of equations

$$\partial n_p/\partial t + \partial \Gamma_p/\partial x = 0, \quad (1)$$

$$\partial n_n/\partial t + \partial \Gamma_n/\partial x = -\nu_d n_n, \quad (2)$$

$$\partial n_e/\partial t + \partial \Gamma_e/\partial x = \nu_d n_n, \quad (3)$$

where $\Gamma_j = D_j(\partial n_j/\partial x) \pm b_j n_j E$ are the component fluxes; D and b are the corresponding diffusion coefficients and mobilities; and the subscripts $j = e, n, p$ refer to electrons, negative ions, and positive ions, respectively. The system (1)–(3) is supplemented with the zero boundary conditions for the particle concentrations on the walls and their gradients at the center. The initial conditions are represented (as in [4, 5]) by a parabolic ion profile $n_n(x, 0)$ and a flat electron profile $n_e(x, 0)$ for $x < x_0$. In the external region $x > x_0$ (where electrons are absent), the corresponding profiles are $n_p(x, 0) \sim n_e(x, 0) \sim \sin[\sqrt{z + a}\,(L - x)]$, where z and α are the ionization and attachment frequencies (in units of the characteristic diffusion time of negative ions $\tau_n = L^2/D_n$) [1, 2].

Considered jointly with the electroneutrality condition

$$n_e + n_n = n_p, \quad \Gamma_e + \Gamma_n = \Gamma_p, \tag{4}$$

the above equations determine the concentrations of charged particles and the field strength. The D and b coefficients are determined by thermal electrons; for simplicity, these electrons are assumed to be distributed by the Maxwell law. Therefore, the system (1)–(4) should be supplemented with an equation for the electron temperature T_e. Due to the high thermal conductivity, this temperature can be considered as constant in the cross section [2]. The cross-section-averaged energy balance equation for thermal electrons is as follows:

$$(3/2)\bar{n}_e dT_e/dt = -3\delta_\varepsilon \nu_\varepsilon \bar{n}_e (T_e - T)/2 - H_{dc} + H_{dt}. \tag{5}$$

Here, terms in the right-hand part (5) describe the plasma cooling due to collisions with neutrals in the volume (ν_ε and δ_ε being the corresponding frequency and energy exchange factor, respectively), the diffusion cooling (H_{dc}), and the possible heating by fast electrons (H_{dt}).

Within the framework of the hydrodynamic model (5), the process of fast electron production and loss as a result of detachment and superelastic collisions, as well as due to collisions involving high energy losses, may lead to large errors and, generally speaking, requires a kinetic analysis [2, 8]. For example, the detachment reactions $O^- + O \longrightarrow O_2 + e$ and $O^- + O_2(a) \longrightarrow O_3 + e$ (leading to the formation of O_2 and O_3 molecules in the ground state) are accompanied by the appearance of fast electrons with the energies (ε_d = 3.6 and 0.6 eV, respectively) markedly exceeding the gas temperature T. If these reactions lead to the formation of vibrationally excited molecules, the energies ε_d of detached electrons will be much lower. In practice, the cases with both large and small ε_d values may take place.

The situation is also affected by the value of $e\varphi_w$, a self-consistent wall potential relative to the center, which is determined using the condition of equal fluxes for the particles of opposite signs (see Eq. (4)). For $\varepsilon_d < e\varphi_w$ and the electron energy distributed by the Maxwell law, the $e\varphi_w$ value is on the order of a few T_e ($e\varphi_w = C_1 T_e$, $C_1 \approx \ln(\sqrt{M/m})$ [2]) and $H_{dc} = e\varphi_w \Gamma_e(L, t)$. Here, the detached electrons are confined in the volume and transfer an energy of $\varepsilon_{d1} \approx \nu_e \varepsilon_d/(\nu_e + \delta_\varepsilon \nu_\varepsilon)$ to the thermal electrons (ν_e is the frequency of electron–electron collisions) [7, 8]. In this case, the heating of thermal electrons due to detachment can be approximately taken into account by introducing an additional source term $H_{dt} = \varepsilon_{d1} K_d \bar{n}_n$ into the right-hand part of Eq. (5).

At higher energies of the detached electrons ($\varepsilon_d > C_1 T_e$), there are two principally different possible situations in which the H_{dc} and H_{dt} values must be determined in a self-consistent manner. As long as the integral flux of detached fast electrons is smaller than the ambipolar flux of positive ions ($L\nu_d \bar{n}_n < \Gamma_p(L, t)$), the fast electrons are lost on the walls by free diffusion ($\Gamma_{ed}(L, t) = L\nu_d \bar{n}_n$) and can be considered independently of the slow plasma electrons. In this case, a fast electron with the energy ε_d gives to the plasma electrons only a small part of this energy $\varepsilon_{d2} \approx \varepsilon_d \nu_e/(\nu_e + \delta_\varepsilon \nu_\varepsilon + 1/\tau_{df}) \approx \varepsilon_d \nu_e \tau_{df} \ll \varepsilon_d$ (where $\tau_{df} \approx 4L^2/(\pi^2 D_e)$) is a characteristic time of the free electron diffusion); as a result, the additional heating of thermal electrons $H_{dt} = \varepsilon_{d2} \nu_d \bar{n}_n$ is still small [7, 8]. The wall potential increases to $e\varphi_w = C_1 T_e - T_e \ln[1 - L\nu_d \bar{n}_n/\Gamma_p(L, t)]$, while the diffusion cooling $H_{dc} = -e\varphi_w[\Gamma_p(L, t) - L\nu_d \bar{n}_n]$ decreases as compared to that calculated in the absence of fast electrons. Since the plasma electron heating in the above cases is small, the T_e value rapidly drops down to the gas temperature when the discharge is switched off.

A principally different situation takes place when the decrease in T_e is accompanied by a drop of the flux $\Gamma_p(L, t)$ down to a level below $L\nu_d \bar{n}_n$. In order to "close" the excess part $L\nu_d \bar{n}_n - \Gamma_p(L, t)$ of the detached fast electrons in the volume, the wall potential approaches the electron energy ($\varepsilon_d \approx e\varphi_w$) and the diffusion cooling of thermal (confined) electrons is absent ($H_{dc} = 0$). The confined fast electrons, in contrast to the transit ones, heat the plasma more effectively by transferring the energy $\varepsilon_{d1}(\varepsilon_{d1} \gg \varepsilon_{d2})$. The corresponding heating term in Eq. (5) is $H_{dt1} = \varepsilon_{d1}[L\nu_d \bar{n}_n - \Gamma_p(L, t)]$. Another part of the fast electron flux, equal to $\Gamma_p(L, t)$ and lost on the wall with the energy $\approx \varepsilon_d$, produces relatively small heating of the thermal electrons: $H_{dt2} = \varepsilon_{d2} \Gamma_p(L, t)$ (for more details, see [7, 8]). In this case, we may expect that, as long as $\nu_d \bar{n}_n > \delta_\varepsilon \nu_\varepsilon \bar{n}_e$, the electron temperature will retain a sufficiently high quasi-stationary level

$$T_{es} = T + 2\varepsilon_{d1} \nu_d \bar{n}_n / 3\delta_\varepsilon \nu_\varepsilon \bar{n}_e \tag{6}$$

rather than rapidly drop down to room temperature.

Thus, provided that the rate of fast electron production $\nu_d \bar{n}_n$ is small (or these electrons are detached with a small energy ε_d) from the very beginning, the T_e value rapidly drops down to the gas temperature T (or even below this level if the diffusion cooling effect is taken into account). If the number of fast detached electrons is large, T_e drops down to $\sim T$ only when the detachment rate decreases to $\nu_d \bar{n}_n < \delta_\varepsilon \nu_\varepsilon \bar{n}_e$ and the Maxwellian electrons are no longer heated.

Depending on the ratio between the characteristic times ν_d^{-1}, $(\delta_\varepsilon \nu_\varepsilon)^{-1}$, and $\tau_{ap} = 4L^2/(\pi^2 D_p(k + 1))$ (the latter is a characteristic time of the ambipolar electron–ion diffusion, $k = T_e/T$), we may distinguish between the two main scenarios of the plasma decay in a system featuring the electron detachment effect. In all cases, the negative ions are confined in the volume and their aver-

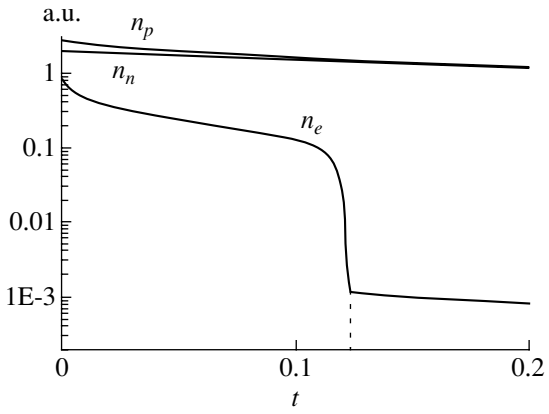

Fig. 1. Variation of the $\bar{n}_e(t)$, $\bar{n}_n(t)$, and $\bar{n}_p(t)$ densities in the regime of self-confinement of negative ions. Here and below ($b_e/b_n = 1\sqrt{2}$, $b_e/b_n = 250$).

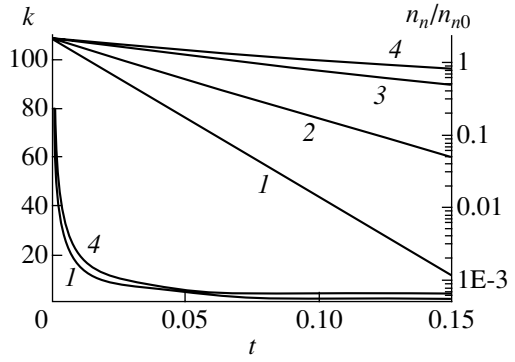

Fig. 2. The plots of $k(t) = T_e(t)/T$ and $\bar{n}_n(t)/\bar{n}_n(0)$ calculated for $\varepsilon_d = \varepsilon_{d2} = 2T$ and various ν_d: (*1*) 7; (*2*) 10; (*3*) 25; (*4*) 50.

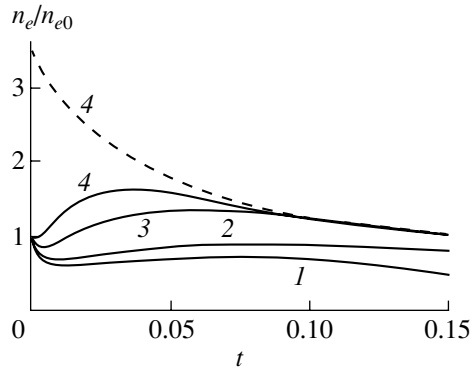

Fig. 3. The plots of $\bar{n}_e(t)/\bar{n}_e(0)$ calculated for $\varepsilon_d = \varepsilon_{d2} = 2T$ and various ν_d (solid curves): (*1*) 7; (*2*) 10; (*3*) 25; (*4*) 50. Dashed curve show the $\bar{n}_p(t)/\bar{n}_e(0)$ curve for $\nu_d = 50$.

age density decays with a characteristic detachment time $t_d = 1/\nu_d$ by the law

$$\bar{n}_n(t) = \bar{n}_n(0)\exp(-\nu_d t). \qquad (7)$$

In the case of weak detachment ($\nu_d \bar{n}_n(0) \ll \bar{n}_e(0)/\tau_{ap}$), the pattern is analogous to that for the first stage of decay in the absence of plasmachemical processes, which was considered in [3–5] (Fig. 1). Here and below, all plots are constructed on the scale of dimensionless coordinate (expressed in units of L) versus dimensionless time (in units of $\tau_n = L^2/D_n$). Owing to a fast diffusion cooling, the $T_e(t)$ value rapidly drops and the subsequent plasma decay proceeds in two stages. First, electrons rapidly leave the volume according to the model [3–5] (dashed curve in Fig. 1). A small admixture of detached electrons keeps all negative ions within the volume. For this reason, the ion–ion plasma decay in the second stage is not controlled by the ambipolar ion–ion diffusion (cf. [3–5]). The densities of all charged plasma components decay according to the same exponential law $\bar{n}_e(t) \sim \bar{n}_n(t) \sim \bar{n}_p(t) \sim \exp(-\nu_d t)$ analogous to that described by Eq. (7).

In our opinion, this phenomenon, whereby negative ions are confined in the second (ion–ion) decay stage by the electrons appearing (together with the negative ions) in the course of detachment, should be called the "self-confinement" of negative ions (cf. [9]). In order to provide for this regime, it is necessary, on the one hand, that a sharp initial drop in the electron density take place leading to the formation of an ion–ion plasma with a low electron content ($\bar{n}_p(t_0) \approx \bar{n}_n(t_0) \gg \bar{n}_e(t_0)$) and, on the other hand, that even a small admixture of detached electrons "close" all negative ions in the volume. A criterion of the transition to the self-confinement of negative ions and the reversal of their flux from outward (onto wall) to inward (into plasma) is $\Gamma_p(L, t_1) = L\nu_d \bar{n}_n(t_1)$, rather than the condition $\nu_d \tau_n = 2$ proposed in [9].

In the limiting case of strong detachment ($\nu_d \bar{n}_n \geq \bar{n}_e/\tau_{ap}$), a principally different plasma decay regime takes place. In this regime, a usual plasma (free of negative ions) rather than ion–ion plasma is formed in the second stage. Since $T_e(t)$ strongly depends on the energy ε_d of detached electrons, let us consider two cases: $\varepsilon_d = 20T$ and $2T$. In both cases, the first (detachment) stage ($t < t_d$) involves a monotonic decrease in the ion concentrations $\bar{n}_p(t)$ and $\bar{n}_n(t)$ due to diffusion and detachment processes, respectively. However, relaxation of the electron density and temperature proceeds differently, depending on the ε_d and $e\varphi_w$ values. Figures 2–5 show the results of model calculations for various values of the detachment frequency ν_d.

In the case of a small energy of detached electrons ($\varepsilon_d = \varepsilon_{d2} = 2T$), the heating of Maxwellian electrons is small and the electron temperature $T_e(t)$ rapidly decreases as a result of the diffusion cooling (Fig. 2). Here, all the $T_e(t)$ curves calculated for various ν_d almost coincide with each other and, according to Eq. (5), their initial portions ($t < t_1$) obey the law $T_e(t) \sim$

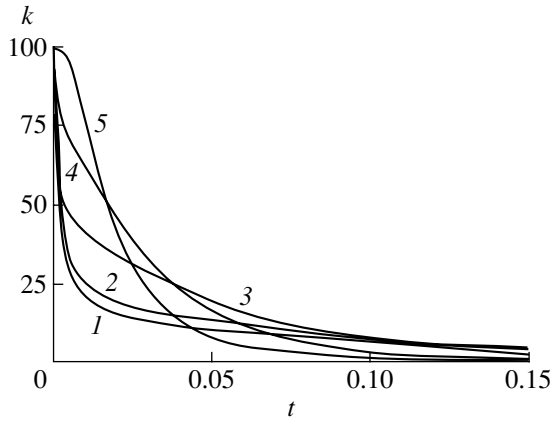

Fig. 4. The plots of $k(t) = T_e(t)/T$ calculated for $\varepsilon_d = \varepsilon_{d1} = 20T$ and various ν_d: (*1*) 7; (*2*) 10; (*3*) 25; (*4*) 50; (*5*) 100.

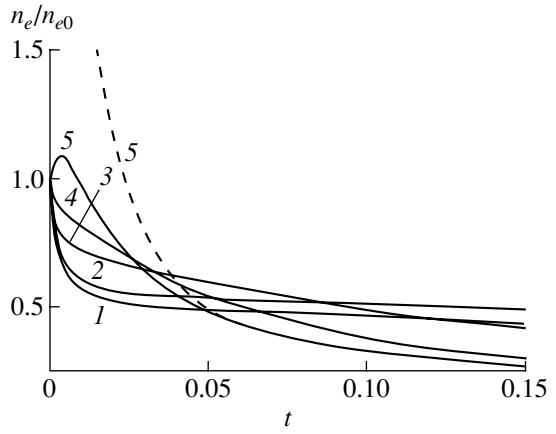

Fig. 5. The plots of $\bar{n}_e(t)/\bar{n}_e(0)$ calculated for $\varepsilon_d = \varepsilon_{d1} = 20T$ and various ν_d (solid curves): (*1*) 7; (*2*) 10; (*3*) 25; (*4*) 50; (*5*) 100. Dashed curve show the $\bar{n}_p(t)/\bar{n}_e(0)$ plot for $\nu_d = 100$.

$n_e(t)^{C_1/2}$. Due to the drop of $T_e(t)$, the flux of positive ions to the wall decreases. When this flux drops to a level of $\Gamma_p(L, t_1) \approx L\nu_d\bar{n}_n(t_1)$, the electron density begins to grow (Fig. 3). The higher the detachment frequency, the earlier the onset of the electron density growth. For a sufficiently large ν_d, this growth may begin immediately after the discharge switch-off (Fig. 3, curve *4*). The negative ions disappear during the characteristic detachment time ($t_d = 1/\nu_d$), after which the decay of the usual electron plasma with $\bar{n}_p \sim \bar{n}_e \gg \bar{n}_n$ in the second stage is determined by a usual ambipolar electron–ion diffusion.

In the case of a high energy of detached electrons ($\varepsilon_d = \varepsilon_{d1} = 20T$), only the $T_e(t)$ curves with small ν_d frequencies decay as rapidly as those with small ε_d values (cf. Figs. 2 and 4). For $\varepsilon_d > C_1T_e$, the detached fast electrons are lost on the walls by free diffusion, which accounts for an $L\nu_d\bar{n}_n$ part of the total flux of electrons to the walls. As noted above, the flux of Maxwellian plasma electrons accounts for only the remaining $(\Gamma_p(L, t) - L\nu_d\bar{n}_n)$ smaller part. Accordingly, the efficiency of the diffusion cooling also significantly decreases ($H_{dc} = -e\varphi_w[\Gamma_p(L, t) - L\nu_d\bar{n}_n]$). Since the diffusion cooling at low pressures is the main factor of the electron gas cooling [2], the $T_e(t)$ decay rate significantly decreases. The system features a certain kind of feedback between the rates of decrease in the electron temperature and density: a decrease in the $T_e(t)$ drop rate caused by the lower diffusion cooling, whereby T_e approaches a quasi-stationary value (6), hinders attaining the condition $\Gamma_p(L, t_1) \approx L\nu_d\bar{n}_n(t_1)$ at which the $n_e(t)$ begins to grow. Note that this situation may lead to the development of instability and the oscillatory decay regime in which oscillations of the near-wall potential jump $e\varphi_n(t)$ are significant [8].

Thus, in a system featuring the formation of fast electrons as a result of detachment, a close relationship between the electron gas density and energy leads to a monotonic decrease in the plasma electron concentration (Fig. 5). Only in the case of a strong detachment, when the initial densities satisfy the condition $\nu_d\bar{n}_n(0) \geq \bar{n}_e(0)/\tau_{ap}$, does the electron density $n_e(t)$ exhibit a growth in the initial short time interval $t_d \sim 1/\nu_d$ (Fig. 5, curve *5*).

REFERENCES

1. L. D. Tsendin, Zh. Tekh. Fiz. **55** (12), 2318 (1985) [Sov. Phys. Tech. Phys. **30**, 1377 (1985)]; Zh. Tekh. Fiz. **59** (1), 21 (1989) [Sov. Phys. Tech. Phys. **34**, 11 (1989)].
2. A. V. Rozhansky and L. D. Tsendin, *Transport Processes in Partially Ionized Plasmas* (Énergoatomizdat, Moscow, 1988; Gordon and Breach, 2001).
3. S. A. Gutsev, A. A. Kudryavtsev, and V. A. Romanenko, Zh. Tekh. Fiz. **65** (11), 77 (1995) [Tech. Phys. **40**, 1131 (1995)].
4. E. A. Bogdanov, A. A. Kudryavtsev, and L. D. Tsendin, Zh. Tekh. Fiz. **71** (4), 40 (2001) [Tech. Phys. **46**, 404 (2001)].
5. E. A. Bogdanov, A. A. Kudryavtsev, and L. D. Tsendin, Pis'ma Zh. Tekh. Fiz. **27** (9), 47 (2001) [Tech. Phys. Lett. **27**, 373 (2001)].
6. A. A. Kudryavtsev, A. L. Kuranov, V. G. Mishakov, *et al.*, Zh. Tekh. Fiz. **71** (3), 29 (2001) [Tech. Phys. **46**, 299 (2001)].
7. N. B. Kolokolov, A. A. Kudryavtsev, and O. G. Toronov, Zh. Tekh. Fiz. **55** (10), 1920 (1985) [Sov. Phys. Tech. Phys. **30**, 1128 (1985)].
8. A. B. Blagoev, N. B. Kolokolov, and A. A. Kudrjavtsev, Phys. Scr. **50**, 371 (1994).
9. I. D. Kaganovich, B. N. Ramaputhri, and D. J. Economou, Appl. Phys. Lett. **76** (20), 2844 (2000).

Translated by P. Pozdeev

Technical Physics Letters, Vol. 27, No. 8, 2001, pp. 656–658. Translated from Pis'ma v Zhurnal Tekhnicheskoĭ Fiziki, Vol. 27, No. 15, 2001, pp. 77–83.

The Kinetics of a Diamond-Like Film Growth in a Microwave Gas Discharge Plasma

S. Yu. Suzdal'tsev and R. K. Yafarov

Saratov Department, Institute of Radio Engineering and Electronics, Russian Academy of Sciences, Saratov, Russia

Received February 28, 2001

Abstract—Spontaneous variations of the microstructure and properties of carbon films during deposition in a microwave gas discharge plasma were studied. The ion current component of the gas discharge plasma favors the selective growth of a diamond-like phase with a thickness exceeding that achieved in the case of a pyrolytic deposition process. *© 2001 MAIK "Nauka/Interperiodica".*

Investigation of the conditions and mechanisms of the synthesis of nano- and microcrystalline carbon film materials representing various allotropes (in particular, diamond-like) at low pressures and temperatures is of considerable value for both applications and fundamental science. This is related to a large variety of the phase microstructure organization types, shapes, and dimensions of carbon nanoclusters in these films. These characteristics, depending on the conditions of material synthesis, account for the unique quantum-dimensional and other properties of the films.

The purpose of our experiments was to study the film deposition kinetics and to search for technological conditions favoring the growth of diamond-like nano- and microcrystalline materials with controlled surface microtopography.

The films were deposited in an ethanol vapor plasma in the gas discharge excited by a microwave generator operating in a regime of electron cyclotron resonance. The samples were prepared on glass substrates using an experimental setup described previously [1]. The temperature in a stationary deposition regime was measured with an accuracy of ±5°C using a calibrated thermoresistor fastened to the substrate holder. The deposited film thickness was determined with the aid of an ellipsometric laser microscope. Detailed investigation of the film surface microtopography was performed with a scanning atomic-force microscope of the NT-MDT type. The film structure was studied by X-ray diffraction on a DRON-3.0 diffractometer.

Figure 1 shows experimental plots of the refractive index, film thickness, and the microcrystallite (grain) surface density and size versus deposition time for the carbon films grown from plasma at an ethanol vapor pressure of 5 Pa. The substrate holder temperature was 300°C and the microwave power supplied to the discharge was about 250 W.

According to the experimental data obtained (Fig. 1), the films grown in the interval of deposition times from 5 to 20 min are characterized by a virtually linearly increasing thickness and an almost linear correlated increase in both parameters (grain size and surface density) characterizing the surface microtopography. A further increase in the process duration leads to a pronounced decrease in the density of grains observed on the growth surface. This circumstance, despite continuing increase in the linear grain size, results in that the rate of increase in the film thickness drops to almost zero in the deposition time interval between 20 and 40 min. This is accompanied by accelerated growth of the refractive index. The extremal character of the grain density variation with time and the related changes in the growth rate and optical properties of the film is evidence that the structure and properties of diamond-like films qualitatively change in the curse of the growth process. Another feature to be noted in Fig. 1 is a rather large thickness of diamond-like films deposited from plasma in comparison to the analogous films obtained by pyrolytic methods.

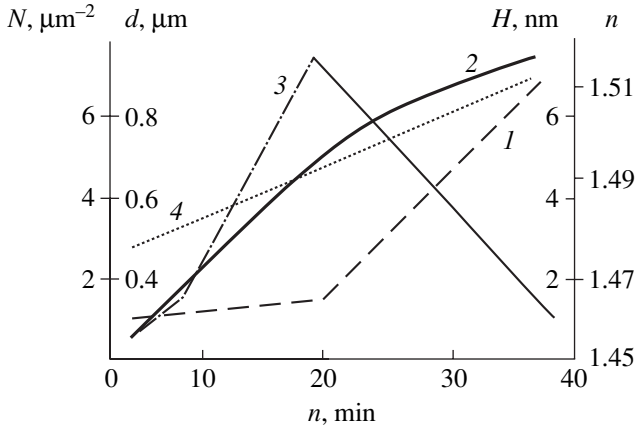

Fig. 1. Experimental plots of the (*1*) refractive index *n*, (*2*) film thickness *d*, (*3*) surface density of grains *N*, and (*4*) grain size *H* versus deposition time for the carbon films grown from a microwave gas discharge plasma.

1063-7850/01/2708-0656$21.00 © 2001 MAIK "Nauka/Interperiodica"

As is known, a decrease in the growth rate of a diamond-like film, as well as the drop in the density of grains on the film surface (explained by a decrease in the nucleation rate), is related to the effect of spontaneous passivation caused by a non-diamond carbon structure formation on the growth surface. The film growth ceases upon the formation of a continuous graphite monolayer representing a stable low-pressure phase possessing kinetic advantages under the deposition conditions.

The most important difference of the pyrolytic diamond film growth from the process of deposition in a microwave gas discharge is the ion-chemical action upon the growth surface in the latter case. This factor may provide for a selective growth of a diamond-like phase and eliminate advantages of the graphite phase growth.

Owing to heterodesmicity, the probability that a graphite nucleus would hold on the surface in the early nucleation and grain growth stages must decrease with increasing temperature. This hypothesis was confirmed by our experimental data, according to which an increase in the substrate temperature under otherwise equal process conditions did not lead to a decrease in the growth rate of diamond-like films in the microwave gas discharge plasma (the film growth rate either increased or remained unchanged). Proceeding from the heterodesmicity of graphite, we may also suggest that selectivity of the diamond-like film deposition in the plasma must depend on the ion type and the total ion current to the substrate, but not on the ion energy.

Figure 2 present the experimental plots illustrating dependence of the current density, film thickness, and the grain size and surface density on the magnitude and sign of accelerating potential applied to the substrate holder. It was established that a negative bias on the substrate holder favored deposition of a "light" diamond-like films with a transmission coefficient close to 100%. An analysis of the X-ray diffraction patterns of these films, as well as those characterized in Fig. 1, showed that the negatively-biased films are composed predominantly of the diamond-like phases of carbon with a hexagonal lattice belonging to three structural modifications (lonsdaleite, C(20H), etc.), include a (111)-oriented cubic diamond phase, and contain small inclusions of a fine-crystalline graphite phase (002). These films exhibited a low electric conductivity (resistivity up to 10^7 Ω m).

An X-ray diffraction study of the films deposited with a positive potential applied to the substrate holder showed that these samples contained predominantly a fine-crystalline graphite phase with a interplanar distance of $d = 3.36$ Å [2]. These films were characterized by a transmission coefficient varying from 60 to 75% (an increase in the positive potential value led to a decrease in the film transmission). The resistivity of such films did not exceed several dozen Ω m.

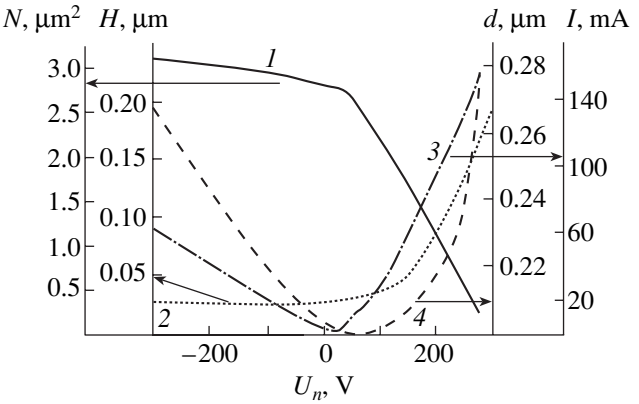

Fig. 2. Plots of the (*1*) grain size, (*2*) surface density of grains, (*3*) current density, and (*4*) film thickness versus the accelerating potential applied to the substrate holder.

An analysis of the experimental data indicates that most significant qualitative changes in the microstructure, growth rate, and microtopography of carbon films were observed, under otherwise equal conditions, upon changing the sign of a bias potential applied to the substrate holder. Note that the character of variation of some characteristics in Fig. 2 even changed to opposite. The size of micro- and nanosized grains in the carbon films grown on the negatively biased substrates is virtually independent of the voltage in the range from –300 to 0 V. At the same time, the action of positive hydrogen ions (the main plasma component in the case of film deposition from ethanol vapors) favorably influences the diamond-like film growth: the higher the positive (hydrogen) ion current density, the greater the nucleation rate, the surface density of grains, and the diamond-like film growth rate.

On the contrary, bombardment of the positively-biased films with electrons and negative ions (of oxygen, carbon, and OH groups) led to the predominant growth of graphite films. Here, the film growth rate and the graphite grain size increased with the positive potential and with the ion current to the substrate, while the nucleation rate and the surface density of grains exhibited a decrease. It was also established that a decrease in the ethanol vapor pressure below a certain level (0.1 Pa), rendering the microwave plasma rarefied and highly ionized, resulted in the growth of graphite films irrespective of the applied potential size and magnitude.

Thus, the obtained experimental data showed that the applied electric field stimulates the grain growth during a carbon film deposition from an ionized gas phase. This effect is related to the intensification of the mass transfer and the activation of processes on the growth surface [3]. The electric field separates ions (positive or negative, depending on the sign of potential applied to the substrate holder) produced by dissociation and ionization of ethanol molecules and transported to the substrate. The presence of ionized carbon

and the deficit of positive hydrogen ions (in the case of a positively biased substrate) favor the growth of a carbon phase. The electric field produces the polarization of molecules in the gas phase and in a chemisorbed layer. This stimulates the process of mass transfer both from the gas phase to the growing crystal face and over the grain surface. Deformation of the adsorbed neutral and negatively charged carbon-containing complexes in the electric field may change their decay activation energy, thus intensifying the process of growth on a preset crystallographic face. Therefore, the absence of a strong oversaturation and a high surface mobility of carbon atoms stimulated by a change in the energy relief of a surface bombarded by plasma ions (rather than by a general increase in the substrate temperature) favor the formation of a dense and mobile adsorbed carbon layer necessary for realization of the lateral growth mechanism leading to the growth of graphite-like films.

The diamond-like phase, in contrast to the graphite-like one, may grow via both lateral and normal mechanism. Therefore, the diamond structure would predominantly form under the conditions favoring the normal growth. For this purpose, the substrate temperature should be decreased, while the degree of oversaturation must be increased. The latter circumstance explains the fact that no diamond-like film growth was observed in a microwave plasma at very low vapor pressures, irrespective of the potential applied to the substrate. In the presence of oversaturation, which is a necessary but not sufficient condition for the diamond-like film growth, a decisive factor of the growth control is the current density of separated ions supplied from the gas phase to the substrate. Predominant growth of the diamond-like microcrystals at a negative potential applied to the substrate is due to the two mechanisms. The first is the ion-chemical sputtering (by hydrogen ions) of the graphite phase nuclei in the absence of interaction between the growing diamond-like phase and negative oxygen ions. The second is the low-energy lattice activation (by the same ions) of chemisorption and crystallization processes in the excited carbon clusters of a certain type, leading to the diamond-like crystal structure growth.

Therefore, a decrease in the diamond-like film growth rate in a stationary deposition regime in a microwave gas discharge plasma is related to a decrease in the nucleation rate, while the existing nuclei continue to grow in size. An increase in the growth rate and maximum thickness observed for the films grown in the microwave gas discharge plasma as compared to the pyrolytic deposition is mostly due to the factors selectively affecting processes on the growth surface in the former case, suppressing the diamond film passivation by a graphite deposit. Other distinctive features of the growth of diamond-like films are the relatively lower energy consumption as compared to the graphite film growth and, probably, the radical growth mechanism of the diamond-like phase nucleation at high oversaturations.

REFERENCES

1. N. N. Bylinkina, S. P. Mushtakova, V. A. Oleĭnik, *et al.*, Pis'ma Zh. Tekh. Fiz. **22** (6), 43 (1996) [Tech. Phys. Lett. **22**, 245 (1996)].
2. A. Ubbelohde and F. Lewis, *Graphite and Its Crystalline Compounds* (Clarendon Press, Oxford, 1960; Mir, Moscow, 1965).
3. Yu. M. Tairov and V. F. Tsvetkov, *Technology of Semiconductor and Dielectric Materials* (Vysshaya Shkola, Moscow, 1990).

Translated by P. Pozdeev

Technical Physics Letters, Vol. 27, No. 8, 2001, pp. 659–661. Translated from Pis'ma v Zhurnal Tekhnicheskoĭ Fiziki, Vol. 27, No. 15, 2001, pp. 84–89.

Electron Transport in the Granular Amorphous Carbon Films with Cobalt Nanoparticles

L. V. Lutsev[a]*, T. K. Zvonareva[b], and V. M. Lebedev[c]*****

[a] *DOMEN Research Institute, St. Petersburg, Russia*
** e-mail: info@domen.ru*
[b] *Ioffe Physicotechnical Institute, Russian Academy of Sciences, St. Petersburg, 194021 Russia*
*** e-mail: siklitsky@pop.ioffe.rssi.ru*
[c] *St. Petersburg Institute of Nuclear Physics, Russian Academy of Sciences, Gatchina, Leningrad oblast, Russia*
**** e-mail: lebedev@mail.pnpi.spb.ru*

Received February 15, 2001

Abstract—The temperature dependence of electric conductivity was studied in a granular amorphous carbon containing cobalt nanoparticles at an overall cobalt concentration below the percolation threshold. It was established that the electron transport in this structure is determined by the inelastic resonance electron tunneling via localized states, which are situated in the dielectric carbon matrix between isolated conducting metal clusters. The number of the localized states is determined as a function of the cobalt concentration in the composite. © *2001 MAIK "Nauka/Interperiodica"*.

Granular structures comprising low-dimension ferromagnetic particles (grains) dispersed in an insulating matrix exhibit optical, electrical, and magnetic properties significantly differing from those of the analogous bulk crystalline and amorphous materials. These distinctions in the properties of granular materials, manifested below the percolation threshold, are controlled to a considerable extent by the features of electron tunneling between metal grains, that is, by the potential barrier height and the characteristics of localized states in the matrix.

The purpose of this study was to determine the number of localized states involved in the tunneling process at the Fermi level of an amorphous hydrogenated carbon matrix containing various amounts of cobalt in the form of nanoparticles.

The number of localized states was determined within the framework of a theoretical model relating the phonon-induced inelastic resonance electron tunneling (through a chain of localized states in the amorphous layer between the tunnel contacts) to the temperature dependence of the conductivity $\sigma(T)$ [1, 2]. Since the number of atoms in the metal grains is sufficiently large ($N \gg 1$, typically $N \sim 1000$), this model can be used to study the character of electron transport between particles in the granular structures. The presence of localized states in such systems leads to a considerable increase in transparency of the tunneling barrier, which significantly affects the temperature and field dependence of the charge transfer process. The number of localized states in the matrix is an important characteristic for some other processes as well. In particular, the localized states determine the character of magnetoresistance and certain features of the frequency spectrum of the conductivity.

According to the model adopted [1, 2], a special place in the conductivity mechanism belongs to the process of the inelastic resonance electron tunneling through the channels containing localized electron states possessing energies scattered within an interval on the order of the thermal energy kT. The temperature dependence of the conductivity in such a channel containing n impurity centers obeys the power law

$$\bar{\sigma}_n = P\left(\frac{\Lambda^2}{\rho c^5}\right)^{(n-1)/(n+1)} \frac{(ga^2n^2l)^n T^\gamma E^\alpha}{al} \times \exp\left[\frac{-2l}{a(n+1)}\right], \quad (1)$$

where a is the radius of the localized state, l is the average distance between grains, $\gamma = n - 2/(n + 1)$, $\alpha = 2n(n + 1)$, P is the proportionality coefficient, Λ is the deformation potential constant, ρ is the matrix substance density, c is the velocity of sound in the matrix, g is the density of localized states, and E is the localized state energy ("depth") in the barrier region.

The inelastic resonance electron tunneling via single-impurity channels ($n = 1$) leads to a weak variation of the conductivity $\sigma(T)$ with the temperature. An increase in the distance between granules leads to a growth in the number of channels and in the number of impurities in each channel. As $n \longrightarrow \infty$, the total conductivity via all channels exhibits the transition from

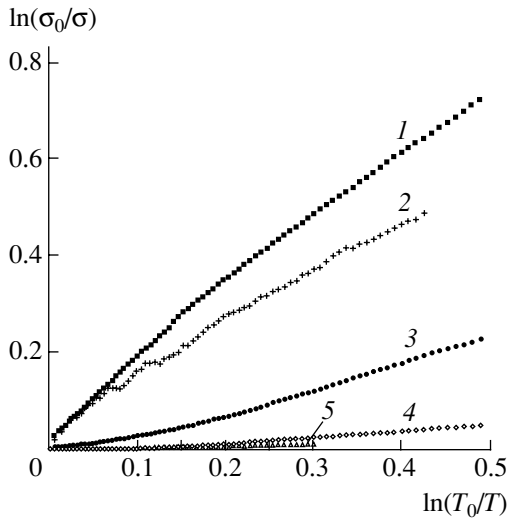

Fig. 1. Logarithmic plots of relative conductivity versus reciprocal temperature for a-C:H(Co) films with various cobalt concentrations (at. fraction) x = 0.24 (*1*), 0.30 (*2*), 0.35 (*3*), 0.44 (*4*), and 0.46 (*5*).

resonance tunneling to hopping conductivity as determined by the Mott law [3, 4]:

$$\ln\sigma(T) \propto -\left(\frac{T_c}{T}\right)^{1/4},$$

where $T_c = \beta/ga^3$ and β is a numerical parameter.

Below the percolation threshold, the conductivity σ of a granular structure is determined by the size of isolated conducting clusters composed of metal particles and by the set of channel conductivities (1) between clusters. The dimensions of conducting clusters depend on the degree of structural disordering and are determined by the localization of electron wavefunctions at the Fermi level of metal particles. Since the cluster conductivity is significantly higher than the tunneling conductivity (1) via impurity channels, the total conductivity $\sigma(T)$ of a granular structure is described by a power function of the temperature and determined by the average number $\langle n\rangle$ of localized states in the conducting channels.

Experimental investigations aimed at determining the number of localized states from data on the temperature dependence of conductivity were performed on the samples of amorphous hydrogenated carbon containing cobalt nanoparticles, designated by a-C:H(Co). The a-C:H(Co) films were grown on polycor (nanophase corundum-based ceramic) substrates by dc magnetron sputtering of composite graphite and cobalt targets in an argon–hydrogen plasma (80% Ar + 20% H_2). The concentration of cobalt in the amorphous carbon deposit was controlled by changing the ratio of cobalt and graphite target areas. The films were deposited onto substrates heated to 200°C. Prior to the deposition process, the chamber was evacuated to a base pressure of 1 μTorr. The samples were prepared in a working gas flowing at a pressure of 10 mTorr and an ion current density of 10^{-1} A/cm^2. The a-C:H(Co) film growth rate depended on the amount of cobalt introduced into the composition and varied in our experiments between 1.4 and 3.0 nm/min. Ohmic contacts in the form of 0.5-mm-wide 15-mm-long copper microstrips were preliminarily deposited onto the substrate surface in vacuum. The microstrips had a thickness of 250–550 nm and were spaced by 3.5 mm.

The film composition was determined by nuclear-physical methods of elemental analysis employing charged particle beams. The cobalt to carbon atomic ratio was determined by Rutherford backscattering using protons with a primary energy of E_p = 1 MeV. In addition to the main controlled components, the films contained oxygen and nitrogen impurities. The impurity concentrations were determined by the method of nuclear reactions with deuterons at E_d = 1 MeV: $^{16}O(d, p)^{17}O$; $^{14}N(d, p)^{15}N$; $^{12}C(d, p)^{13}C$. This technique is described in more detail elsewhere [5]. Based on these data, we determined the ratio x of the number of cobalt atoms to the total number of atoms determined by methods of elemental analysis. For the samples studied, the relative content of cobalt atoms x varied from 0.24 to 0.46, which corresponded to a cluster structure below the percolation threshold. The size of cobalt particles, determined from the small-angle X-ray scattering (SAXS) measurements, increased with x: from 2.3 nm at x = 0.24 to 3 nm at x = 0.46.

The temperature dependence of conductivity was measured in a sample cooling mode for a current passing in the film plane (horizontal geometry) at an applied voltage of 0.1 V. Figure 1 shows the plots of relative conductivity versus temperature in the logarithmic coordinates. The initial point corresponds to the conductivity σ_0 measured at T_0 = 299.5 K. As can be seen from these data, the conductivity is described in the first approximation by a power function of the temperature. This behavior is evidence that the contribution of inelastic resonance tunneling to conductivity is described by the model adopted [1, 2]. Insignificant deviations of the experimental curves from the power relationships are probably explained by the temperature-induced rearrangement of the isolated conducting clusters involved in the electron tunneling. A similar fine structure in the temperature dependence of conductivity was observed in a-C:U(Cu) granular films [6].

Figures 2a and 2b show the plots of conductivity σ and the average number $\langle n\rangle$ of localized states in the tunneling channels between isolated conducting clusters as functions of the cobalt concentration. The number $\langle n\rangle$ of localized states was calculated using a relationship given by formula (1):

$$\langle n\rangle = \frac{1}{2}[\gamma - 1 + (\gamma^2 + 2\gamma + 9)^{1/2}],$$

where the power index γ was determined from the experimental temperature variation of the conductivity.

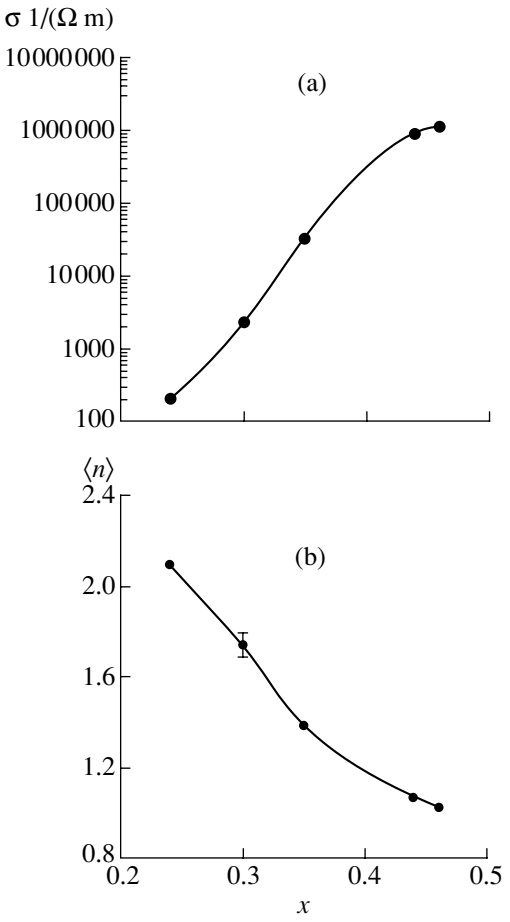

Fig. 2. Plots of (a) conductivity σ and (b) average number ⟨*n*⟩ of localized states in the tunneling channels between isolated clusters versus relative cobalt content *x* in a-C:H(Co) films.

Thus, using a comparison of the experimental data with predictions based on the theoretical model [1, 2], we may conclude that the electron transport in the granular structures with a cobalt concentration below the percolation threshold is controlled by the inelastic resonance tunneling via a relatively small number of localized sates situated between the conducting metal clusters.

Acknowledgments. The authors are grateful to M.V. Baĭdakova for conducting the SAXS measurements, to V. I. Siklitsky for processing the X-ray diffraction data, and to V. I. Ivanov-Omskiĭ for fruitful discussions and valuable remarks.

This study was supported by the Russian Foundation for Basic Research (RFBR), project no. 99-02-16071a; one of the authors (T.K.Z.) received also an RFBR grant no. 00-02-17004.

REFERENCES

1. L. I. Glazman and R. I. Shekhter, Zh. Éksp. Teor. Fiz. **94** (1), 292 (1988) [Sov. Phys. JETP **67**, 163 (1988)].
2. L. I. Glazman and K. A. Matveev, Zh. Éksp. Teor. Fiz. **94** (6), 332 (1988) [Sov. Phys. JETP **67**, 1276 (1988)].
3. B. I. Shklovskiĭ and A. L. Efros, *Electronic Properties of Doped Semiconductors* (Nauka, Moscow, 1979; Springer-Verlag, New York, 1984).
4. H. Böttger and V. V. Bryksin, *Hopping Conduction is Solids* (Akademie-Verlag, Berlin, 1985), p. 398.
5. T. K. Zvonareva, V. M. Lebedev, T. A. Polyanskaya, *et al.*, Fiz. Tekh. Poluprovodn. (St. Petersburg) **34** (9), 1135 (2000) [Semiconductors **34**, 1094 (2000)].
6. L. V. Lutsev, S. V. Yakovlev, and V. I. Siklitskiĭ, Fiz. Tverd. Tela (St. Petersburg) **42** (6), 1105 (2000) [Semiconductors **42**, 1139 (2000)].

Translated by P. Pozdeev

Technical Physics Letters, Vol. 27, No. 8, 2001, pp. 662–664. Translated from Pis'ma v Zhurnal Tekhnicheskoĭ Fiziki, Vol. 27, No. 15, 2001, pp. 90–94.

A Gas-Dispersed Medium for Pulsed Chemical Lasers Based on Photon-Branched Chain Reactions

V. I. Igoshin, V. S. Kazakevich, A. Yu. Kurov, A. L. Petrov, and V. D. Shlyak

Lebedev Institute of Physics (Samara Branch), Russian Academy of Sciences, Samara, Russia

e-mail: laser@fian.smr.ru

Received March 11, 2001

Abstract—A gas-dispersed medium (aluminum particles in argon) was obtained for the first time with the parameters necessary for the development of pulsed chemical lasers based on photon-branched chain reactions: particle size, 0.1–0.15 μm; particle density, $>10^8$ cm^{-3}; argon pressure, 0.3–1.5 atm; medium lifetime, >10 min.

Previously [1], we have theoretically demonstrated the possibility of creating a purely chemical pulsed H_2–F_2 laser based on a photon-branched chain reaction (PBCR), with finely dispersed passivated aluminum particles in the active medium. Under the action of the IR laser radiation, the metal particles evaporate and the atomic aluminum interacts with F_2 molecules with the formation of fluorine atoms F playing the role of active centers:

$$Al + F_2 \longrightarrow AlF + F.$$

This is the onset of a chain reaction leading to the reagent burning with the formation of excited hydrogen fluoride molecules:

$$F + H_2 \longrightarrow HF^* + H,$$

$$H + F_2 \longrightarrow HF^* + F.$$

A fraction of the laser radiation photons participates in the particle heating, thus facilitating the active center nucleation. If the yield of photons exceeds their consumption for the initiation and continuation of the reaction, the entire process becomes self-sustained. Reactions of this type can be considered as processes with the photon branching mechanism, which can serve as a base for creating powerful laser systems.

When the experimental work on the creation of lasers of this type was just started, there were misgivings that dark reactions of a fraction of aluminum particles with an $H_2(D_2)$–F_2 mixture may lead to a decrease in the energy stored by the chemically active medium and to spontaneous burning of the medium. However, shortly after the possibility of creating gas-dispersed active media with a pressure of ~1 atm for the pulsed chemical H_2–F_2 and D_2–F_2 lasers was experimentally proved [2]. It was demonstrated for the first time that adding Al particles (by spraying a commercial Al powder synthesized by the levitation technique) with a size of ~0.5 μm and a concentration of ~10^5 cm^{-3} to an $H_2(D_2)$–F_2–O_2–He mixture (50 : 114 : 11 : 635) at a pressure of P = 1 atm does not increase the rate of the dark production of HF molecules; the gas mixtures with aluminum particles exhibited a long-term stability (~15 min). The heating and evaporation of Al particles in the D_2–F_2 laser medium under the action of radiation of an H_2–F_2 laser generator led to burning of the former laser medium within a time period of ~3 μs. The absence of amplification and generation in the experiments reported in [2] was explained by insufficient concentration of Al particles, low degree of homogeneity in the aluminum distribution over the medium volume, and the presence of coarse (d > 1 μm) fragments appearing as a result of coagulation.

It was concluded [2] that necessary prerequisites for the creation of a chemical laser with photon-branched chain reaction in a chemically active gas-dispersed medium are as follows:

(i) homogeneity of the gas-dispersed medium;

(ii) high concentration of the dispersed phase (10^8–10^9 cm^{-3});

(iii) submicron average particle size (0.1–0.05 μm);

(iv) long gas-dispersed medium lifetime (2–15 min).

Aluminum powders obtained by the existing methods by no means always satisfy the requirements (with respect to the particle size distribution and the presence of foreign impurities) to the dispersed phase of an active medium for a PBCR-based chemical laser.

In this study, a gas-dispersed medium was obtained by passing a current pulse through an aluminum wire or foil in an argon atmosphere. In experimentally selecting an optimum regime of the gas-dispersed medium formation, we varied the duration (5–30 μs) and shape of current pulses, the aluminum conductor type (a wire with a diameter of 0.2–0.4 mm or a foil with a thickness of 10–20 μm) and length (100–200 mm), the capacitance and charging voltage of the capacitor bank, and the gas (argon) pressure. The discharge current density

1063-7850/01/2708-0662$21.00 © 2001 MAIK "Nauka/Interperiodica"

exceeded 10^6 A/cm^2 and the specific deposited energy was 0.2–1.5W_c (W_c is the sublimation energy of the exploding conductor). The gas-dispersed medium was probed with a He–Ne laser beam and the radiation attenuation and scattering levels were determined, which provided information about homogeneity of the medium and the Al particle concentration in the gas mixture.

The signals from photodetectors were digitized with the aid of an L-1250 ADC interface and transmitted to a personal computer for the processing. The particle size was evaluated by the electron diffraction microscopy of samples prepared by a 10- to 20-h deposition from aerosol onto glass substrates. The samples represented a lacy structure of fine particles forming a three-dimensional web with a height of up to 100 μm, which could be retained for months; coarse particles occurred immediately on the substrate surface. The particles were also studied by electron diffraction. An analysis of the electron diffraction patterns showed that the particles are composed predominantly of a pure aluminum; an aluminum oxide film, when present, had a thickness not exceeding 0.01 μm.

The results of investigations showed that the main technological parameters determining the characteristic size and concentration of Al particles formed upon explosion of the wire or foil are the current pulse shape, voltage across the exploding conductor, and the energy deposited.

The explosion of an Al wire involves the stage of conductivity breakage and current halt. This behavior is characteristic of the model of exploding wire [3, 4], according to which a wire conducting a pulsed current with a density of ~10^6 A/cm^2 exhibits an initial expansion (leading to the conductivity breakage and the current halt) followed by the metal dispersion in particles with a characteristic size of ~0.1 μm. These events take place for a deposited energy of ~0.5W_c over a time period of 1–5 μs, which indicates that the metal evaporation and condensation process during the aerosol formation is not a limiting stage.

The gas-dispersed media most suited for the creation of PBCR-based chemical lasers were obtained upon explosion of a wire with a diameter of 0.2 mm or a foil with a thickness of 20 μm, a width of 2 mm, and a length of 200 mm. The conductor was exploded in a horizontal quartz tube with an internal diameter of ~16 mm. For a capacitor bank charged to a voltage of 19 kV, the deposited energy was ~0.6W_c. The electron-microscopic examination of the aluminum particles in an electron microscope showed that particles formed upon the explosion of both foil and film possess a characteristic size of ~0.1 μm. Almost all the explosion regimes studied led to the formation of a certain amount of coarse particles (0.5–1 μm), but their number was insignificant as compared to the finely dispersed phase.

Data on the time variation of the attenuation coefficient of a laser radiation with λ = 0.63 μm for the optimum regimes of wire and foil explosion are presented in the figure. Taking into account that all coarse particles precipitate within 3–5 min, the concentration of a finely dispersed fraction estimated after 10 min was 10^9 cm^{-3}. The experiment showed clarification of the medium, whereby the particle concentration dropped by a factor of more than 5 over a 10-min period of time (from 10th to 20th minute). A possible reason for the suppressed coagulation process in the gas-dispersed medium studied is the argon "coat" formation on the particle surface [5]. Repeated discharge of the capacitor bank charged to 5–7 kV led (see curves *1a* and *2a* in the figure) to a complete or partial (depending on the deposited energy) restoration of the gas-dispersed medium composition in the tube.

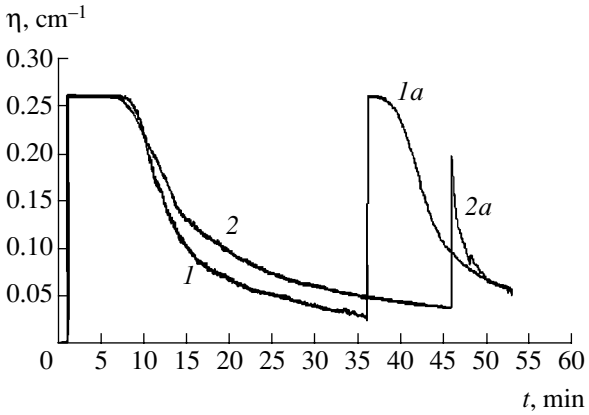

Time variation of the attenuation coefficient η of the He–Ne laser radiation transmitted through a gas-dispersed medium formed upon explosion of aluminum (*1*) foil and (*2*) wire (U = 1 kV/cm; deposited energy, ~0.6W_c).

The experiments showed that an increase in the deposited energy above W_c by increasing the bank capacitance resulted in that a considerable fraction of the stored energy was dissipated in the discharge at the instant of the conductor dispersion. This led to the particle charging and the formation of a stable "web" structure within a time period of less than one minute. A decrease in the voltage at a constant deposited energy caused an increase in the average particle size (~0.2–0.3 μm) and in the fraction of coarse (0.5–1 μm) particles. A decrease in the gas pressure down to 0.3 atm led to a faster precipitation of particles, although neither an average size nor concentration of particles were altered.

An interesting effect was observed upon the current passage through an aluminum foil in the doubly-folded regions. The foil exhibited a network of through holes with a diameter of ~50 μm and fused edges. The amount of holes on the cathode side was 2–3 times that on the anode side. The capacitor bank voltage was applied to the ends of the quartz tube containing the foil. The current density was 5×10^5 A/cm^2 or above. All experiments were performed in an argon atmosphere at a pressure of 0.25–1.5 atm. This perforation

effect was observed for the current oscillation half-period having a characteristic value of 1–5 ms. To our knowledge, this phenomenon was never reported in the literature.

Thus, the results of our experiments demonstrated the possibility of obtaining a gas-dispersed laser medium in a range of argon pressures from 0.3 to 1.5 atm, containing particles with a characteristic size of 0.1–0.15 μm and a concentration exceeding 10^8 cm^{-3}. It is suggested that the effect of argon "coat" formation significantly facilitates the development of PBCR-based chemical laser by suppressing the particle coagulation process.

REFERENCES

1. V. I. Igoshin and S. Yu. Pichugin, Kvantovaya Élektron. (Moscow) **16** (3), 437 (1989).
2. M. A. Azarov, V. A. Drozdov, V.I. Igoshin, *et al.*, Kvantovaya Élektron. (Moscow) **24** (11), 983 (1997).
3. S. V. Lebedev and A. I. Savvatimskiĭ, Usp. Fiz. Nauk **144** (2), 215 (1984) [Sov. Phys. Usp. **27**, 749 (1984)].
4. A. P. Il'in and A. A. Gromov, *Oxidation of Hyperfine Aluminium and Boron Powders* (Tomsk, 1999).
5. A. P. Il'in, Fiz. Khim. Obrab. Mater., No. 4, 93 (1997).

Translated by P. Pozdeev

Technical Physics Letters, Vol. 27, No. 8, 2001, pp. 665–668. Translated from Pis'ma v Zhurnal Tekhnicheskoĭ Fiziki, Vol. 27, No. 16, 2001, pp. 1–9.

Data Transmission through a Radio Channel Using Masking Oscillations

É. V. Kal'yanov

Fryazino Branch, Institute of Radio Engineering and Electronics, Russian Academy of Sciences, Fryazino, Moscow oblast, Russia

Received November 29, 2000

Abstract—A scheme of data transmission through a radio channel masked by chaotic oscillations is considered. A mathematical model describing the system is formulated in the case of chaotic oscillations generated in two separated frequency bands. The results of a numerical analysis of the model are presented. It is demonstrated that hidden data transmission in such a channel is possible. *© 2001 MAIK "Nauka/Interperiodica".*

Using chaotic oscillations for masking the transmitted data is a promising direction in modern communication theory, which has extensively developed in the past decade [1–8]. However, the problem of the qualitative discrimination of the informative signal from chaos requires further investigation. Below we propose a new method for the hidden data transmission using two frequency-separated bands of chaotic oscillations.

The proposed method of data transmission can be used both with two data channels and with a single communication channel. However, single-channel transmission encounters more difficulties. In this case, the proposed method is schematically illustrated in Fig. 1. The system comprises a transmitter composed of elements *1–5*, a communication channel *6*, and a receiver including elements *7– 13*.

A masking signal is produced by a source of stochastic oscillations *1* and branched in the decoupling element *2*. Some (half) of these oscillations are converted (frequency-shifted or multiplied) in device *3* and fed to the summing device *4* together with the nonconverted chaotic oscillations from decoupler *2* (the second half of the chaotic signal from generator *1*) and with the regular oscillations carrying the informative signal. The total signal appears as chaotic (noiselike) oscillations with an increased spectral power density of the chaotic oscillations in the two separated frequency bands. This signal is amplified by amplifier *5* and, after being transmitted via channel *6*, by amplifier *7* compensating for the losses and distortions in the communication channel. In other words, the signal entering decoupler *8* in the absence of informative component ($s(t) = 0$) must be equal to the chaotic signal at the input of amplifier *5*.

The chaotic oscillations received (containing the informative signal) are separated in decoupler *8*. One part of the signal received is processed by filter *9* separating the frequency band containing the informative signal. A signal from the other output of decoupler *8* is transmitted via converter *10* to filter *11* separating chaotic oscillations in the same frequency band. This processing allows the informative signal to be separated as a difference of oscillations in subtractor *12* and fed to detector *13*.

The conversion of masking oscillations in device *3* is essentially the coding of chaotic oscillations. This conversion allows the informative signal, masked by chaos, to be confidentially transmitted via channel *6* in one frequency band and the nonconverted chaotic oscillations to be transmitted in the other frequency band. The latter information is necessary for separating the useful signal from chaos upon the transformations described above of the received signal in devices *9–13*.

For masking the informative signal, it is expedient to use narrowband chaotic oscillations formed by the low-power source *1*. In this case, it is possible to restrict the conversion to a small frequency shift in converters *3* and *10*. However, the frequency shift magnitude is of no principal significance for a mathematical model illustrating the proposed masking method. At the same time,

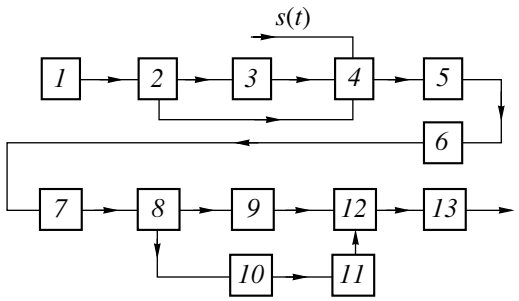

Fig. 1. Schematic diagram of the system of hidden data transmission comprising (*1–5*) transmitter elements, (*6*) transmission line (radio channel), and (*7–13*) receiver elements: (*1*) source of chaotic oscillations; (*2*, *8*) decouplers; (*3*, *10*) frequency converters; (*4*) summing device; (*5*, *7*) amplifiers; (*9*, *11*) filters; (*12*) subtractor; (*13*) detector; $s(t)$ is the informative signal.

1063-7850/01/2708-0665$21.00

a mathematical modeling of the scheme depicted in Fig. 1 is significantly simplified when the coding (frequency conversion) reduces to a multiplication process leading naturally to a greater change in the average frequency of oscillations.

Let us consider a mathematical model for the scheme depicted in Fig. 1, with the informative signal masked by chaotic oscillations shifted with the aid of frequency multipliers. Chaotic oscillations convenient for the analysis are provided by a stochastic system described in the general case by a system of nonlinear equations with delay [9]

$$\begin{aligned} \ddot{x}_1 + 2\delta\dot{x}_1 + \omega_0^2 x_1 &= -\omega_0 y_1 + \varphi(x_1, y_1), \\ \dot{y}_1 + by_1 &= ax_1 + \psi(x_1). \end{aligned} \tag{1a}$$

Here, x_1, y_1 are the variables depending on time t; δ, ω, a, and b are constants; and $\varphi(x_1, y_1)$ and $\psi(x_1)$ are nonlinear functions. The upper point indicates differentiation with respect to time t.

The properties of a generator described by Eqs. (1a) are determined by particular expressions for the nonlinear functions. For the nonlinear functions presented in the form

$$\begin{aligned} \varphi(x_1, y_1) &= -(1.5\omega_0 x_1 + 0.5x_1^2 + y_1)x_1 \\ &\quad + \sigma(\alpha - 2r + 1)(x_1 + \omega_0), \end{aligned} \tag{1b}$$

$$\psi(x_1) = (\sigma - 0.5b)x_1^2, \tag{1c}$$

and obeying the relationships

$$2\delta = \sigma - \alpha, \quad \omega_0^2 = b(r-1), \quad a = (2\sigma - b)\omega_0, \tag{1d}$$

a solution to Eqs. (1a) may correspond to a chaotic attractor.

Besides the generator described by Eqs. (1), the stochastic source *1* in Fig. 1 contains two filters connected in series. These elements are described by the equations

$$\ddot{x}_i + (\omega_i/Q_i)\dot{x}_i + \omega_i^2(x_i - \beta_i x_{i-1}) = 0, \tag{2}$$

(i = 2, 3). Here ω_i, Q_i are the intrinsic frequencies and quality factors of the filters and β_i are the coupling parameters. The output signals of decoupler *2* are determined by the quantities $\gamma x_3(t)$ and $(1 - \gamma)x_3(t)$ (where $\gamma < 1$).

The frequency converter (multiplier) *3* contains the input and output filters and a nonlinear element. The input and output filters are described Eqs. (2) with i = 4–6 and 8–10, respectively. The nonlinear element is characterized by a cubic polynomial

$$x_j = \nu x_{j-1} + \mu x_{j-1}^3, \tag{3}$$

where ν and μ are constants and j = 7.

The oscillatory process at the output of the summing device *4* is described by the expression $x_{11}(t) = x_{10}(t) + (1 - \gamma)x_3(t) + s(t)$, where $s(t)$ are regular oscillations modulated by the informative signal. These oscillations can be presented in the form $s(t) = [A_s + F(t)]\cos(\omega_s t)$, where A_s and ω_s are the carrier amplitude and frequency and $F(t)$ is the informative signal proper.

The $x_{11}(t)$ oscillations are passed through elements *5* and *6* and amplified in *7*, after which the signal $x_{12}(t)$ at one of the outputs of decoupler *8* is equal to $x_{12}(t) = \gamma x_{11}(t)$. This signal is fed to a system of serial filters *9* described by Eq. (2) with i = 13–16. A signal $x_{17}(t) = (1 - \gamma)x_{11}(t)$ from the second output of decoupler *8* enters the frequency multiplier *10* similar to converter *3*. The input and output filters of multiplier *10* are described by Eq. (2) with i = 18–20 and 22–24, respectively. The nonlinear element of multiplier *10* is characterized by Eq. (3) with j = 21. Oscillations $x_{24}(t)$ from the output of *10* enter filter *11* described by Eqs. (2) with i = 26–28,

Taken from the output of subtractor *12*, oscillations $x_{29}(t) = x_{16}(t) - x_{28}(t)$ are processed in detector *13* separating the informative signal. Detector *13* contains a nonlinear element, integrating circuit, and a low-Q filter. The nonlinear element and integrating circuit are described by the equations

$$x_k(t) = \xi_0 + \xi_1 x_{k-1}(t) + \xi_2 x_{k-1}^2(t), \tag{4}$$

$$\dot{x}_{k+1}(t) = \zeta[x_k(t) - x_{k+1}(t)], \tag{5}$$

where ξ_0, ξ_1, ξ_2, and ζ are constant coefficients and k = 30. The filter is described by Eq. (2) with i = 32. The $x_{32}(t)$ signal describes the received information.

Equations (1)–(5) describe a mathematical model of the data transmission scheme depicted in Fig. 1. The relatively large number of conjugated (serial) filters used in the model is necessary in order to ensure a numerical analysis with a sufficiently high filtration of the frequency-separated bands of the chaotic oscillations. The analysis is more conveniently performed in the case of low-Q filters. The level of filtration provided by a single low-Q second-order filter described by Eq. (2) is small even at a large detuning of the bands of transmitted frequencies. This is related to the special shape of the resonance curve of a serial resonance circuit (a small attenuation in the region of low frequencies). At the same time, using narrow oscillation bands does not provide for a clear illustration of the signal masking. The real filters used in practice ensure a significant filtration, so that effective masking of the informative signal can be ensured by a narrowband noise with a normal distribution law.

In calculating the mathematical model described by Eqs. (1)–(5), the following values of parameters determining the operating regime of the stochastic generator were used: σ = 36, α = 28, r = 7, and b = 3. The intrinsic frequencies ω_i of the filters i = 2–6 and i = 18–20 were selected equal to 10, while those for i = 8–10, i = 13–16, and i = 22–30 were taken equal to 30. The Q-values of the filters with i = 1–6 and i = 18–20 were selected

equal to 4, while those for i = 8–10, i = 13–16, and i = 22–28 were taken equal to 10. The coupling coefficients were β_i = 0.1 (for i = 2, 18); 0.2 (6, 10, 20, 24); 0.25 (14, 16, 26, 28); 0.3 (5, 8, 19, 22); and 1 (2, 18). In all cases we assumed that $\gamma = 0.5$. The values of parameters determining the nonlinear characteristics of the multipliers and the detector were as follows: $\nu = 0.01$; $\mu = 0.002$; $\xi_0 = 0.1$; $\xi_1 = 0.2$; and $\xi_2 = 2$. The parameter of the integrating circuit was $\zeta = 1$. For illustrative purposes, the informative signal was taken in the form of $F(t) = A_0\cos(\Omega t)$. The regular oscillations were described by the following parameters: $A_s = 1$; $A_0 = 0.4$; $\omega_s = 30$; and $\Omega = 1.2$. In the detector, the filter parameters were $\omega_{32} = 1.2$, $Q_{32} = \beta_{32} = 1$.

Figure 2a shows the power spectrum of oscillations at the output of summing device *4*. Figure 2b shows the temporal fragment for $t \in [153, 173]$. Figures 2c and 2d present the corresponding patterns (in the same time interval of the signal at the transmitter input and receiver output, respectively. As can be seen (Fig. 2a), the power spectrum $S(x_{11})$ exhibits maxima at the frequencies ω = 10 and 30. The regular (informative) signal $F(t)$ is masked. The temporal fragment in Fig. 2b shows a chaotic oscillatory process $x_{11}(t)$, in which the regular signal is not distinguished either. If the method of signal conversion is unknown, the transmitted harmonic oscillations cannot be isolated from the pattern of Fig. 2b.

The regular oscillations $x_{32}(t)$ separated in the detector (Fig. 2d) exhibit not only a phase shift relative to the transmitted signal (Fig. 2c) but, naturally, some distortions of the sinusoidal shape as well. The latter circumstance is explained by the insufficient filtration of the chaotic oscillations at a frequency of ω = 10 and on the third harmonic (ω = 30) in the receiver circuits. One of these circuits contains filter *9*, and another, converter *10* and filter *11*. Upon attenuation (approximately tenfold) of the mutual penetration of chaotic oscillations with peak powers at the frequencies ω = 10 and 30 into receiver circuits, distortions of the transmitted signal become insignificant. However, an increase in the degree of penetration of the above oscillations into the receiver circuits leads to an increase in the level of distortions in the received signal. Note that these distortions may be absent (even with no filtration at all), provided that two channels are employed in the transmission line *6*. This is possible in the case of cable or optical fiber lines.

The above analysis indicates that the proposed method of signal conversion offers an effective means of transmitting confidential information via a radio channel. An advantage of this method is that both oscillations generated by a dynamical system with chaotic behavior and noise signals can be employed as the masking signal. Use of the chaotic oscillations in the mathematical model is expedient because the results of such calculations are reproducible. In addition, chaotic oscillations are widely used in communication systems.

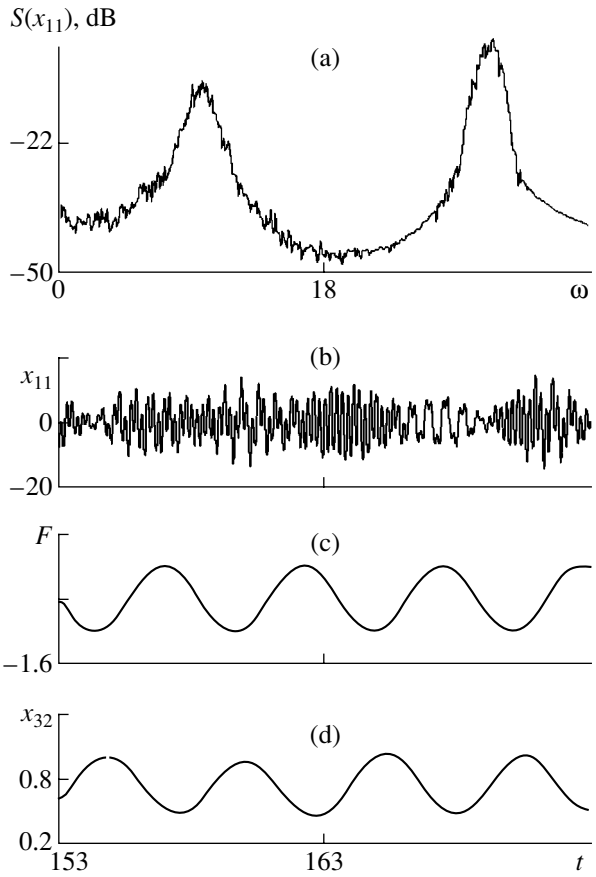

Fig. 2. Operation of the proposed data transmission system illustrated by (a) signal power spectrum, (b) the corresponding time pattern, and (c, d) signal shapes at the transmitter input and receiver output, respectively.

In practically implementing the proposed method of hidden data transmission, it is necessary to find a compromise between the range of data transmission and secrecy, since this relationship depends on many factors. Similar to many other methods of hidden communications (see, e.g., [2, 3, 8], the amplitude of masking oscillations must be at least ten times that of the informative signal. This circumstance hinders to a certain extent the use of transmitters with high output power, restricting the method to short-range communications. The working frequency range seems to pose no significant restrictions upon this method of data transmission, but it seems that most expedient applications are in the decimetric wavelength range. The employment of the proposed method poses high requirements with respect to the identity of the coding elements used in the transmitter and receiver circuits: the difference between these elements must not exceed 6–8%.

It must be noted that, in the case of a large shift of the "mean" frequency of the chaotic oscillations, it is expedient to employ two communication channels, naturally, with separate amplifiers and antennas. In the case of a large separation between the transmitted

bands of chaotic oscillations, the proposed masking method seems to offer better prospects for data transmission via cable or optical fiber lines. It is important to note that, systems using two channels (with each band of the chaotic oscillations transmitted via its own channel) require no filtering devices. characterized by relatively small losses and a weak dispersion, optical fiber transmission lines show especially good prospects. Using these lines naturally implies that chaotic oscillations employed in the data transmission channel (after amplifier 5) must be converted by the corresponding optoelectronic means into the optical frequency range. Two communication channels should be employed with a small shift of the mean frequency of the narrowband chaotic oscillations, which can be provided by oscillation mixing. In this case, it is possible to use one antenna and nondistorting (linear) amplifiers.

Acknowledgments. This study was supported by the Russian Foundation for Basic Research, project no. 98-07-90 299.

REFERENCES

1. L. Kocarev, K. S. Halle, K. Eckert, *et al.*, Int. J. Bifurcation Chaos Appl. Sci. Eng. **2** (3), 709 (1992).
2. A. R. Volkovskiĭ and N. F. Rul'kov, Pis'ma Zh. Tekh. Fiz. **19** (3), 72 (1993) [Tech. Phys. Lett. **19**, 97 (1993)].
3. I. I. Matrosov, Pis'ma Zh. Tekh. Fiz. **22** (23), 4 (1996) [Tech. Phys. Lett. **22**, 952 (1996)].
4. L. M. Pecora, T. L. Caroll, G. A. Johnson, *et al.*, Chaos **7** (4), 520 (1997).
5. V. D. Shalfeev, G. V. Osipov, A. K. Kozlov, *et al.*, Zarubezhn. Radioélektron. Usp. Sovremen. Radioélektron., No. 10, 27 (1997).
6. É. V. Kal'yanov, Radiotekh. Élektron. (Moscow) **43** (2), 206 (1998).
7. A. S. Dmitriev, L. V. Kuz'min, A. I. Panas, *et al.*, Radiotekh. Élektron. (Moscow) **43** (9), 1115 (1998).
8. A. S. Dmitriev and L. V. Kuz'min, Pis'ma Zh. Tekh. Fiz. **25** (16), 71 (1999) [Tech. Phys. Lett. **25**, 665 (1999)].
9. Yu. I. Neimark and P. S. Landa, *Stochastic and Chaotic Oscillations* (Nauka, Moscow, 1987; Kluwer, Dordrecht, 1992).

Translated by P. Pozdeev

Technical Physics Letters, Vol. 27, No. 8, 2001, pp. 669–670. Translated from Pis'ma v Zhurnal Tekhnicheskoĭ Fiziki, Vol. 27, No. 16, 2001, pp. 10–14.

The Total Pressure Losses in a Flow Behind a Shock Wave Emerging from Channels of Various Geometries

T. V. Bazhenova, T. A. Bormotova, V. V. Golub, A. L. Kotel'nikov, and A. S. Chizhikov

Institute for High Energy Densities, Associated Institute for High Temperatures, Russian Academy of Sciences, Moscow, Russia

e-mail: bazhenova@hedric.msk.ru

Received March 7, 2001

Abstract—The total pressure losses in a flow behind a shock wave emerging from the open end of a round or square channel were experimentally studied. It was found that the total pressure behind the stagnation wave in a channel with a square cross section is lower than that in the case of a round channel. © *2001 MAIK "Nauka/Interperiodica".*

When a shock wave emerges from a channel, the flow pattern exhibits a non-automodel (non-self-similar) variation. For example, in the case of a three-dimensional square channel, the interaction of stagnation and shock waves gives rise to a complicated nonstationary three-dimensional flow field in which the flow structure varies differently in various directions [1, 2]. The interaction of an obstacle with a shock wave emerging from a round channel was studied for a subsonic [3] and supersonic [4] flow behind the incident shock wave. It was found [5] that the pressure drop at an obstacle can be controlled by partly blocking the channel output.

Previously [2], we demonstrated that the volume of a nonstationary barrel and the degree of gas expansion in this barrel are greater for the shock wave emerging from a channel with a square cross section than for the same wave emerging from a round channel; both values are also greater than those in an equivalent stationary flow. It was expected that an increase in the Mach number of the flow in front of the stagnation wave for a shock wave emerging from a square channel must be accompanied by greater pressure losses in the shock wave, with a relative decrease in the total pressure behind the stagnation wave.

The behavior of shock waves emerging from channels of various geometries was studied in a setup comprising a shock tube connected to a cylindrical vacuum chamber. The edge of the shock wave represented a replaceable flange with a round or square channel accommodated inside the tube. The shock tube edge with the flange (perpendicular to the tube wall) was placed against plane-parallel optical windows in the pressure chamber. The low- and high-pressure chambers were filled with air at an initial pressure of 4 kPa. The incident shock wave velocity was measured to within 1% by a base technique using pressure gauges. The time variation of the pressure at an obstacle arranged perpendicularly to the flow axis was measured with a Kistler-603B transducer. The pressure transducer was preliminarily calibrated to within 5% in the blunt end of the shock tube.

The flow pattern was visualized with the aid of a special shadowing device and monitored with a high-speed optomechanical camera. The reconstructed Toepler patterns showed that a shock wave emerging from the channel featured a system of oblique shock waves and a stagnation wave forming a barrel-like structure similar to that observed in an underexpanded supersonic jet. As is known [6], the distance from the nozzle edge to the stagnation wave during the formation of a supersonic jet increases with time in the early stage of the process and exhibits several oscillations, after which the stagnation wave occupies a stationary position and converts into the Mach disk. This stage could not be observed in our experiments because of the limited volume of the gas compressed by the shock wave in the tube. As a result, the stagnation wave coordinate continuously increased to become several times greater than the calculated stationary value.

In order to study the dependence of the total pressure losses behind the stagnation wave on the Mach number of the incident shock wave, we measured the pressure drop at an obstacle placed perpendicularly to the flow axis at a distance of $4.5d$ (duct gauge) from the channel edge. To provide for a correct comparison of the total pressure variation for the shock waves emerging from round and square channels, the equivalent distances from the edge to obstacle were preliminary determined for equal effective gauges (for the square cross section, this is the diameter of a circle with equal area). The interaction of the diffracted shock wave with the obstacle and the formation of a stagnation wave

1063-7850/01/2708-0669$21.00

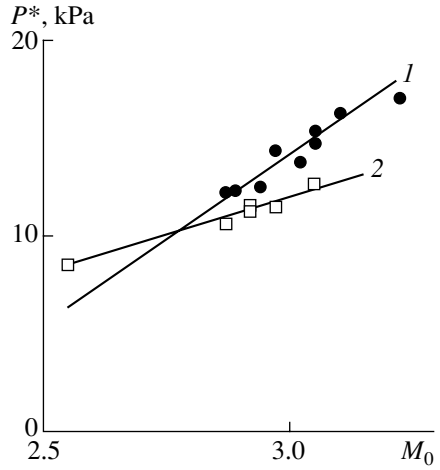

Fig. 1. Plots of the total excess pressure behind the stagnation wave versus the Mach number of the incident shock wave emerging from a channel with a (*1*) round and (*2*) square cross section.

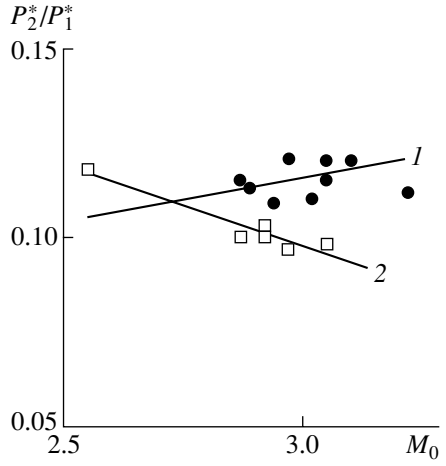

Fig. 2. Plots of the total pressure restore coefficient behind the stagnation wave versus the Mach number of the incident shock wave emerging from a channel with a (*1*) round and (*2*) square cross section.

behind the shock wave were studied using a sequence of the Toepler patterns. The reflected wave propagates upstream and interacts with the contact surface and with the stagnation wave. The latter wave occupies a stationary position. In this position, the distance from the stagnation wave to the obstacle for the square channel is smaller than for the round channel.

The pressure oscillograms exhibit two distinct regions: a pressure step ("peak") corresponding to the interaction of the obstacle with a diffracted shock wave and a quasistationary region ("shelf") corresponding to the interaction of the obstacle with the flow behind the contact surface. The total pressure measured on the "shelf" behind the stagnation wave was greater for the round channel than for the square channel. This difference increased with the Mach number (Fig. 1).

The ratio of the total pressure P_2^* behind the stagnation wave at the obstacle to the total pressure P_1^* at the channel edge (the restore coefficient) is a characteristic of the total pressure losses in a system of shock waves formed as a result of interaction of the obstacle with the diffracted shock wave and with the stagnation wave in the flow behind the contact surface. The total flow pressure at the channel edge is determined by the Mach number of the cocurrent (mass) flow behind the incident wave. This quantity is a known function of the initial Mach number M_0 of the incident shock wave, which increases with the M_0 value. In the channels of different geometries, the restore coefficients depend differently on the Mach number M_0 of the incident shock wave (Fig. 2).

Thus, the results of our experiments showed that the total pressure losses behind the stagnation wave in a channel with a round cross section are lower than those in the case of a square channel. As the Mach number of the incident shock wave increases, the total pressure restore coefficient in the former case grows, while that in the latter case drops.

The observed regularities offer a means of controlling the total pressure in the shock wave emerging from a channel by changing the shape of its cross section. This may be of interest in a number of technical applications, such as combatting automobile exhaust noise, cleaning pressure vessels from carbon deposits, and eliminating dust from the surface of chips in microelectronic devices [7, 8].

REFERENCES

1. T. V. Bazhenova, V. V. Golub, T. A. Bormotova, *et al.*, Izv. Akad. Nauk, Mekh. Zhidk. Gaza, No. 3, 114 (1999).
2. T. V. Bazhenova, V. V. Golub, T. A. Bormotova, *et al.*, Teplofiz. Vys. Temp. **39** (1), 123 (2001).
3. B. Yu. Panov, A. I. Starshinov, and E. A. Ugryumov, Gazodin. Teploobmen **1**, 108 (1970).
4. T. V. Bazhenova, V. V. Golub, S. V. Bazarov, *et al.*, Izv. Akad. Nauk, Mekh. Zhidk. Gaza, No. 4, 110 (1999).
5. T. V. Bazhenova, V. V. Golub, T. A. Bormotova, *et al.*, Pis'ma Zh. Tekh. Fiz. **26** (15), 32 (2000) [Tech. Phys. Lett. **26**, 659 (2000)].
6. V. A. Belavin, V. V. Golub, and I. M. Naboko, Prikl. Mekh. Tekh. Fiz., No. 1, 56 (1979).
7. Q. Yu and H. Gronig, Shock Waves, No. 6, 249 (1996).
8. G. T. Smedley, D. G. Phares, and R. C. Flagan, Exp. Fluids **26** (1/2), 116 (1999).

Translated by P. Pozdeev

Technical Physics Letters, Vol. 27, No. 8, 2001, pp. 671–673. Translated from Pis'ma v Zhurnal Tekhnicheskoĭ Fiziki, Vol. 27, No. 16, 2001, pp. 15–20.

Vacuum Electric Discharge Initiated by Accelerated Nanoparticles

S. V. Adamenko, P. A. Bereznyak, I. M. Mikhaĭlovskiĭ, V. A. Stratienko, N. G. Tolmachev, A. S. Adamenko, and T. I. Mazilova

Kharkov Physicotechnical Institute, National Scientific Center, Kharkov, Ukraine
Laboratory of Electrodynamic Investigations, ENRAN Company, Kiev, Ukraine

Received March 6, 2001

Abstract—A static breakdown induced by the impact of particles detached from a point anode in a strong electric field, corresponding to the athermal field evaporation threshold, was studied by field ion microscopy. Under these conditions, the particle size threshold for the vacuum discharge initiation decreases by one order of magnitude as compared to the case of flat electrodes and falls within a nanometer range of the average radius of bombarding charged particles. The threshold energies of particles initiating a static electric discharge also exhibit a significant decrease. *© 2001 MAIK "Nauka/Interperiodica".*

Investigations of the high-voltage vacuum discharges clearly demonstrated the determining role of the explosive emission centers formed in a pulsed discharge process [1–3]. Ectons, representing charged particle bunches, were originally also observed in the study of explosive (blow-up) emission processes. However, further investigations showed that ectons may also appear as a result of the microexplosion processes occurring on electrodes bombarded by accelerated microparticles [4]. An allowance for these effects made it possible to explain the main features of a static high-voltage vacuum discharge initiated by the impact of microparticles on the electrodes. However, the laws of such discharge initiation strongly depend on the particular experimental conditions, and the mechanism of this phenomenon is still not completely clear. The phenomena accompanying the static vacuum breakdown for electrodes bombarded with particles of micron and millimeter dimensions were more exhaustively studied [4, 5]. The breakdown initiated by the bombardment of smaller particles remains practically unstudied, which is explained to a considerable extent by difficulties encountered in the determination of the microparticle configurations and energies.

We have studied the static vacuum breakdown initiated by submicron particles using high-resolution field ion microscopy (FIM). This technique is capable of determining the size of particles and the local electric field strength. As a result, it was established that the particle size threshold for the initiation of a static vacuum breakdown in a strong electric field falls within a nanometer range of the radius of bombarding particles. Accordingly, the particle energy threshold for the discharge initiation is also shifted toward lower values.

The experiments were conducted in a two-chamber field ion microscope operating at a working voltage in the 2–30 kV range, using samples cooled with liquid hydrogen. The amplitude of relative voltage pulsations did not exceed 10^{-3}. The residual gas pressure in the inner working chamber was 10^{-6} Pa; the imaging gases were helium, neon, or hydrogen at a pressure varying from 10^{-1} to 10^{-3} Pa. The sources of charged microparticles were cone-shaped point tungsten anodes (99.98% W) with an apex angle of 10°–15° and a point tip curvature radius of 5–40 nm. The particles were produced by the fracture of the point tip under the action of ponderomotive forces of the applied electric field. The cathode had the form of a copper disk with a central hole and a surface polished by mechanical and electrochemical (orthophosphoric acid solution) methods. Ions passing through the hole (occurring on the optical axis of the microscope) formed an image of the point surface, which was amplified by a microchannel plate. A high voltage was applied to the point anode through a $2 \times 10^8\ \Omega$ resistor. The capacitance of the diode in which the electric breakdown was initiated was 200 pF. The electric discharge was detected by a jump of the voltage across the diode and by a flash of light. In order to eliminate vacuum discharges initiated by the field electron emission and evaporation of the anode, the diode was subjected to high-voltage training. The experiments on the breakdown initiated by accelerated microparticles were started upon reaching a vacuum insulation strength of not less than 25 kV. After the high-voltage training, a series of 20–30 experiments was conducted without breaking vacuum in the working chamber. The point anodes that degraded during the experiments were replaced with the aid of a high-vacuum-lock preparation chamber.

1063-7850/01/2708-0671$21.00 © 2001 MAIK "Nauka/Interperiodica"

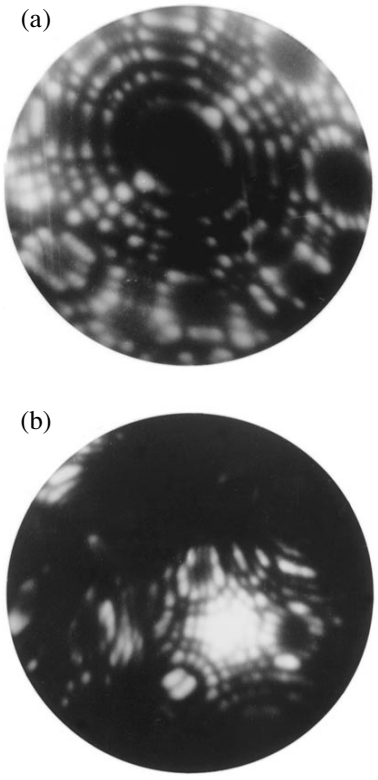

Fig. 1. FIM images of the point anode (a) before and (b) after a breakdown.

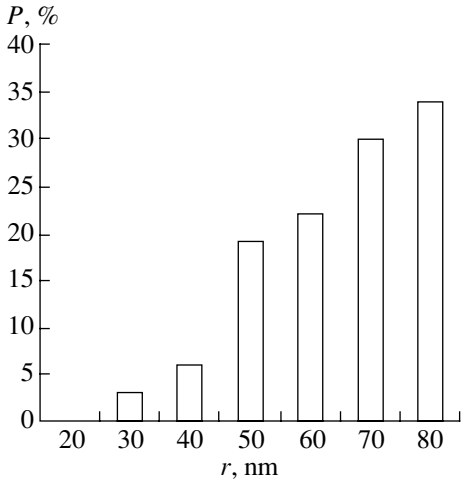

Fig. 2. A histogram of the probability P of the breakdown initiation versus the nanoparticle curvature radius r.

The curvature radii of the cylindrical particle surface were determined by the number of atomic steps (formed in the course of the field evaporation) between the crystallographic poles with low Miller indices [6]. The particle lengths were determined (in the experiments not involving breakdowns) by a change in the average curvature radius of the point tip upon the field-induced fracture. Since the mechanical stresses rapidly decay with a distance from the point tip, the point anode was usually fractured and the microparticles formed in a region spaced by 1–3r from the tip. Therefore, the detached anode fragments might possess a configuration far from spherical. While, the anode tip radius could be determined with an accuracy of 4–8%, the average length of a detached fragment was estimated at a relative error of about 50%. The breakdown usually resulted in the anode curvature radius increasing by more than one order of magnitude and the formation of microprotrusions on the anode surface [7]. These surface features make the main contribution to the formation of anode images in FIM (Fig. 1).

The field strength at the cone-shaped point tip shaped by the field evaporation is approximately constant and equal to $E = V/(5r)$. Only slight variations in the field strength related to the anisotropy of the field evaporation energy were observed [5]. On the cone-shaped point anode surface, The electric field strength E significantly drops and, in determining the charge Q of a broken particle, we may only take into account a field strength over the hemispherical part of the point anode:

$$Q = 2\pi\varepsilon_0 E r^2, \tag{1}$$

where ε_0 is the dielectric constant and r is the curvature radius of the point anode. The electric field strength component directed along the anode axis is

$$F = \pi r^2 \varepsilon_0 E^2/2. \tag{2}$$

In an electric field with a strength of $2–6 \times 10^{10}$ V/m, the ponderomotive forces may significantly exceed a macroscopic yield point and reach a theoretical limiting strength of the point anode material [8]. Assuming that the particle charge remains unchanged on the acceleration path and using formula (1), we may express the kinetic energy as

$$W = 10\pi\varepsilon_0 E^2 r^3. \tag{3}$$

Figure 2 shows a histogram of the probability P of the breakdown initiation by the impact of microparticles on the copper cathode. The probability is plotted versus the particle radius r taken equal to the radius of curvature of the hemispherical point anode. As the curvature radius of the bombarding particles increases, the breakdown probability grows to reach 34% for r in the interval from 75 to 85 nm. The process of breakdown initiation by the microparticles exhibits a threshold character, being possible only for particles with a curvature radius above 30 nm. This value is one order of magnitude lower than the corresponding threshold value determined in experiments with macroscopic (flat) electrodes [4].

The detachment of nanoparticles took place in the course of the anode surface shaping by the field evaporation at a constant electric field strength at the anode

surface (56–58 V/nm), which corresponded to an evaporation rate of 0.2–1.5 atomic monolayers per second. The diode voltage increased from 5.6 to 22.4 kV, proportionally to the point tip curvature radius. Accordingly, the energy of particles bombarding the copper cathode varied from 6.9×10^{-12} to 4.5×10^{-10} J. Calculated by formula (3), the threshold value of the energy necessary for initiating the vacuum discharge is 5.58×10^{-11} J. This estimate is two orders of magnitude lower than the values for the discharge initiation by microparticles broken from a flat anode. However, a specific energy is constant (20.6 eV/atom) in the entire interval of applied voltages. This energy is sufficient to produce local melting and evaporation of the cathode material, as well as for the complete evaporation of the particle, resulting in the formation of a near-surface plasma with a density close to the solid-state material density. It was demonstrated [5] that the interaction of such plasma with the cathode leads to the formation of an ecton responsible for breakdown of the vacuum gap.

Thus, microscopic fragments detached from the point anodes occurring in ultimately high electric fields (on the order of 10^{10}–10^{11} V/m, which corresponds to the athermal field evaporation of metals) are accelerated to energies significantly greater than the heat of sublimation. As a result, the particle size threshold for the vacuum discharge initiation falls within a nanometer range. The specific energies and velocities of such accelerated particles not only exceed the corresponding values achievable in the experiments with flat electrodes but apparently reach a limiting possible level. Indeed, an increase in the particle charge above the level observed in the experiments with point anodes unavoidably leads to the field evaporation and a decrease in the charge of detached nanoparticles.

Acknowledgments. The authors are grateful to P.I. Fomin for fruitful discussions and to E.I. Lugovskaya for her help in conducting the experiments.

REFERENCES

1. G. A. Mesyats and D. I. Proskurovsky, *Pulsed Electric Discharge in Vacuum* (Nauka, Novosibirsk, 1984; Springer-Verlag, Berlin, 1989).
2. G. A. Mesyats, *Ectons* (Nauka, Yekaterinburg, 1993), Part 1.
3. G. N. Furseĭ and V. M. Zhukov, Zh. Tekh. Fiz. **46** (2), 310 (1976) [Sov. Phys. Tech. Phys. **21**, 176 (1976)].
4. I. N. Slivkov, *High-Voltage Processes in Vacuum* (Énergoatomizdat, Moscow, 1986).
5. G. A. Mesyats, *Ectons* (Nauka, Yekaterinburg, 1994), Part 2.
6. M. K. Miller, L. Cerezo, M. G. Hetherington, and G. D. W. Smith, *Atom Probe Field Ion Microscopy* (Clarendon, Oxford, 1996).
7. E. L. Kontorovich, T. I. Sudakova, and V. N. Shrednik, Pis'ma Zh. Tekh. Fiz. **25** (10), 69 (1999) [Tech. Phys. Lett. **25**, 410 (1999)].
8. I. M. Mikhaĭlovskiĭ, P. Ya. Poltinin, and L. I. Fedorova, Fiz. Met. Metalloved. **56** (1), 186 (1983).

Translated by P. Pozdeev

Technical Physics Letters, Vol. 27, No. 8, 2001, pp. 674–676. Translated from Pis'ma v Zhurnal Tekhnicheskoĭ Fiziki, Vol. 27, No. 16, 2001, pp. 21–26.

Internal Magnetic Relaxation in Levitating Superconductors

B. M. Smolyak, G. N. Perel'shteĭn, and G. V. Ermakov

Institute of Thermal Physics, Ural Division, Russian Academy of Sciences, Yekaterinburg, Russia

e-mail: b-smolyak@yandex.ru

Received February 23, 2001

Abstract—The effect of stopping the levitation force relaxation was observed upon reversal of the superconductor magnetization. A model of the internal magnetic relaxation in levitating superconductors is proposed, according to which both the magnetic moment and the force acting upon the sample are constant. © *2001 MAIK "Nauka/Interperiodica".*

The magnetic flux creep leads to magnetic moment relaxation in superconductors. The relaxation rate sharply decreases upon reversal of the field magnetizing the sample [1–3] or under the action of a variable magnetic field [4]. The authors of those papers failed to explain this phenomenon assuming that it is caused by a decrease in the creep rate in the volume of superconductors. (As is well known [5], the creep can only be suppressed by increasing the vortex activation energy.) Below we report on the results of the investigation of the levitation force relaxation. We observed the effect of the levitation stabilization. We believe that the nature of the effect is related to the internal magnetic relaxation.

We have measured the relaxation of the force holding a superconductor in the state of levitation below a ring-shaped magnet. A sample of the fused YBaCuO ceramics had the shape of a disk with a diameter of 10 mm and a thickness of 3.5 mm; the SmCo magnet was $30 \times 18 \times 8$ mm in size. The disk and magnet planes were parallel and the common symmetry axis z was vertical. The average magnetic field induction on a level of the sample suspension was about 0.1 T and the average induction gradient was ~0.3 T/cm. The sample was cooled down to 78 K at the center of the magnet and magnetized by moving along the z axis up to the point of suspension either directly or with reversal. In the latter case, the sample was first moved down and then returned to the suspension point. As a result, the sample acquired a unipolar or bipolar magnetization, whereby the magnetic moments of circulating currents were oriented either parallel or antiparallel to each other in the z axis direction. The current density at the onset of relaxation was $J(t_0) = 4 \times 10^3$ A/cm^2. The levitation force F was equilibrated by a load $P–G$, where P is the total weight of the sample and the loading device ($P > F$) and G is a controlled force applied to the loading device. The measurements were started at the time instant $t_0 = 1$ min after placing the sample at the point of suspension.

Figure 1a shows the plots of normalized levitation force versus time for the direct magnetization (without reversal), while Fig. 1b resents the time variation of the levitation force in the case of the sample magnetization with reversal. The F^* value was normalized to the force F_0 acting in the absence of the magnetization reversal. The force ratio at the beginning of relaxation determines the reversal coefficient $f^* = F^*/F_0$ (here and below, the values referring to the case of magnetization reversal are denoted by asterisks; the subscript refers to time, e.g., $F^*(t_0) \equiv F_0^*$ etc.) Note the following features in the system behavior: (i) the reversal of the external

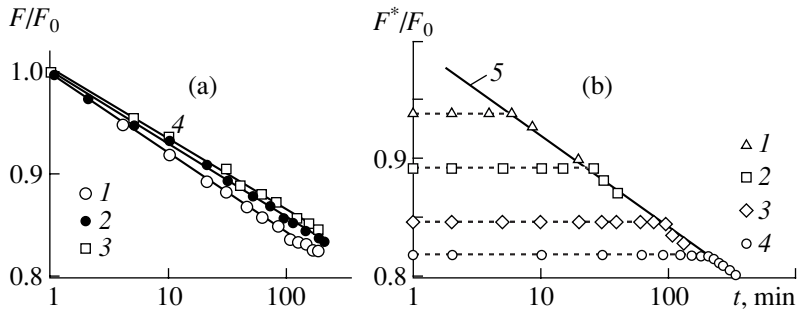

Fig. 1. Relaxation of the levitation force: (a) unipolar magnetization, $F_0 = 0.35$ (*1*), 0.21 (*2*), 0.14 H(*3*); (b) bipolar magnetization, $F_0^*/F_0 = 0.94$ (*1*), (*2*) 0.89, 0.845 (*3*), 0.82 (*4*), 1 (*5*) (see Fig. 1a, curve *1*); $F_0 = 0.35$ H.

1063-7850/01/2708-0674$21.00 © 2001 MAIK "Nauka/Interperiodica"

magnetic field leads to the levitation force relaxation stopping; (ii) the levitation stabilization time depends on the reversal coefficient; (iii) the force F^* remains constant over the time period required for reducing the nonreversal force F from F_0 to f^*F_0; (iv) after this period of time, the force F^* starts decreasing at the same rate as F.

Let us consider relaxation of the force acting upon a superconducting disk having a structure of opposite azimuthal currents with a density J_θ. A resultant force in the z direction is determined by integrating a ponderomotive force density $J_\theta B_r$ over the superconducting disk volume; B_r is the radial magnetic induction component, by which we may imply the external magnetic field [6]. A calculation of the field generated by the ring magnet showed that $B_r(r, z) \cong B_r(R, z)r/R$, where R is the disk radius. Assuming that the current density depends only on the radius, $J_\theta = J_\theta(r)$, we may write an expression for the force as

$$F^* = \Phi M^*, \tag{1}$$

where Φ is the magnetic flux passing through the side surface of the disk and M^* is the disk magnetization in the z direction. For a bipolar current structure, the magnetization is

$$M^* = \frac{1}{3}JR[2(r^*/R)^3 - 1], \tag{2}$$

where r^* is the radius of the surface separating regions with opposite circulating currents. We use the Been model according to which the currents are distributed with a constant density (for simplicity, the subscript "θ" at the current density J is omitted). In the case of a unipolar magnetization, $M = M^*(r^* = R) = JR/3$.

In relationship (1), the magnetic flux Φ is independent of time; therefore, variation of the force with time is due to a change in the magnetization. The current density relaxation can be described as $J(t > t_0) = J(t_0)\alpha(t)$, where $\alpha(t) < 1$ is the current relaxation coefficient. According to a linear theory of the magnetic flux creep [5],

$$\alpha(t) = 1 - \frac{kT}{U}\ln\frac{t}{t_0}, \tag{3}$$

where U is the effective activation energy. Since the unipolar magnetization is proportional to the current density ($M \sim J$), the current density, magnetization, and force possess the same relaxation coefficient: $\alpha(t) = J(t)/J_0 = M(t)/M_0 = F(t)/F_0$. Figure 2a shows a radial distribution of the magnetic induction in the case of a unipolar magnetization. During the creep, the vortices move to the side surface of the disk ($r^* = R$) and escape from the sample. As a result, the induction gradient and the current density decrease (assuming the distribution preserves its linearity [7]). This is a well-known mechanism of the magnetic relaxation (referred to as the "open" type), which is related to the flow of vortices passing through the superconductor surface.

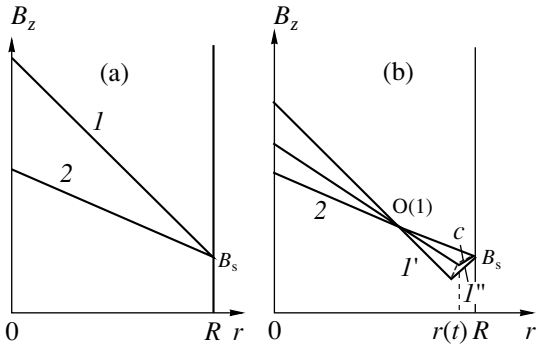

Fig. 2. Magnetic induction distribution in a disk with (a) unipolar and (b) bipolar magnetization at $t = t_0$ (*1*, *1*'–*1*") and $t \geq t_i$ (*2*); B_s is the induction at the side surface.

In the case of a bipolar magnetization, the initial distribution of the magnetic induction is described by a broken line (Fig. 2b) comprising linear portions *1*' and *1*". During the creep, the vortices move to the side of lower vortex density, that is, toward the boundary r^* between the regions *1*' and *1*"). This boundary will also move if the flows from regions *1*' and *1*" are unequal. Let us consider the case when the flow from region *1*' exceeds the counterflow ($r^*(t_0) > R/\sqrt[3]{2}$). We will assume that (i) the induction gradients in regions *1*' and *1*" decrease at the same rate and (ii) both regions retain linear flux profiles. Under these conditions, the distributions *1*' and *1*" rotate by the same angle around the centers $O(t)$ and B_s, respectively (Fig. 2b). (The point $O(t)$ determines the average vortex density in region *1*' at a given time instant). The angle between lines *1*' and *1*" increases, while the angle vertex travels along the curve c toward point B_s (i.e., the boundary r^* tends to R). We may write a differential equation $2\alpha(dr^*/d\alpha) = R - 4r^*/3$ and integrate it to obtain

$$r^*(t) = \frac{1}{4}R[3 + (\alpha_i/\alpha(t))^{2/3}], \tag{4}$$

where $\alpha_i \equiv \alpha(t_i)$, t_i is the time instant at which r^* reaches the side surface. Using formulas (2) and (4), the coefficient of relaxation of the bipolar magnetization can be written as

$$\beta^*(t) = \frac{M^*(t)}{M^*(t_0)} = \frac{\alpha(t)\{[3 + (\alpha_i/\alpha(t))^{2/3}]^3 - 32\}}{[3 + \alpha_i^{2/3}]^3 - 32}. \tag{5}$$

Expanding this expression in powers of $1 - \alpha_i/\alpha(t)$ and $1 - \alpha_i$ and retaining the terms up to the third power, we obtain

$$\beta^*(t) = 1 + \frac{1}{36\alpha_i}[(1 - \alpha_i)^3 - (1 - \alpha_i/\alpha(t))^3\alpha(t)]. \tag{6}$$

From Eq. (6) we infer that the magnetization increases with time: for $t \le t_i$, $\alpha(t) \ge \alpha(t_i)$ and $\beta^*(t) > 1$. A relative change of the magnetization during the time t_i is $1 - \beta^*(t_i) = -(1 - \alpha_i)^3/36\alpha_i$. This quantity can be estimated assuming that $M^*(t_i) = M(t_i)$ and $\alpha_i = \beta^*(t_i)f^*$, where $f^* = M_0^*/M_0 = F_0^*/F_0$ is the reversal coefficient. For $f^* = 0.8$, we obtain $|1 - \beta^*(t_i)| \cong 3 \times 10^{-4}$ which implies that a change in the magnetization during the time t_i is negligibly small. Thus the current density and its distribution in the volume change so that the magnetic moment remains unaltered.

Therefore, an internal magnetic relaxation takes place, whereby the magnetic flux is redistributed in the sample. During this, the field state at the sample boundary remains unchanged and, hence, the total force acting upon the system of closed currents is constant. The internal relaxation time can be estimated assuming that $\beta^*(t_i) = 1$ and $\alpha(t_i) = f^*$. Using formula (3), we obtain

$$t_i = t_0 \exp\left[(1 - f^*)\left(\frac{U}{kT}\right)\right]. \quad (7)$$

This relationship provides a good description of the results of measurements of the levitation stabilization time (the value $U/kT = 30$ was determined as reciprocal to the logarithmic relaxation rate $(dF/d\ln t)/F_0$ for curve *1* in Fig. 1a). At $t = t_i$, the system goes out of the internal magnetic relaxation state possessing a homogeneous current structure with a current density $J(t_i) = J_0\alpha(t_i)$. Subsequent relaxation proceeds by a mechanism of the open type.

REFERENCES

1. M. R. Beasly, R. Labush, and W. W. Webb, Phys. Rev. B **181**, 682 (1969).
2. K. Kwasnitza and Ch. Widmer, Physica C (Amsterdam) **184**, 341 (1991).
3. K. Kwasnitza and Ch. Widmer, Cryogenics **33**, 378 (1993).
4. É. V. Matizen, P. P. Bezverkhiĭ, and V. G. Martinets, Zh. Éksp. Teor. Fiz. **111**, 1047 (1997) [JETP **84**, 578 (1997)].
5. Y. Yeshurun, A. P. Malozemoff, and A. Shaulov, Rev. Mod. Phys. **68**, 911 (1996).
6. L. D. Landau and E. M. Lifshitz, *Course of Theoretical Physics*, Vol. 8: *Electrodynamics of Continuous Media* (GITTL, Moscow, 1957; Pergamon, New York, 1984).
7. G. Blatter, M. V. Feigelman, V. B. Geshkenbein, *et al.*, Rev. Mod. Phys. **66**, 1125 (1994).

Translated by P. Pozdeev

Technical Physics Letters, Vol. 27, No. 8, 2001, pp. 677–678. Translated from Pis'ma v Zhurnal Tekhnicheskoĭ Fiziki, Vol. 27, No. 16, 2001, pp. 27–31.

Wave Propagation in a Liquid Flowing in a Channel with Elastic Walls

Yu. N. Zaĭko

Volga Region Academy of State Service, Saratov, Russia

Received March 6, 2001

Abstract—Wave propagation in the ideal liquid flowing in a cylindrical circular channel is described. The channel is considered as an elastic shell and the interaction of density and pressure waves in the liquid with elastic waves in the walls is taken into account. It is shown that the flow may exhibit instability under certain conditions. Conditions for the convective and absolute instability development are determined. The pattern of instability development and the onset of turbulence in this model differs from the analogous scenario in a viscous liquid model. © *2001 MAIK "Nauka/Interperiodica".*

Consider a stream of liquid (or gas) flowing in a circular channel (tube) with the cross section area $A = \pi a^2$, where a is the tube radius. Assuming that A is sufficiently small, the liquid density and velocity in this channel can be described in an approximation taking into account only the velocity component v along the tube axis. The corresponding one-dimensional problem is described by a system of equations in terms of A, v, and the pressure p depending on the longitudinal coordinate x only [1].

Following Lamb [1], we write a set of equations in a dimensionless form using the following quantities as the time, length, and pressure units, respectively:

$$T = \sqrt{\frac{\rho a^2}{E}}, \quad L = \sqrt{\frac{\rho a h}{2\rho_0}}, \quad P = \frac{Eh}{2a}.$$

Here ρ_0 is the liquid density, ρ is the density of the channel wall material, h is the wall thickness, and E is the Young modulus of the wall.

The initial system of equations can be written as

$$\begin{aligned} A_t + (Av)_x &= 0, \\ v_t + vv_x + p_x &= 0, \\ A_{tt} + RA_{xxxx} + A - p &= 0, \end{aligned} \tag{1}$$

where t is the dimensionless time and subscripts denote partial derivatives. The first equation in system (1) represents the equation of continuity, the second is the equation of motion in Euler's form, and the third relationship described elastic waves in the channel wall considered as an elastic shell (tube). The term RA_{xxxx} takes into account the interaction between waves in the stream and bending waves in the wall, which becomes significant for the wavelengths $\lambda \le (ah)^{1/2}$ [2]; the quantity $R = \rho_0^2[3(1-\mu^2)\rho^2]$ is the so-called cylindrical rigidity, and μ is the Poisson coefficient [2]. In this form, the last equation in system (1) was used to study the waves in cylindrical shells arising under the action of a distributed external load [3]. This relationship can be derived from rigorous equations describing the waves in cylindrical shells [4], in which only the terms most significant in the approximation considered are retained. The relative pressure is unity ($p = 1$) at the points where the flow velocity is equal to the average value ($v = v_0$).

Let us consider the case of small-amplitude waves and represent variables in the form $v = v_0 + v'$, $A = 1 + A'$, and $p = 1 + p'$, where $v' \ll v_0$, $A' \ll 1$, and $p' \ll 1$. A solution to the linearized Eqs. (1) will be found in the form of $\sim\exp(ikx - i\omega t)$. Substituting this expression into the initial system yields a dispersion relationship between wavenumber k and frequency ω:

$$D(\omega, k) = (1 + Rk^4 - \omega^2)k^2 - (kv_0 - \omega)^2 = 0. \tag{2}$$

Figure 1 shows a solution to Eq. (2) for various v_0 and a curve of the marginal stability $v_0(k)$, which is obtained from (2) assuming the absence of increasing solutions of the linearized system:

$$v_0(k) = \frac{1}{k}\sqrt{(1+k^2)(1+Rk^4)}. \tag{3}$$

This curve with minimum $v_{0m} = v_0(k_m)$ has a shape characteristic of such problems (Fig. 1). Here and below, the imaginary part of the frequency is $\mathrm{Im}(\omega(k)) = 0$, while above $\mathrm{Im}(\omega(k)) \neq 0$. Therefore, the $v_0(k)$ curve separates the regions of stable and unstable motion of liquid in the channel. In the region of $v_0 < v_{0m}$, the flow is stable: any small perturbation does not increase with time and the motion remains one-dimensional for an arbitrary long time. Indeed, multidimensional perturbations arising on the background of the one-dimensional flow possess a greater energy than the one-dimensional perturbations. For $v_0 > v_{0m}$, the perturbations with wavenumbers in a small vicinity of k_m grow and violate the one-dimensional flow character. The size of this instability region in the vicinity of k_m varies as $\sim(v_0 - v_{0m})^{1/2}$.

1063-7850/01/2708-0677$21.00

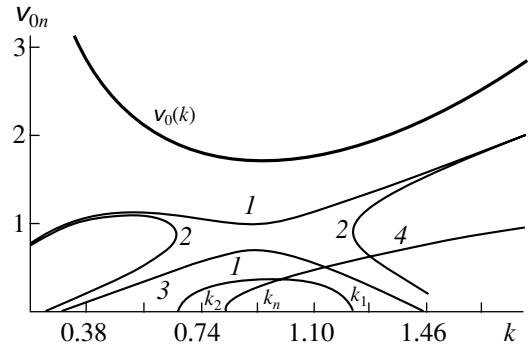

Fig. 1. Solutions to Eq. (2) and the curve of marginal stability (3) for $R = 0.51$: (*1*) $\omega(k)$ function for $v_0 = 1.7 < v_{0m}$; (*2*, *3*) $\mathrm{Re}(\omega(k))$ and $\mathrm{Im}(\omega(k))$ for $v_0 = 1.89 > v_{0m}$, respectively; (*4*) the curve of singular points $D(k(\omega), \omega)$ obtained from Eq. (4).

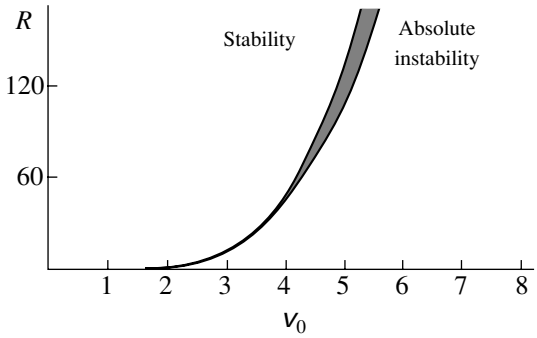

Fig. 2. The $R(v_0)$ curves obtained from Eqs. (5) and (6) (right- and left-hand boundaries of the shadowed region, respectively) separating the (R, v_0) plane into three regions with different character of the stability of solutions to the linearized system (1). The narrow shadowed region corresponds to the convective instability.

According to the theory of instabilities [5], an instability is absolute (convective) if the curve $\mathrm{Im}(\omega(k))$ [obtained from (2)] is lying on the plane of the complex variable ω farther (closer) from the real frequency axis than the line $\omega = \omega_s(k)$ containing zeros of the function $D_k(k(\omega), \omega)$ or the branching points of the function $k(\omega)$ [also obtained from (2)]. An equation for $\omega_s(k)$ is determined by solving the system of equations $D(k(\omega), \omega) = 0$ and $D_k(k(\omega), \omega) = 0$ and has the form

$$\omega_s(k) = \frac{k}{1+\frac{2}{3}k^2} \times\left\{\frac{5}{6}v_0 \pm \sqrt{\frac{25}{36}v_0^2 + \frac{2}{3}(1-v_0^2)\left(1+\frac{2}{3}k^2\right)}\right\}. \quad (4)$$

For $k < k_1 = 1/4\sqrt{(v_0^2+24)/(v_0^2-1)}$, the curve $\omega_s(k)$ passes along the real axis on the complex frequency plane, while for $k > k_1$ this curve goes to the complex plane as depicted in Fig. 1. The condition of coincidence of k_1 and k_2 (determining the right-hand boundary of the instability region (Fig. 1) yields an equation for the boundary between the regions of convective and absolute instability in the (Rv_0) plane (depicted by the right-hand curve in Fig. 2):

$$R = 256\frac{(v_0^2+8)(v_0^2-1)^3}{(17v_0^2+8)(v_0^2+24)}. \quad (5)$$

The left curve in Fig. 2 represents a boundary between the regions of stability and convective instability. This curve is obtained by solving the equation $R = R(k_m)$, where

$$R(k) = \frac{v_0^2}{(1+k^2)k^2} - \frac{1}{k^4}; \quad k_m^2 = \frac{4 - v_0^2 + v_0\sqrt{v_0^2+8}}{4(v_0^2-1)}; \quad \frac{dR(k_m)}{dk} = 0. \quad (6)$$

The results indicate that an allowance for the bending rigidity of the channel walls leads to the appearance of a new mechanism of the energy transfer (redistribution) in the spectrum as compared to the case of viscous flow. The new mechanism is based on the excitation of elastic waves in the channel walls by waves in the liquid. This, in turn, accounts for a different scenario of the transition to the turbulent regime in the channel with elastic walls, which was experimentally observed by Krindel and Silberberg [6].

On the one hand, an allowance for the interaction between waves in the liquid and elastic waves in the walls results in that (even for a very small interaction, $R \longrightarrow 0$) the axisymmetric flow is unstable with respect to small perturbations (in the absence of this interaction, the flow possessed both convective and absolute stability at any velocity v_0 [2]).

On the other hand, a sufficiently strong interaction ensuring the transfer of a considerable fraction of energy from waves in the liquid to elastic waves in the wall leads to a delay in the development of instability in the flow and in the passage to the turbulent regime.

REFERENCES

1. G. L. Lamb, Jr., *Elements of Soliton Theory* (Wiley, New York, 1980; Mir, Moscow, 1983).
2. L. D. Landau and E. M. Lifshitz, *Course of Theoretical Physics*, Vol. 6: *Fluid Mechanics* (Nauka, Moscow, 1986; Pergamon, New York, 1987).
3. L. I. Slepyan, *Nonstationary Elastic Waves* (Sudostroenie, Leningrad, 1972).
4. A. S. Vol'mir, *Nonlinear Dynamics of Plates and Shells* (Nauka, Moscow, 1972).
5. A. I. Akhiezer, I. A. Akhiezer, R. V. Polovin, *et al.*, *Plasma Electrodynamics*, Ed. by A. I. Akhiezer (Nauka, Moscow, 1974; Pergamon, Oxford, 1975).
6. P. Krindel and A. Silberberg, J. Colloid Interface Sci. **71**, 39 (1979).

Translated by P. Pozdeev

Technical Physics Letters, Vol. 27, No. 8, 2001, pp. 679–682. Translated from Pis'ma v Zhurnal Tekhnicheskoĭ Fiziki, Vol. 27, No. 16, 2001, pp. 32–39.

Electrothermal Instability of a Polar Polymer Dielectric above the Glass Transition Temperature

O. A. Emel'yanov

St. Petersburg State Technical University, St. Petersburg, Russia

e-mail: elmf-dean@servccphtf.stu.neva.ru

Received March 21, 2001

Abstract—A stationary temperature state of a polar polymer dielectric exposed to an electric field is studied. A special feature of the dielectrics of this type is the presence of a maximum in the loss factor $\varepsilon''(T)$ above the glass transition temperature. Using an approach based on the Kirkwood formula for $\varepsilon''(T)$, exact solutions to a nonlinear model problem are obtained. These solutions show the multiplicity of the stationary temperature states and the surface of these states in the "load–ambient temperature" space of parameters exhibits a topological singularity of the "fold" type. © *2001 MAIK "Nauka/Interperiodica".*

1. Introduction. As is well known, the thermal state of a dielectric exposed to an electric field E may be unstable. In the region of high temperatures, the development of such instabilities terminates at a thermal breakdown. Limitation of the thermal breakdown current in dielectric structures leads to interesting electrokinetic phenomena accounting for a nonlinear character of the current–voltage (I–U) and capacitance–voltage (C–U) characteristics and for some other effects [1].

Such dissipative effects arise due to a strong dependence of the volume heat evolution q_v on the temperature T described by the formulas

$$q_v = \omega\varepsilon_0\varepsilon''E^2, \quad (1)$$

$$\varepsilon'' = \varepsilon_0''\exp(-W/kT), \quad (2)$$

where ω and E are the frequency and strength of the external electric field, ε'' is the loss factor, W is the activation energy, and k is the Boltzmann constant. A phenomenological theory of the electrothermal state of this system reduces to solving a nonlinear problem described by a thermal conductivity equation with the source term q_v.

A number of results were reported for such problems with a smooth ε'' functions, including those of the type (2) [2, 3]. At the same time, it is interesting to analyze the electrothermal state of a dielectric featuring a nonmonotonic $\varepsilon''(T)$ behavior (e.g., with a maximum), which is characteristic of a large class of polar polymer dielectrics such as PET and PVA. (Fig. 1). The nonmonotonic character of $\varepsilon''(T)$ may account for the appearance of several stationary temperature states. Transitions between these states in continuous dielectric films may proceed by an autowave mechanism. Some experimental data and estimates were reported in [4]. In that case, the stable temperature states and the temperature autowaves represented dissipative structures of the simplest types [5]. For dielectric samples of a finite thickness (modeled, e.g., by a flat capacitor), we may also expect a multiplicity of stationary temperature states of the system. Let us consider this problem in more detail.

2. Model description. Consider a one-dimensional model representing a thin plane capacitor with a dielectric of thickness $2h$ possessing a thermal conductivity λ. The dielectric occurs in an electric field $E = E_0\sin\omega t$ with the frequency $\omega > \omega_M$ ($\omega_M = \sigma/\varepsilon\varepsilon_0$ is the Maxwell frequency and σ is the electric conductivity). In this system, $E(x)$ = const (as follows from the condition $\mathrm{div}j_{tot} = \mathrm{div}(\sigma \cdot E(x)) = 0$, where j_{tot} is the total current in the dielectric). The stationary temperature field $T(x)$

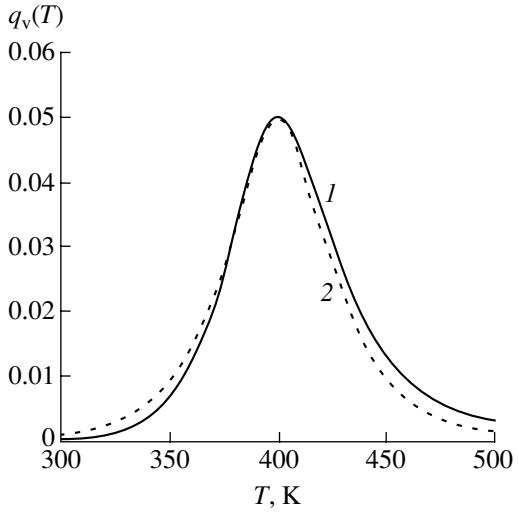

Fig. 1. The sources of bulk heat evolution described by (*1*) the Kirkwood formula (6) and (*2*) the model (7).

1063-7850/01/2708-0679$21.00

in the system is determined by solving the following nonlinear problem:

$$\begin{cases} \dfrac{d}{dx}\lambda(T)\dfrac{dT}{dx} + q_v(T) = 0; \quad \left.\dfrac{dT}{dx}\right|_0 = 0, & (3) \\ \text{with boundary conditions of type III} \\ \lambda(T)\left.\dfrac{dT}{dx}\right|_{\pm h} = \mp\alpha(T|_{\pm h} - T_0) & (4) \\ \text{or of type I} \\ T|_{\pm h} = T_0. & (5) \end{cases}$$

Here q_v is the source function determined by formula (1), α is the coefficient of heat transfer, and T_0 is the ambient temperature. The solutions of Eq. (3) with boundary conditions (4) or (5) of types III or I, respectively, correspond to the stationary states of the system.

As is well known [6], the loss factor $\varepsilon''(T)$ in some polar dielectrics is satisfactorily described by the Kirkwood formula

$$\varepsilon''(T) = \frac{2\varepsilon''_{\max}}{(\omega\tau_r)^{\beta_d} + (\omega\tau_r)^{-\beta_d}} = \varepsilon''_{\max}\operatorname{scosh}[\beta_d \ln(\omega\tau_r)], \quad (6)$$

where ω is the frequency of the applied electric field E, $\tau_r = \tau_0\exp(W/kT)$ is the relaxation time, β_d is the distribution parameter, and W is the activation energy. A significant nonlinearity of $\varepsilon''(T)$ allows us to ignore the much weaker temperature dependences of λ and α. Expanding the term $\exp(W/kT)$ in Eq. (6) and taking into account the asymptotic behavior of $\operatorname{scosh}[\beta_d\ln(\omega\tau_r)]$ in the region of T_g (a maximum in $\varepsilon''(T)$), we obtain the following expression:

$$\begin{aligned} \varepsilon''(T) &= \varepsilon''_{\max}\exp[-(\beta_d W/kT_g^2)|T - T_g|] \\ &\times [2 - \exp[(-(\beta_d W/kT_g^2)|T - T_g|]. \end{aligned} \quad (7)$$

Introducing the dimensionless load

$$\beta = \frac{\omega\varepsilon_0\varepsilon''_{\max}(E2h)^2}{\lambda}\frac{\beta_d W}{kT_g^2}, \quad (8)$$

dimensionless temperature

$$\vartheta = \frac{T - T_g}{kT_g^2}\beta_d W, \quad (9)$$

the Biot number

$$\mathrm{Bi} = \frac{\alpha h}{\lambda}, \quad (10)$$

and dimensionless coordinate

$$y = \frac{x}{h}, \quad (11)$$

the system (3)–(5) can be reduced to the following form:

$$\begin{cases} \dfrac{d^2\vartheta}{dy^2} + \beta\exp(-|\vartheta|)(2 - \exp - |\vartheta|) = 0, & (12) \\ \left.\dfrac{d\vartheta}{dy}\right|_0 = 0 \quad \left.\dfrac{d\vartheta}{dy}\right|_{\pm 1} = \mp\mathrm{Bi}(\vartheta|_{\pm 1} - V_0), & (13) \\ \left.\dfrac{d\vartheta}{dy}\right|_0 = 0 \quad \vartheta|_{\pm 1} = V_0, & (14) \end{cases}$$

where Eqs. (13) and (14) are the boundary conditions of types III and I, respectively. The form of a model source $q_v(T)$ determined with allowance for (7) at $\beta = \varepsilon_{\max}$ is depicted in Fig. 1. In system (12)–(14), the solution $\vartheta \le 0$ corresponds to the temperature states on the left of T_g ($T \le T_g$), while the solution $\vartheta \ge 0$ refers to the region $T \ge T_g$; V_0 is the dimensionless temperature of the dielectric surface. Thus, the solution $\vartheta(x)$ to equation (12) with boundary conditions of type I depends on two parameters, the load β and the dielectric surface temperature V_0: $\vartheta = \vartheta(x, \beta, V_0)$. A solution to the same problem with boundary conditions of type III depends on an additional dimensionless parameter Bi.

3. Solving model equations. System (12)–(14) can be integrated, and the exact solution can be written for the boundary conditions of both types. Let us consider a solution describing the temperature field $\vartheta(x)$ for the boundary conditions of type I.

3.1. $V_0 \le \vartheta < \vartheta_m \le 0$. In this case,

$$\vartheta(x) = \ln\frac{4 - a^2}{2 + a\cosh(y\sqrt{\beta}\sqrt{4 - a^2})}. \quad (15)$$

3.2. $V_0 \le 0$, $\vartheta_m \ge 0$, $\vartheta(x) \le 0$. [For $\vartheta(x) \ge 0$, the solution corresponds to Eq. (19).]. For $\vartheta_m \le -\ln(2 - \sqrt{2})$,

$$\begin{aligned} \vartheta(x) &= \ln\frac{4 - c^2}{2 + c\cosh Y}, \\ Y &= \left((y\sqrt{\beta} - A)\sqrt{4 - c^2}\right) - \ln B. \end{aligned} \quad (16)$$

For $\vartheta_m \ge -\ln(2 - \sqrt{2})$,

$$\vartheta(x) = \ln\frac{4 + c^2}{2 + c\sinh Y}. \quad (17)$$

In both cases, the constants A and B are expressed as

$$\begin{aligned} A &= \frac{1}{\sqrt{4 - b^2}}\arccos\frac{2 - b^2}{b}, \\ B &= \frac{c}{\sqrt{4 \mp c^2}\sqrt{1 \mp c^2} + 2 \mp c^2}, \end{aligned} \quad (18)$$

where the minus and plus signs under the square roots refer to Eqs. (16) and (17), respectively.

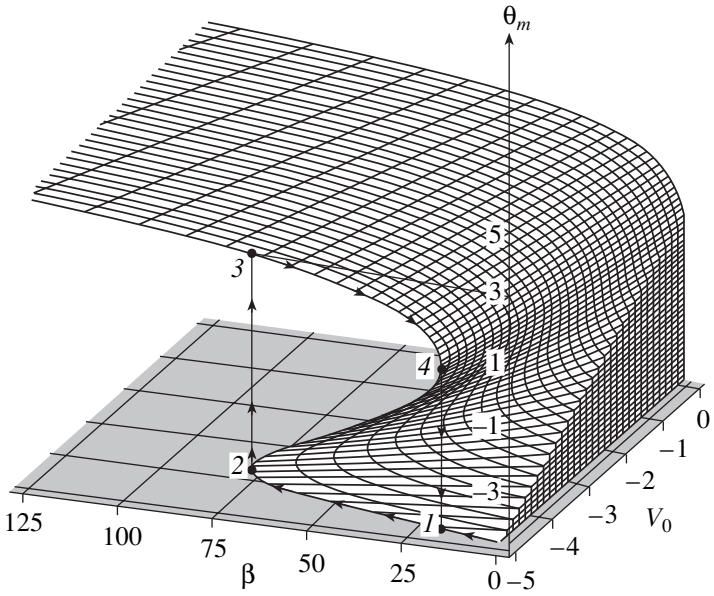

Fig. 2. The temperature ϑ_m at the center of the dielectric layer plotted in the space of parameters (β, V_0) for $V_0^* = -5$.

3.3. $V_0 \geq 0$. In this case,

$$\vartheta(x) = \ln\frac{2 + b\cos(y\sqrt{\beta}\sqrt{4-b^2})}{4-b^2}. \qquad (19)$$

In all expressions (15)–(19), the coefficients are

$$\begin{cases} a = 2 - \exp(\vartheta_m), \\ b = 2 - \exp(-\vartheta_m), \\ c^2 = |b^2 - 2|. \end{cases}$$

where ϑ_m is the maximum dimensionless temperature (at the center of the dielectric layer). The condition

$$\sqrt{\beta} = \int_{V_0}^{\vartheta_m} \frac{d\vartheta}{\sqrt{\int_{\vartheta}^{\vartheta_m} q_v(U)dU}}$$

gives an implicit dependence $\vartheta_m = f(\beta, V_0)$.

4. Discussion of results. In the most interesting case of $V_0 < 0$, $\vartheta_m > 0$, corresponding to the distribution $T(x)$ in the interval containing the region of maximum $\varepsilon''(T)$ in the vicinity of T_g (section 3.2), the solution is

$$\sqrt{\beta} = \frac{1}{\sqrt{4-b^2}}\arccos\frac{2-b^2}{b} - \frac{1}{\sqrt{2+b^2}} \times \ln\left(\frac{(\sqrt{2+b^2}\sqrt{b^2-1}+b^2)\exp(V_0)}{\sqrt{2+b^2}\sqrt{(2-\exp(V_0))^2+b^2-2}+2+b^2-2\exp(V_0)}\right). \qquad (20)$$

Figure 2 shows the shape of the surface $\vartheta_m = \vartheta_m(\beta, V_0)$ representing a multivalued function of the parameters. Consider a ϑ_m cross section corresponding to a fixed temperature V_0^* of the dielectric surface. The ascending ϑ_m branches correspond to the stable temperature states of the system, while the descending branch represents unstable states. As the load is gradually increased (e.g., by increasing the applied voltage $U = E2h$, the system passes from state 1 to 2 and then exhibits a jump to state 3. A subsequent decrease in the load is accompanied by the passage from state 4 to 3 and drops to state 1.

In this case, the system exhibits a hysteresis that was experimentally observed when studying the performance of PET capacitors under the conditions of large reactive powers ωcU^2. The multivaluedness of ϑ_m vanishes for $V_0 \geq 0$ ($T_0 \geq T_g$). According to the catastrophe theory, the $\vartheta_m(\beta, V_0)$ surface possess a characteristic singularity of the "fold" (A_3) type [7].

An analysis of the interesting problems of dynamics of the transitions between states 1–2–3–4 falls outside the framework of this publication.

Conclusions. 1. Using an approach based on the Kirkwood relationship describing the variation of the

loss factor $\varepsilon''(T)$ for a broad class of polar dielectrics, exact solutions to a nonlinear model problem of the thermal stability of such dielectrics in a variable electric field were obtained.

2. For certain values of the problem parameters (the temperature V_0 of a plane capacitor surface and the load β), the system is characterized by a multiplicity of the stationary temperature states.

3. In the space of parameters (β, V_0), the temperature ϑ_m at the center of the dielectric layer is described by a multivalued surface possessing a topological singularity of the "fold" type.

REFERENCES

1. E. V. Kharitonov and É. I. Ermolina, Zh. Tekh. Fiz. **55** (7), 1279 (1985) [Sov. Phys. Tech. Phys. **30**, 740 (1985)].
2. E. V. Kharitonov and É. I. Ermolina, Fiz. Tverd. Tela (Leningrad) **29** (4), 977 (1987) [Sov. Phys. Solid State **29**, 560 (1987)].
3. A. A. Samarskiĭ, V. A. Galaktionov, S. P. Kurdyumov, and A. P. Mikhaĭlov, *Operations with Sharpening in Problems for Quasilinear Parabolic Equations* (Nauka, Moscow, 1987).
4. P. N. Bondarenko, O. A. Emel'yanov, and S. N. Koĭkov, Pis'ma Zh. Tekh. Fiz. **15** (16), 45 (1989) [Sov. Tech. Phys. Lett. **15**, 640 (1989)].
5. B. S. Kerner and V. V. Osipov, Usp. Fiz. Nauk **160** (9), 1 (1990) [Sov. Phys. Usp. **33**, 679 (1990)].
6. B. I. Sazhin, *Electrical Properties of Polymers* (Khimiya, Leningrad, 1986).
7. V. I. Arnol'd, *Catastrophe Theory* (Nauka, Moscow, 1990), p. 128.

Translated by P. Pozdeev

Technical Physics Letters, Vol. 27, No. 8, 2001, pp. 683–685. Translated from Pis'ma v Zhurnal Tekhnicheskoĭ Fiziki, Vol. 27, No. 16, 2001, pp. 40–46.

A Phenomenological Parameter Characterizing the Relaxation of Stresses Caused by the Lattice Mismatch at a Heteroboundary

O. V. Konstantinov, E. Yu. Kotel'nikov, A. V. Matveentsev, and A. E. Romanov

Ioffe Physicotechnical Institute, Russian Academy of Sciences, St. Petersburg, 194021 Russia

Received March 7, 2001

Abstract—An analytical formula is derived describing an increase in the bandgap width for a quantum cluster considered as an inclusion of the simplest shape (spherical or flat) featuring an arbitrary lattice mismatch with the surrounding matrix. A phenomenological relationship is introduced between this quantity and the stressed boundary relaxation parameter considered as the fitting parameter. The relaxation is small (or even absent) in a system with quantum wells and is completely manifested in a system with quantum dots. © *2001 MAIK "Nauka/Interperiodica".*

Deformations are known to lead to significant changes in the energy spectra of semiconductors, in particular, to an increase in the bandgap width. This effect is related predominantly to the dilatation phenomenon (a strain-induced change in the crystal volume). The dilatation is related to the pressure equal to one-third of the stress tensor trace. The dependence of the bandgap width on the pressure is thoroughly studied in the physics of semiconductors [1]. This phenomenon becomes especially important in the theory of quantum clusters in semiconductors, such as quantum wells and quantum dots. Because of a lattice mismatch between the cluster and the surrounding matrix, the pressure inside the cluster may be rather large so as to significantly influence the spectrum of levels in the cluster.

The problems related to the calculation of the elastic stress fields at the quantum dots were considered in [2, 3]. Despite the highly sophisticated methods employed, the results of those calculations were rather ambiguous. This is related to the fact that the lattice mismatch at the cluster boundaries is set by assuming that no stress field relaxation takes place at these boundaries. This assumption disagrees with the observed spectrum of recombination radiation from InAs quantum dots occurring in the GaAs matrix.

Below we propose a new method based on introducing a phenomenological parameter describing the stress field relaxation at the cluster boundaries. Is is believed, in combination with a simple cluster model also described in this paper and a simple theory of the spectrum of electron states developed previously [4], that this parameter ensures the determination of the stress field relaxation parameter at the cluster boundary using the spectrum of recombination radiation from the clusters.

Pressure inside a cluster. Quantum wells containing a narrow-bandgap material are usually characterized by the lattice constant of the virtual crystal exceeding that of the surrounding matrix. For this reason, the quantum well material is contracted. The contraction must be especially strong in the case of quantum dots, which are frequently composed of pure narrow-bandgap materials. In such a system, the difference Δa between the lattice constants of cluster and matrix is maximum. The contraction leads to an increase in the bandgap width of the cluster (quantum well or quantum dot) due to a pressure developed inside the cluster. According to the known experimental data summarized in [1], the dependence of the bandgap width on the pressure in most of the $A^{III}B^{V}$ semiconductors is described by increasing function. For the pressures below 20 kbar, the slope K of this increase is

$$K = 12 \text{ meV/kbar}. \quad (1)$$

If the pressure p is expressed in GPa, the relationship between the bandgap width and pressure can be written as

$$\delta E_g = 0.12p, \text{ eV}, \quad (2)$$

where δE_g is the pressure-induced bandgap increment (in eV). As will be demonstrated below (for both the spherical geometry of a quantum dot and the planar geometry of a quantum well), the pressure in both systems can be described by the same function of the relative effective lattice mismatch parameter f:

$$p = \frac{2}{3}\frac{E}{1-\nu}f, \quad (3)$$

where E is the Young modulus (GPa) and ν is the Poisson coefficient. Substituting formula (3) into relationship (2), we obtain an expression relating the increase in the bandgap width to the lattice mismatch parameter:

$$\delta E_g = 0.08\frac{E}{1-\nu}f, \text{ eV}. \quad (4)$$

Let us introduce a new phenomenological quantity ρ called the relaxation parameter. For this purpose, the

lattice mismatch parameter f can be presented in the following form:

$$f = \frac{\Delta a}{a} x(1-\rho), \quad (5)$$

where a is the lattice constant of the matrix, Δa is the difference between the lattice constants of a pure narrow-bandgap cluster material and the matrix (since the lattice constant of a wide-bandgap matrix is usually smaller than that of the narrow-bandgap cluster, the latter exhibits contraction and, hence, Δa is positive), and x is the fraction of the pure narrow-bandgap material in the solid solution of the cluster material (quantum well or quantum dot). In the proposed approach, the parameter ρ describing the relaxation of the cluster–matrix heteroboundary is considered as an unknown variable quantity. If the boundary is stressed and contains no misfit dislocations, this relaxation parameter is $\rho = 0$. If the boundary is not stressed (i.e., relaxation takes place), we have $\rho = 1$ (here, the mismatch parameter f is zero).

For a cluster composed of the $In_xGa_{1-x}As$ solid solution, we obtain $\Delta a = 4 \times 10^{-9}$ cm and $a = 5.7 \times 10^{-8}$ cm, so that

$$\frac{\Delta a}{a} = 0.07. \quad (6)$$

In this case, the lattice mismatch parameter can be expressed as

$$f = 0.07x(1-\rho). \quad (7)$$

For semiconductors based on InAs, we may take $E = 50$ GPa and $\nu = 1/3$ [2]. Then formula (3) can be written as

$$p = 3.5x(1-\rho). \quad (8)$$

Substituting (8) into (4), we exclude the pressure and obtain a formula describing an increase in the bandgap width:

$$\delta E_g = 0.42x(1-\rho), \text{ eV}. \quad (9)$$

Let us consider the magnitude of the relaxation parameter ρ introduced for the cluster–matrix heteroboundary. In the case of a quantum well, the boundary is flat and the lattice mismatch is relatively small, so that we may naturally assume that the relaxation is absent and $\rho = 0$. In the case studied previously[4], we dealt with a quantum well of the composition $In_{0.2}Ga_{0.8}As$ ($x = 0.2$) for which $\delta E_g = 0.08$ eV. Here and below, all energies are calculated to within 0.01 eV, since a better accuracy cannot be reached because the relaxation parameter ρ is unknown. An increase in the bandgap width inside a quantum dot made of a pure InAs is five times greater than the above value, reaching 0.40 eV (this value even exceeds the initial bandgap width equal to 0.35 eV). No electron levels would exist in such a quantum dot, which contradicts the experiment. From this we infer that the boundary of a cluster of the quantum dot type does not feature a pseudomorphous (i.e., stressed and dislocation-free) state. This is probably related to the conditions of growth of an InAs quantum dot pyramid arranged with its wide base on the InAs wetting layer. As the wetting layer is overgrown with gallium arsenide, the InAs pyramids are gradually "flooded" with GaAs. Under these conditions, we may naturally expect that no stretched GaAs crystal would form surrounding the InAs pyramid. Note that we cannot strictly prove the condition $f = 0$ for this cluster boundary and only make the simplest assumption. Therefore, these calculations possess mostly an illustrative character and the numerical values are by no means unambiguous. However, the proposed theory is quite simple and the calculations can be refined as soon as new experimental data appears to provide for a more reasonable selection of the relaxation parameter.

A final result for the bandgap width inside the cluster is given by formula (10) together with an empirical expression describing the bandgap width E_g^x for an unbounded solid solution. For example, such an expression for $In_xGa_{1-x}As$ is as follows [5]:

$$E_g^x = 1.43 - 1.48x + 0.41x^2. \quad (10)$$

The corresponding formula for the bandgap width inside the cluster is

$$E_g = 1.43 - 1.06x - 0.42x\rho + 0.41x^2. \quad (11)$$

Let us compare the result of E_g calculations by this formula for a quantum dot ($E_g = 1.23$ eV) to the value adopted previously ($E_g = 1.21$ eV) [4]. Of course, we may simply ignore a difference of 0.02 eV, but an attempt at eliminating this discrepancy using the relaxation parameter ρ yields $\rho = 0.25$, which is also quite a reasonable result.

Now we will consider the derivation of formula (3) for the pressure inside clusters of the simplest shapes (spherical and flat).

Elastic fields for a spherical quantum dot model. Let the crystal lattices of the quantum-confined structure and the surrounding matrix be characterized by the parameters a_1 and a_2, respectively. Within the framework of a linear theory, the elastic fields caused by the lattice mismatch $\Delta a = a_1 - a_2$ are proportional to the mismatch parameter: $f = \Delta a/a_1$.

A spherical quantum dot with a radius R_0 can be represented as an elastic dilatational conclusion. This system is modeled [7, 8] by an elastic ball of radius R_0 inserted into a spherical cavity having a volume smaller by ΔV than the inclusion volume. Owing to the symmetry, the field of displacements both inside ball ($\mathbf{u}^{(1)}$) and

outside ball ($\mathbf{u}^{(2)}$) possesses only a radial component depending on the radial coordinate r [7]:

$$u_r^{(1)} = -\frac{2(1-2\nu)}{(1+\nu)}\frac{C}{R_0^3}r, \tag{12}$$

$$u_r^{(2)} = \frac{C}{r^2}, \tag{13}$$

where ν is the Poisson coefficient. The elastic moduli of the quantum dot and the surrounding matrix are assumed to be equal. The constant C is determined from the boundary condition

$$4\pi R_0^2(u_r^{(2)} - u_r^{(1)})\Big|_{r=R_0} = \Delta V, \tag{14}$$

which yields

$$C = \frac{1+\nu}{12\pi(1-\nu)}\Delta V \quad \text{or} \quad C = \frac{1+\nu}{3(1-\nu)}R_0^3 f. \tag{15}$$

The second formula (13) takes into account that the volume difference ΔV can be related to the mismatch parameter as

$$\Delta V = 4\pi R_0^3 f, \quad \text{or} \quad \Delta V/V = 3f. \tag{16}$$

The field of displacements (11) and (12) determines the deformation tensor components (expressed in a spherical coordinate system):

$$\varepsilon_{rr}^{(1)} = \varepsilon_{\varphi\varphi}^{(1)} = \varepsilon_{\theta\theta}^{(1)} = -\frac{2(1-2\nu)}{3(1-\nu)}f, \tag{17}$$

$$\varepsilon_{rr}^{(2)} = -\frac{2(1+\nu)}{3(1-\nu)}\frac{R_0^3}{r^3}f, \quad \varepsilon_{\phi\phi} = \varepsilon_{\theta\theta} = \frac{1+\nu}{3(1-\nu)}\frac{R_0^3}{r^3}f. \tag{18}$$

The dilatation is defined as

$$\delta = \sum_k \varepsilon_{kk}.$$

This value is constant inside a quantum dot:

$$\delta^{(1)} = -\frac{2(1-2\nu)}{1-\nu}f, \tag{19}$$

and vanishes outside the dot:

$$\delta^{(2)} = 0. \tag{20}$$

Using Eqs. (17), (18), and Hooke's law, we obtain expressions for the elastic stress field:

$$\sigma_{rr}^{(1)} = \sigma_{\varphi\varphi}^{(1)} = \sigma_{\theta\theta}^{(1)} = -\frac{2E}{3(1-\nu)}f, \tag{21}$$

$$\sigma_{rr}^{(2)} = -\frac{2E}{3(1-\nu)}f; \quad \sigma_{\varphi\varphi}^{(2)} = \sigma_{\theta\theta}^{(2)} = -\frac{1}{2}\sigma_{rr}^{(2)}, \tag{22}$$

where E is the Young modulus. Accordingly, the pressure defined as

$$p = \frac{1}{3}\sum_k \sigma_{kk}$$

is given by formula (3) inside the quantum dot and is zero outside the dot.

Elastic fields for a flat quantum well model. Let us select a Cartesian coordinate system with the y axis perpendicular to the surfaces bounding the well. The axes x and z are parallel to the surfaces and to the crystallographic directions in which the mismatch f is set. The elastic deformations and stresses outside the well are absent, while those inside the well are determined by the relationships

$$\varepsilon_{xx} = \varepsilon_{zz} = -f, \quad \varepsilon_{yy} = \frac{2\nu}{1-\nu}f, \tag{23}$$

$$\sigma_{xx} = \sigma_{zz} = -\frac{E}{1-\nu}f, \quad \sigma_{yy} = 0. \tag{24}$$

Accordingly, the dilatation inside the well is

$$\delta = -\frac{2(1-2\nu)}{1-\nu}f. \tag{25}$$

Thus, we have proved that the pressure inside a contracted quantum well or quantum dot can be described by a common expression (3).

REFERENCES

1. R. A. Smith, *Semiconductors* (Cambridge Univ. Press, Cambridge, 1978; Mir, Moscow, 1982).
2. T. Benabbas, Y. Androussi, and A. Lefebvre, J. Appl. Phys. **86** (4), 1945 (1999).
3. A. D. Andreev, J. R. Downes, D. A. Faux, and E. P. O'Reily, J. Appl. Phys. **86** (1), 297 (1999).
4. V. P. Evtikhiev, O. V. Konstantinov, and A. V. Matveentsev, Pis'ma Zh. Tekh. Fiz. **27** (6), 65 (2001) [Tech. Phys. Lett. **27**, 248 (2001)].
5. *Landolt-Börnstein: Numerical Data and Functional Relationships in Science and Technology, New Series* (Springer-Verlag, Berlin, 1987), Group III, Vol. 22a.
6. J. D. Eshelby, Solid State Phys. **3**, 79 (1956).
7. C. Teodosiu, *Elastic Models of Crystal Defects* (Springer-Verlag, Berlin, 1982; Mir, Moscow, 1985).

Translated by P. Pozdeev

Technical Physics Letters, Vol. 27, No. 8, 2001, pp. 686–688. Translated from Pis'ma v Zhurnal Tekhnicheskoĭ Fiziki, Vol. 27, No. 16, 2001, pp. 47–53.

A Low-Radioactive D–^{3}He Thermonuclear Fuel Cycle with ^{3}He Self-Supply

V. I. Khvesyuk and A. Yu. Chirkov

Moscow State Technical University, Moscow, Russia

e-mail: khves@power.bmstu.ru

Received December 26, 2000

Abstract—The possibility of implementing a highly efficient low-radioactive thermonuclear fuel cycle using deuterium as the raw material (primary fuel) is justified. The energy production is ensured mostly by the D–^{3}He reaction, with ^{3}He obtained in the course of the reactor operation. It is shown that, under certain conditions, neutrons account for only ~5% of the total thermonuclear output power and the neutron power flux to the first wall is $q_n < 0.5$ MW/m^2. © *2001 MAIK "Nauka/Interperiodica".*

A mixture of deuterium D and light helium ^{3}He is one of the most promising alternative types of thermonuclear fuel. An attractive feature of the nearly equicomponent D–^{3}He mixture is the possibility of creating a low-radioactive thermonuclear reactor with a first wall lifetime exceeding 40 years, which is due to a low neutron power flux to the wall ($q_n < 0.5$ MW/m^2). A serious problem encountered in the realization of the equicomponent D–^{3}He fuel cycle is related to the fact that no commercially significant source of the ^{3}He isotope is available on the Earth. One of the possible solutions is the delivery of ^{3}He from the Moon [1].

Below we will consider alternative variants in which the primary fuel (raw material) is deuterium—a comparatively cheap and readily available isotope, while ^{3}He is produced and employed in the same reactor. Preliminary kinetic analysis showed that a high efficacy can be reached using both a D–^{3}He cycle [2–4] and a catalyzed D–D cycle [4]. The purpose of this study was to consider the possible variants of the D–^{3}He cycle with ^{3}He self-supply and to estimate the parameters of a thermonuclear plasma and a magnetic plasma confinement system ensuring the low radioactivity and high efficiency of the energy production.

A deuterium-containing plasma features the following simultaneous reactions:

$$\mathrm{D + D} \longrightarrow n(2.45\ \mathrm{MeV}) + {}^3\mathrm{He}(0.817\ \mathrm{MeV}), \quad (1)$$

$$\mathrm{D + D} \longrightarrow p(3.02\ \mathrm{MeV}) + \mathrm{T}(1.01\ \mathrm{MeV}), \quad (2)$$

$$\mathrm{D} + {}^3\mathrm{He} \longrightarrow p(14.68\ \mathrm{MeV}) + {}^4\mathrm{He}(3.67\ \mathrm{MeV}), \quad (3)$$

$$\mathrm{D + T} \longrightarrow n(14.1\ \mathrm{MeV}) + {}^4\mathrm{He}(3.5\ \mathrm{MeV}). \quad (4)$$

Owing to a high rate of reaction (4), a considerable proportion of the tritium produced by reaction (2) interacts with deuterium. The parameters of fuel cycles based on the deuterium reactions (1)–(4) depend to a significant extent on the ratio of fuel components

$$r_j = n_j/n_\mathrm{D}, \quad (5)$$

where $j = {}^3$He or T. Figure 1 shows a plot of the ignition (break-even) criterion $n\tau T$ versus the relative amount of ^{3}He. The optimum values of the plasma temperature fall within the range $T = 50$–70 keV. Figure 1 is plotted for $T = T_\mathrm{min}$, which is the temperature corresponding to the minimum $n\tau T$ value for a given $r_{^3\mathrm{He}}$. The ignition criterion was calculated using the reaction cross sections taken from data base [5] and the bremsstrahlung losses calculated by formulas [4] taking into account the quantum and relativistic effects.

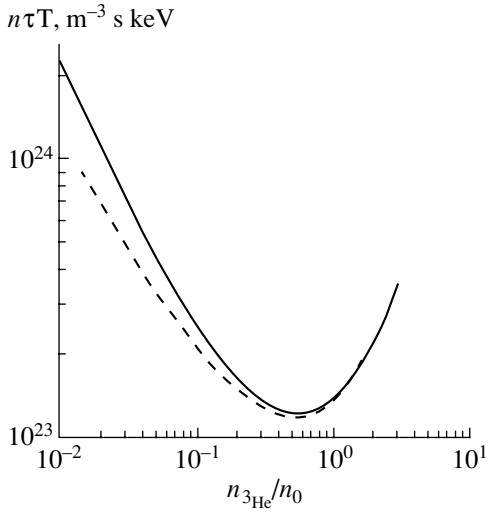

Fig. 1. Plots of the ignition criterion $n\tau T$ versus relative content of ^{3}He in the cycle at $T = T_\mathrm{min}$ for $\gamma_\mathrm{T} = 0$ (solid curve) and 1 (dashed cure).

1063-7850/01/2708-0686$21.00 © 2001 MAIK "Nauka/Interperiodica"

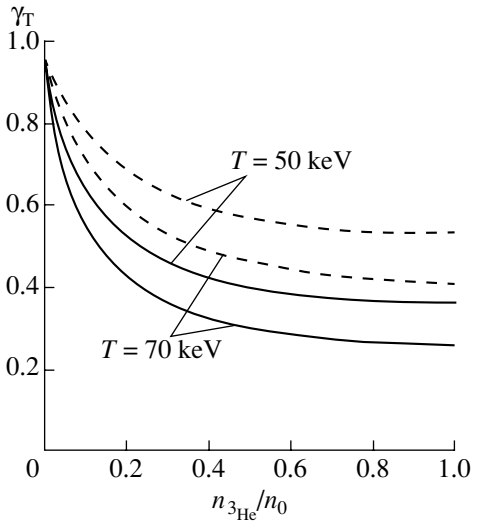

Fig. 2. Plots of the tritium burn-up fraction versus relative content of ^{3}He in the cycle at two temperatures for the tritium confinement time $\tau_T = \tau_{ign}$ (solid curves) and $2\tau_{ign}$ (dashed curves), where τ_{ign} is the time corresponding to the ignition criterion $n\tau T$.

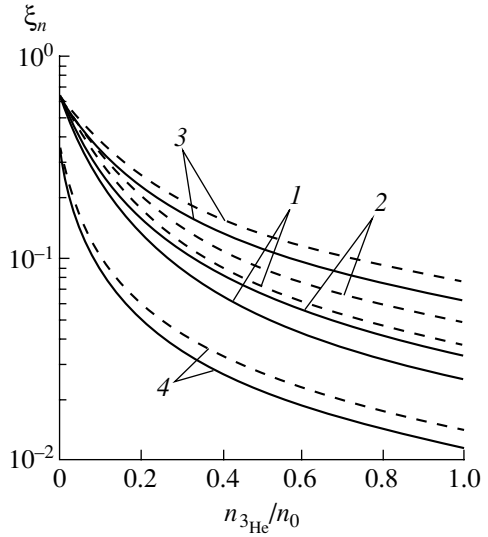

Fig. 3. Plots of the neutron yield versus relative content of ^{3}He in the cycle at T = 70 keV (solid curves) and 50 keV (dashed curves: (*1*) $\tau_T = \tau_{ign}$; (*2*) $\tau_T = 2\tau_{ign}$; (*3*) total tritium burn-up; (*4*) total tritium pump-off.

The tritium burn-up in the plasma is characterized by the quantity γ_T equal to the ratio of the number of tritium nuclei burning per unit time to the number of these nuclei produced during the same time. In a low-radioactivity thermonuclear reactor, the relative neutron yield $\xi_n = P_n/P_{fus}$ (P_{fus} is the fusion power and P_n is the neutron flux power) must be on a level of ~0.1. In order to reduce the flux of neutrons with an energy of 14.1 MeV, it is necessary to ensure the forced removal of tritium from the plasma. This can be achieved, for example, by the so-called selective pumping [6], which also removes some other products of reactions (1)–(4) including p, ^{3}He, and ^{4}He.

Figures 2 and 3 show the tritium burn-up fraction γ_T and the neutron yield ξ_n, respectively. In order to provide for ξ_n = 0.1–0.15, it is necessary that the relative fraction of ^{3}He would be $r_{^3He} \sim 0.2$. In a reactor using only the natural deuterium fuel and intended for the ^{3}He production, the possible sources of ^{3}He are reaction (1) and reaction T $\longrightarrow$ ^{3}He + e + 0.018 MeV. In the latter case, tritium can be provided either by reaction (2) or by a reaction in the blanket: n + ^{6}Li $\longrightarrow$ T + ^{4}He + 4.8 MeV; n + ^{7}Li $\longrightarrow$ T + ^{4}He + n – 2.47 MeV (with an allowance for the neutron multiplication n + ^{9}Be $\longrightarrow$ 2^{4}He + 2n – 1.67 MeV. Theoretically, the use of the neutron-multiplier materials may provide for $K_{D–D} \approx K_{D–T} > 2$, where $K_{D–D}$ ($K_{D–T}$) is the number of tritium nuclei produced in the blanket per one D–D (D–T) neutron generated in the plasma. In the case under consideration, $r_{^3He}$ = 0.1–0.2 and $T_{min} \approx 70$ keV.

As is known, an increase in the plasma temperature leads to a sharp growth in the cyclotron losses. For this reason, the minimum time τ_E required for the energy confinement in a field with low β (the ratio of plasma pressure to the magnetic field pressure) corresponds to lower temperatures. On the other hand, the region of T < 50 keV is characterized by a sharp increase in the $n\tau T$ value. Thus, the working temperature range occurs in the region T = 50–70 keV. The power of cyclotron losses P_s depends on a number of factors and can be estimated by the Trubnikov formula [7]. In order to reduce the cyclotron losses and to decrease the effect of errors related to their determination on the final results, the magnetic system parameters should be selected so that the ratio $\xi_s = P_s/P_{fus}$ does not exceed ~0.2. The values of thermonuclear plasma parameters for the reactors with magnetic plasma confinement are summarized in the table for the systems with relatively small and large β.

The numerical analysis was performed for the plasma with a circular cross section (no special magnetic configuration features were taken into account). The plasma temperature was assumed to be constant in the plasma column cross section, while the pressure was distributed according to a parabolic law $p = p_0[1 – (\rho/R)^2]$ (ρ is the distance from the magnetic axis and R is the plasma column radius). The initial set of parameters includes thermonuclear power on the axis $P_{fus\,0}$, column radius R, corpuscular time τ_a of retaining the thermonuclear products, plasma power gain coefficient Q, average pressure ratio $\langle\beta\rangle$, the electron and ion temperatures ($T_e = T_i = T$), the coefficient Γ_s of the cyclotron radiation reflection from the wall, and the coefficients of tritium production in the plasma ($K_{D–D}$ and $K_{D–T}$). The calculations yielded $r_{^3He}$, r_T, γ_T, τ_E, ξ_n, ξ_{br} =

Thermonuclear D–^{3}He plasma parameters in reactors with magnetic confinement system (P_{fus0} = 6 MW/m^3, R = 2m, τ_a = 8 s, Q = 20)

Variant	$\langle\beta\rangle$ = 0.1, T = 50 keV, Γ_s = 0.9		$\langle\beta\rangle$ = 0.5, T = 70 keV, Γ_s = 0.7			
	1	2	3	4	5	6
$K_{D–D} = K_{D–T}$	–	1	1	0	0	1
$r_{^3He}$	0.5*	0.305	0.245	0.125	0.158	0.245
r_T	0.00356	0.00381	0.00524	0.00572	$<10^{-3}$**	$<10^{-3}$**
γ_T	0.64	0.68	0.64	0.70	–	–
n_{D0}, 10^{20} m^{-3}	2.55	3.11	2.51	3.27	3.26	2.70
$n_{tot\,0}$, 10^{20} m^{-3}	9.72	9.87	7.68	8.38	8.06	7.38
B_0, T	10.7	10.7	5.4	5.4	5.4	5.3
τ_E, s	7.6	7.9	5.3	7.5	4.9	4.2
ξ_n	0.10	0.15	0.15	0.27	0.061	0.042
ξ_{br}	0.36	0.32	0.24	0.25	0.23	0.22
ξ_s	0.21	0.21	0.061	0.065	0.064	0.059
q_n, MW/m^2	0.20	0.30	0.30	0.53	0.12	0.08

* Requires external ^{3}He sources.

** Selective pumping must provide for the complete absence of tritium nuclei with energies <350 keV.

P_{br}/P_{fus} (P_{br} is the bremsstrahlung radiation power), ξ_s, and q_n, as well as the parameters on the magnetic axis including deuterium concentration (n_{D0}), total plasma density ($n_{tot\,0}$), and the magnetic induction in vacuum B_0.

In the table, the base variant with $r_{^3He}$ = 0.5 corresponds to a minimum required plasma confinement time; for variants 2–6, the $r_{^3He}$ values correspond to a stationary operation of the reactor with equal burn-up times for all ^{3}He production schemes. In the variants with pumping (5 and 6), it was assumed that the concentration of thermalized tritium is zero and the concentration of high-energy tritium ($\varepsilon > \varepsilon_{pump}$, where ε is the kinetic energy and ε_{pump} is the pumping energy) was calculated using a high-energy distribution function [8]. The energy losses from plasma (related to pumping of the thermonuclear products at $\varepsilon_{pump} \approx 350$ keV) amounted to about 10% of the P_{fus}. Note that the D–^{3}He cycle is rather sensitive with respect to contamination with impurities entering the plasma as a result of the first wall sputtering. For example, the lethal contents of B^{+5} and Be^{+4} for $r_{^3He}$ = 0.15–1 and T = 50–70 keV are 1–2% and 2–3%.

The results of calculations presented in the table show that, for some reasons (e.g., the necessity of simultaneously obtaining high B_0 and Γ_s values), the systems with low Be^{+4} (including traditional tokamaks) are inexpedient in D–^{3}He reactors. Thus, high β values (characteristic of the alternative magnetic systems such as spherical tokamak and reversed magnetic configuration) are of principal importance for the D–^{3}He reactor under consideration. Meeting this condition is necessary to provide for a sufficiently high average specific thermonuclear power ($\langle P_{fus}\rangle \approx 2$ MW/m^3), acceptable magnetic field strength ($B_0 \approx 5$ T), and the required confinement time ($\tau_E < 10$ s). By means of selective pumping, it is possible to ensure a very low neutron yield at a small $r_{^3He}$ in a blanket-free reactor ($K_{D–D} = K_{D–T} = 0$).

REFERENCES

1. L. M. Wittenberg, J. F. Santarius, and G. L. Kulcinski, Fusion Technol. **10**, 165 (1986).
2. I. N. Golovin, V. V. Kostenko, V. I. Khvesyuk, and N. V. Shabrov, Pis'ma Zh. Tekh. Fiz. **14** (20), 1860 (1988) [Sov. Tech. Phys. Lett. **14**, 807 (1988)].
3. V. I. Khvesyuk, N. V. Shabrov, D. V. Semenov, and A. N. Lyakhov, Zh. Tekh. Fiz. **68** (7), 37 (1998) [Tech. Phys. **43**, 777 (1998)].
4. V. I. Khvesyuk and A. Yu. Chirkov, Pis'ma Zh. Tekh. Fiz. **26** (21), 61 (2000) [Tech. Phys. Lett. **26**, 964 (2000)].
5. R. Feldbaher, *Nuclear Reaction Cross Sections and Reactivity Parameter* (IAEA, 1987).
6. V. I. Khvesyuk and N. V. Shabrov, Pis'ma Zh. Tekh. Fiz. **19** (1), 42 (1993) [Tech. Phys. Lett. **19**, 17 (1993)].
7. B. A. Trubnikov, in *Reviews of Plasma Physics*, Ed. by M. A. Leontovich (Atomizdat, Moscow, 1973; Consultants Bureau, New York, 1979), Vol. 7.
8. S. V. Putvinskii, in *Reviews of Plasma Physics*, Ed. by B. B. Kadomtsev (Énergoizdat, Moscow, 1990; Consultants Bureau, New York, 1993), Vol. 18.

Translated by P. Pozdeev

Technical Physics Letters, Vol. 27, No. 8, 2001, pp. 689–691. Translated from Pis'ma v Zhurnal Tekhnicheskoĭ Fiziki, Vol. 27, No. 16, 2001, pp. 54–58.

A Nonlinear Dispersion Relationship for Electrocapillary Waves on the Charged Surface of a Dielectric Liquid

N. M. Zubarev

Institute of Electrophysics, Ural Division, Russian Academy of Sciences, Yekaterinburg, Russia

e-mail: nick@ami.uran.ru

Received February 5, 2001

Abstract—It is shown that the problem of describing a profile of a progressive electrocapillary wave on the boundary of a dielectric liquid, with a free surface charge completely screening the electric field above the liquid, admits an analytical solution. An exact expression for the nonlinear dispersion relationship between the frequency, wavenumber, and amplitude of such a wave is derived and analyzed. *© 2001 MAIK "Nauka/Interperiodica".*

A dispersion relationship for an electrocapillary wave on the boundary of a deep dielectric liquid bearing a free surface charge has the following form [1, 2]:

$$\omega_0^2(k) = \frac{\alpha}{\rho}k^3 - \frac{P}{4\pi\rho}k^2, \quad P = E^2 + E'^2, \qquad (1)$$

where E and E' are the electric field strengths in and above the liquid, respectively; α is the surface tension coefficient; ρ is the liquid density; k is the wavenumber; and ω_0 is the frequency. Expression (1) ignores effects of the gravity force, which is possible provided that $P \gg 8\pi\sqrt{g\alpha\rho}$ and $k \gg 4\pi\rho g/P$ (g is the acceleration of gravity).

An approach to the study of the evolution of a charged liquid surface based on the analysis of Eq. (1) is only applicable in the case of small-amplitude perturbations of the boundary ($A \ll k^{-1}$). For the surface waves with a finite amplitude, the main nonlinear effect consists in that the dispersion relationship depends on the amplitude A (see, e.g., [3]:

$$\omega = \omega(k, A).$$

Below we demonstrate that, in the case when the surface charge completely screens the electric field above the liquid boundary (i.e., when $E' = 0$) [4, 5], the problem of describing a profile of the nonlinear electrocapillary wave on the dielectric liquid surface admits an analytical solution. This allows us to obtain an exact expression for the nonlinear dispersion equation and to analyze this relationship.

Let us consider a potential motion of the ideal dielectric liquid in a region bounded by a free surface $y = \eta(x, t)$. The electric field potential in the medium $\varphi(x, y, t)$ and the liquid velocity potential $\Phi(x, y, t)$ obey the Laplace equations

$$\varphi_{xx} + \varphi_{yy} = 0, \quad \Phi_{xx} + \Phi_{yy} = 0. \qquad (2)$$

System (2) has to be solved together with the kinematic and dynamic boundary conditions

$$\eta_t = \Phi_y - \eta_x\Phi_x, \quad y = \eta(x, t), \qquad (3)$$

$$\Phi_t + \frac{\Phi_x^2 + \Phi_y^2}{2} + \frac{\varphi_x^2 + \varphi_y^2 - E^2}{8\pi\rho} = \frac{\alpha\eta_{xx}}{\rho(1 + \eta_x^2)^{3/2}}, \qquad (4)$$
$$y = \eta(x, t);$$

the condition of equipotentiality of the liquid surface in the presence of a free surface charge,

$$\varphi = 0, \quad y = \eta(x, t); \qquad (5)$$

and the conditions of the electric field homogeneity and the velocity field damping at infinite distance from the surface

$$\varphi \longrightarrow -Ey, \quad \Phi \longrightarrow 0, \quad y \longrightarrow -\infty. \qquad (6)$$

A system of equations describing a progressive electrocapillary wave (with the profile remaining unchanged in the frame of reference related to the wave) are obtained from the electrohydrodynamic equations (2)–(6) upon the following substitution:

$$\varphi(x, y, t) = \varphi(x', y), \quad \Phi(x, y, t) = \Phi'(x', y) + Cx',$$
$$\eta(x, t) = \eta(x'),$$

where $x' = x - Ct$ and C is a constant having the sense of the wave velocity along the x axis. It is convenient to introduce a current function $\Psi(x', y)$ harmonically conjugated with the potential Φ':

$$\Psi_{x'} = -\Phi'_y, \quad \Psi_y = \Phi'_{x'},$$

this harmonic conjugate satisfies the Laplace equation

$$\Psi_{x'x'} + \Psi_{yy} = 0 \quad (7)$$

with the boundary conditions

$$\Psi = 0, \quad y = \eta(x'), \quad (8)$$

$$\Psi \longrightarrow -Cy, \quad y \longrightarrow -\infty. \quad (9)$$

As can be seen, Eqs. (7)–(9) coincide to within constant terms with Eqs. (2), (5), and (6) for the electric field potential. Consequently, there is a relationship between the field and velocity potentials

$$\varphi/E = \Psi/C.$$

Therefore, the wave shape in the moving coordinate system (x', y) is described by an equation derived from the boundary condition (4):

$$\frac{\Psi_{x'}^2 + \Psi_y^2 - C^2}{2} = \frac{\alpha'\eta_{x'x'}}{\rho(1 + \eta_{x'}^2)^{3/2}}, \quad y = \eta(x'), \quad (10)$$

where α' is the effective surface tension

$$\alpha' = \frac{4\pi\rho C^2}{E^2 + 4\pi\rho C^2}\alpha. \quad (11)$$

Equations (7)–(10) coincide with equations describing the shape of a progressive capillary wave [6] and, to within constant factors, with expressions for the equilibrium configuration of a charged surface of a liquid metal [7, 8]. This system of equations possesses a broad class of exact periodic solutions [6]. Using these solutions, we may describe the amplitude of the surface perturbations $A = \frac{1}{2}(\eta_{max} - \eta_{min})$ as a function of the wavenumber k, the wave velocity C, and the system parameters:

$$A = \left(\frac{4\alpha'^2}{C^4\rho^2} - \frac{4}{k^2}\right)^{1/2}.$$

Substituting formula (11) for the effective surface tension α' and assuming that $C = \omega/k$ (i.e., that C is the phase velocity of the wave), we obtain an exact expression for the nonlinear dispersion relationship

$$\omega^2(k, A) = \frac{\alpha k^3}{\rho\sqrt{1 + A^2k^2/4}} - \frac{E^2k^2}{4\pi\rho}. \quad (12)$$

As can be readily seen, in the limit of infinitely small amplitudes ($A \longrightarrow 0$) this expression transforms into a linear dispersion relationship (1). According to Eq. (1), the frequency is negative ($\omega_0^2 < 0$) for $k < k_0 = E^2/(4\pi\alpha)$; this implies that an aperiodic hydrodynamic instability is developed on the initially flat liquid surface. For $k > k_0$, the frequency ω_0 is imaginary; this corresponds to the propagation of linear dispersive waves. Now let us study how an allowance for the dependence on A (i.e., for the nonlinearity) affects the character of dynamics of the free charged surface of a dielectric liquid. It readily follows from (12) that a maximum wave amplitude at a fixed wavenumber $k > k_0$ corresponds to the wave with $\omega = 0$ and is equal to

$$A_{max}(k) = \left(\frac{64\pi^2\alpha^2}{E^4} - \frac{4}{k^2}\right)^{1/2}.$$

If the wave amplitude exceeds this level, then $\omega^2 < 0$ and the problem becomes ill-posed in the context of wave propagation. Moreover, this implies that the amplitude of the surface perturbations may infinitely increase with time, which corresponds to an explosion-like electrohydrodynamic instability.

The above condition generalizes the simplest linear criterion for the instability development on a flat liquid surface to the case of finite perturbation amplitude. Note also that, for any wavenumber, the maximum amplitude obeys the inequality $A_{max}(k) < 8\pi\alpha E^{-2}$. Therefore, Eqs. (2)–(6) admit the wave solutions only for $k > k_0$ and $A < 2/k_0$. Using Eq. (12), we may qualitatively analyze the stability of such solutions. For a relatively small amplitude, relationship (12) can be represented in the form of a series (Stokes' expansion)

$$\omega(k, A) = \omega_0(k) + \omega_2(k)A^2,$$

where ω_0 is determined by Eq. (1) and ω_2 s given by the formula

$$\omega_2(k) = -\frac{\alpha k^5}{16\omega_0(k)\rho}.$$

The criterion for the modulation instability of small-amplitude waves is as follows [3]: $\omega_0''\omega_2 < 0$, where $\omega'' = d^2\omega/dk^2$. As can be readily seen, the wave packet in our case is stable for $k_0 < k < 4k_0/3$ and unstable for $k > 4k_0/3$.

Thus, an analysis of the nonlinear dispersion relationship (12) led us to several conclusions concerning the stability of a charged surface of a dielectric liquid with respect to finite perturbations and the domain of existence of the wave solutions to the equations of electrodynamics. A more detailed analysis of the dynamics of perturbations on the liquid surface can be performed using a conformal mapping of the space occupied by the liquid onto a halfplane (see, e.g., [9]). In particular, neglecting the capillary effects, this method reduces the initial equations of motion (2)–(6) to an integrable equation describing the Laplace growth [10].

Acknowledgments. This study was supported in part by the Russian Foundation for Basic Research (project no. 00-02-17 428) and by the INTAS Foundation (project no. 99-1068).

REFERENCES

1. J. R. Melcher, *Field-coupled Surface Waves* (MIT Press, Cambridge, Mass., 1963).
2. L. P. Gor'kov and D. M. Chernikova, Dokl. Akad. Nauk SSSR **228** (4), 829 (1976) [Sov. Phys. Dokl. **21**, 328 (1976)].
3. G. B. Whitham, *Linear and Nonlinear Waves* (Wiley, New York, 1974; Mir, Moscow, 1977).
4. V. P. Volodin, M. S. Khaĭkin, and V. S. Édel'man, Pis'ma Zh. Éksp. Teor. Fiz. **26** (10), 707 (1977) [JETP Lett. **26**, 543 (1977)].
5. V. Shikin and P. Leĭderer, Fiz. Nizk. Temp. **23** (5/6), 624 (1997) [Low Temp. Phys. **23**, 468 (1997)].
6. G. D. Crapper, J. Fluid Mech. **2**, 532 (1957).
7. N. M. Zubarev, Pis'ma Zh. Tekh. Fiz. **25** (22), 79 (1999) [Tech. Phys. Lett. **25**, 920 (1999)].
8. N. M. Zubarev, Zh. Éksp. Teor. Fiz. **116** (6), 1990 (1999) [JETP **89**, 1078 (1999)].
9. A. I. Dyachenko, E. A. Kuznetsov, M. D. Spector, and V. E. Zakharov, Phys. Lett. A **221**, 73 (1996).
10. N. M. Zubarev, Pis'ma Zh. Éksp. Teor. Fiz. **71** (9), 534 (2000) [JETP Lett. **71**, 367 (2000)].

Translated by P. Pozdeev

Technical Physics Letters, Vol. 27, No. 8, 2001, pp. 692–694. Translated from Pis'ma v Zhurnal Tekhnicheskoĭ Fiziki, Vol. 27, No. 16, 2001, pp. 59–64.

A Possible Mechanism of "Superdeep" Particle Penetration into a Solid Target

A. A. Sivkov

High Voltage Research Institute, Tomsk Polytechnic University, Tomsk, Russia

e-mail: admin@admin.hvri.tpu.tdu.ru

Received March 19, 2001

Abstract—Experimental data obtained by the author demonstrate that particles may exhibit superdeep penetration into solid targets by a classical cumulative mechanism never considered previously. *© 2001 MAIK "Nauka/Interperiodica".*

Experiments on the deposition of titanium–titanium carbide (Ti–TiC) composite coatings onto steel substrates in a coaxial magneto-plasmatic accelerator [1, 2] showed the effect to be analogous to the so-called superdeep penetration of microparticles [3–6]. The composition was formed (in the course of the accelerator operation) due to the plasma-erosion sputtering of titanium from the surface of electrodes and the dynamic synthesis of titanium carbide. The necessary carbon was introduced in the form of a powder into the arc discharge initiation zone.

In a cylindrical accelerator channel with a diameter of 13 mm and a length of 280 mm, the front part of the high-current discharge plasma structure of the Z-pinch type was accelerated by a current pulse increasing up to 150 kA in 170 μs to a velocity of ~3.3 km/s. A steel target-substrate with a thickness of 10 mm and a diameter of 120 mm was placed at a distance of 400 mm from the channel edge. The experiments were performed at atmospheric pressure. The treatment resulted in the formation of a Ti–TiC composite coating with a thickness of about 1 mm on the steel surface. According to the results of the X-ray phase analysis (DRON-3.0 diffractometer, $Cu_k(\alpha)$ radiation), the coating component ratio was 1 : 2. Figure 1 shows a micrograph (JEOL-840 scanning electron microscope) of an unetched vertical section of a coated steel sample.

Previously [3–6], it was ascertained that the anomalous effect of superdeep penetration is possible only in a very narrow range of conditions (corresponding to explosive injection) and particle dimensions in the range from 10 to 100 μm. However, at a comparable velocity of the projectiles in the beam created by the electromagnetic accelerator, a section of the steel substrate (Fig. 1) shows the presence of numerous tracks with a transverse size below 10 μm. Therefore, the size of penetrating particles may be on the order of 1–5 μm. The straight tracks reach a depth of ~50 μm (Fig. 1), after which the particle trajectories become curvilinear and the micrograph shows only their fragments in the form of "paths" crossing the cutting plane: these traces are observed down to a depth of ~350 μm. An analysis of the implanted samples by X-ray photoelectron spectroscopy (Link attachment to the JEOL-840 instrument) confirmed the presence of titanium at this depth. Indirect evidence of the superdeep penetration of titanium was offered by the results of microhardness measurements in the same section. The average microhardness value in a 350-μm-thick surface layer was 2100 MPa, which is approximately 25% higher than the average value for the deeper layers. Thus, the experimental penetration depth of the particles is almost two orders of magnitude higher than their expected dimensions, which allows the phenomenon observed to be classified as "superdeep" penetration.

The results obtained in these experiments agree with the generally known conditions for the superdeep penetration effect, according to which a substrate must be subjected to a high-velocity (~2.0 km/s), high-density

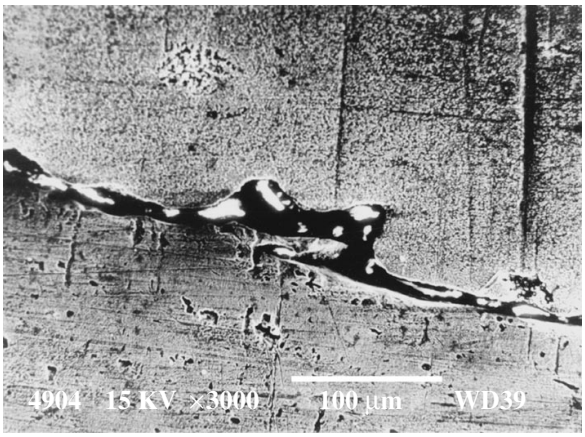

Fig. 1. The scanning electron micrograph of an unetched transverse section of a steel sample (bottom part) coated with a Ti + TiC composition (top part); magnification, ×200.

1063-7850/01/2708-0692$21.00 © 2001 MAIK "Nauka/Interperiodica"

(>1.0 g/cm^3), and sufficiently long (~10^{-4} s) pulsed beam action. However, the observed tracks exhibit no full collapse, showing only some "healing" of the entrance holes and an increase in the track diameter with the penetration depth. In some cases, the tracks exhibit branching. In the micrograph of Fig. 1, a dark-contrast zone in the middle is probably due to a cleavage of the Ti–TiC brittle solid composition. Such defects could be avoided by more thoroughly preparing the sample sections. The same sample was repeatedly lapped, polished, and etched in a 5% HNO_3–C_2H_5OH solution. An investigation of the new section in the same scanning electron microscope gave interesting new results: the entire retained substrate–coating boundary exhibited uniformly distributed toothlike defects. A scanning electron micrograph presented in Fig. 2 shows these defects at a 6500-fold magnification. This micrograph apparently demonstrates unfinished cumulative processes. Clearly seen are the noncollapsed cumulative cavities containing solidified residues of the cumulative streams, as well as the voids and entrance holes of the penetrating particles. Note a dark trajectory of a deep-penetrating stream in the right-hand part of the micrograph (Fig. 2). The geometry of the observed fragments fully corresponds to the classical concepts of cumulative theory [7].

The cumulative effects observed can be given a quite natural (and even obvious) explanation. A front of the pulsed beam incident onto the substrate surface is not (and cannot) be flat and is characterized by a relief with convex and concave parts. When a concave front part strikes a flat substrate, with the edges first reaching the surface, we observe a classical cumulative system configuration. The collapse of the concavity and the formation of a cumulative stream of the surface material are ensured by the oncoming flow of the substance having a mass rate close to the stream velocity. Both the density of the substance in the cumulative jet and its velocity are markedly greater than the analogous values in the initial stream. According to the hydrodynamic theory [7], the stream penetration depth L into the target is determined by the Lavrent'ev formula:

$$L = l\sqrt{\rho_1/\rho_2},$$

where l is the effective length of the cumulative stream and ρ_1 and ρ_2 are the implant and substrate material densities, respectively.

The stream length may be three times the depth of the initial cumulative cavity. A simple estimate according to the hydrodynamic model shows that the stream penetration by a straight trajectory reaching a depth of ~50 μm is possible for a hemispherical cavity base diameter of 20–30 μm and a transverse stream size on the order of 1 μm. Further penetration by a curvilinear trajectory down to a depth of ~350 μm can be explained, with an allowance for the elastic interaction,

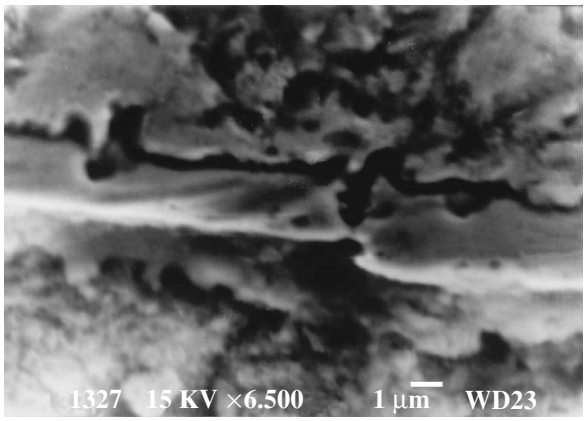

Fig. 2. A scanning electron micrograph of an etched transverse section showing manifestations of the frozen cumulative processes (magnification, ×6500).

by the stream motion via advancing cracks and the grain boundaries of the steel microstructure. The possibility of such a mechanism of solid particle penetration was theoretically justified [8, 9] and experimentally confirmed in this study by a strong change in the steel microstructure manifested by the grain refinement and by the grain boundary rupture down to a depth of ~350 μm.

Manifestations of the cumulative penetration mechanism can be also observed for a high-speed and dense flux of solid microparticles created in explosive cumulative accelerators such as those employed in [3–6]. Convincing evidence for this hypothesis is provided by the results of numerical calculations of the particle flux parameter [10]. According to these data, a geometric envelope of the frontal part of the particle flux with a maximum possible density (~4.0 g/m^3) possesses the shape of a cumulative concavity. Although the above hypothesis is based on the results of experimental observations, some additional investigations are necessary.

Acknowledgments. The author is grateful to A.P. Il'in (High Voltage Research Institute), A.M. Gromov, and N.V. Bychin (both from the Altai Federal Research and Production Center) for their help in work and fruitful discussions.

This study was supported by the project "Development of Scientific and Technological Principles for the Dynamic Synthesis of Superhard Materials and Related Coatings" within the framework of the Program "Scientific Research in Higher Education in the Directions of Science and Technology" of the Ministry of Education of the Russian Federation.

REFERENCES

1. A. A. Sivkov, RF Patent No. 2 150 652, 7F41B 6/00, Byull. No. 16 (2000).

2. A. A. Sivkov, Prikl. Mekh. Tekh. Fiz. **42** (1), 3 (2001).
3. K. I. Kozorezov, V. N. Maksimenko, and S. M. Usherenko, *Selected Problems of Modern Mechanics* (Mosk. Gos. Univ., Moscow, 1981), Part 1, pp. 114–119.
4. A. K. Kozorezov, K. I. Kozorezov, and L. I. Mirkin, Fiz. Khim. Obrab. Mater., No. 2, 51 (1990).
5. K. I. Kozorezov and L. I. Mirkin, Fiz. Khim. Obrab. Mater., No. 3, 75 (1999).
6. K. I. Kozorezov and L. I. Mirkin, Fiz. Khim. Obrab. Mater., No. 1, 77 (2000).
7. *Physics of Explosion*, Ed. by K. P. Stanyukovich (Nauka, Moscow, 1975).
8. S. S. Grigoryan, Dokl. Akad. Nauk SSSR **292** (6), 1319 (1987) [Sov. Phys. Dokl. **32**, 124 (1987)].
9. G. G. Chernyĭ, Dokl. Akad. Nauk SSSR **292** (6), 1324 (1987) [Sov. Phys. Dokl. **32**, 168 (1987)].
10. S. K. Andilevko, G. S. Romanov, and S. M. Usherenko, Inzh.-Fiz. Zh. **61** (1), 46 (1991).

Translated by P. Pozdeev

Technical Physics Letters, Vol. 27, No. 8, 2001, pp. 695–697. Translated from Pis'ma v Zhurnal Tekhnicheskoĭ Fiziki, Vol. 27, No. 16, 2001, pp. 65–70.

High-Power Pulsed Ion Beam Modification of the Surface Properties of Alumina Ceramics

I. G. Romanov and I. N. Tsareva

Nizhni Novgorod Branch of the Blagonravov Institute of Machine Science, Russian Academy of Sciences, Nizhni Novgorod, Russia

Received March 30, 2001

Abstract—The effects of high-energy pulsed ion beam treatment on the surface structure and microhardness of alumina ceramics were studied. The most pronounced changes were observed in the samples exposed to high-power ion beams. The possible mechanisms of material strengthening are discussed. © *2001 MAIK "Nauka/Interperiodica".*

Ion beam processing is a powerful tool of surface modification, which leads to the formation of structures that cannot be obtained by other methods. By varying the ion bombardment conditions, it is possible to modify in a controlled manner the surface properties not only of normal metals and semiconductors [1–3], but of the high-strength materials well [4, 5], thus significantly extending their possible application field.

The purpose of this study was to examine the samples of alumina ceramics (polycor) based on a corundum α-Al_2O_3 phase exposed to a high-power (300 keV) C^+ ion beam in a pulsed charged particle accelerator of the Temp type. The ion beam current density was j = 40–120 A/cm^2 at a pulse duration of $\tau = 10^{-7}$ s; the number of pulses was varied from 1 to 3. For comparison, some ceramic samples were also implanted with B^+ and Ar^+ ions at an energy of 40 keV and an ion beam current density of 10 μA/cm^2. The ion dose was varied from 6×10^{13} to 2×10^{16} cm^{-2}. The structure and phase composition of the initial and ion-bombarded samples were studied by X-ray diffraction on a DRON-3M diffractometer using Cu–K_α radiation. The measurements were performed both in the traditional (Bragg–Brentano) diffraction geometry and at a grazing incidence. The optical metallographic investigations were performed with a Neophot microscope. The degree of modification of the mechanical properties was evaluated by microhardness (H_μ) measurements.

An analysis of the X-ray diffraction data showed that the initial sample structure corresponds to a rolling texture of α-Al_2O_3 of the (0001) $\langle 11\bar{2}0 \rangle$ type with a hexagonal close packing. The diffraction patterns exhibited a characteristic increase in the intensity of reflections with large d_{hkl} values and contained diffraction maxima due to the secondary slip planes. Irradiation of a sample with a single pulse of C ions at j = 60–120 A/cm^2 produced no significant structural changes. Upon increasing the number of pulses to three, the diffractograms display, in addition to the α-doublet from the $(10\bar{1}4)$ plane with d_{hkl} = 0.9045 Å, a new reflection from the $(32\bar{5}4)$ plane with d_{hkl} = 0.9076 Å. The intensity of the new peak increases with the ion beam current density. These structural changes were observed in a 10-μm-thick surface layer of the sample.

The ceramic samples exposed to high-power pulsed ion beams with various j values showed a difference in the character of the reflection intensity variation in depth. For example, the intensity of the $(10\bar{1}2)$ and $(12\bar{3}3)$ peaks in a sample treated at a lower beam current density decreased within a 1-μm-thick layer, but the exposure to a pulse at j = 120 A/cm^2 (heating the sample surface to a maximum temperature) reversed the trend (the peak intensity increased). The high-power C^+ ion beam irradiation leads to a change in the grain size. This is clearly illustrated by micrographs of the sample surface (see Fig. 1): the phenomenon of selective sputtering was manifested both in the corundum grain refinement (Fig. 1b) and in the subsequent grain growth (Fig. 1c).

The high-power pulsed C^+ ion beam treatment led to a significant increase in the surface microhardness H_μ (Table 1). Some decrease in H_μ was observed only for j > 100 A/cm^2. Ions in a nanosecond high-current ion

Table 1. Microhardness $H\mu$ (kgf/mm^2) of α-Al_2O_3 irradiated with a pulsed high-power C^+ ion beam

Number of pulses	Ion beam current density, A/cm^2				
	0	40	80	100	120
1	2250	3800	4000	4500	4500
3	2250	3900	4100	4700	3500

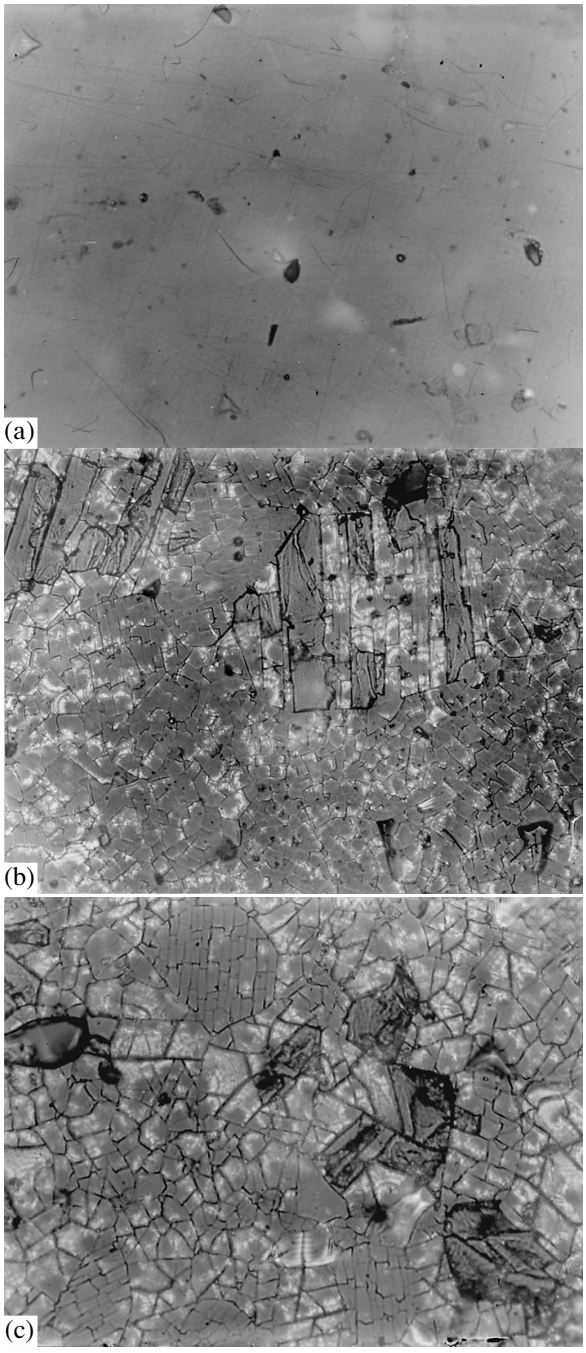

Fig. 1. Micrographs of the surface of α-Al_2O_3 (a) before ion bombardment and (b, c) after exposure to three pulses of a high-power (E = 300 keV) pulsed ion beam at a current density of 80 and 120 A/cm^2, respectively.

beam stopped in the sample produce intense heating of the surface layer, followed by its rapid cooling. A correct interpretation of the structural and phase transitions in ion-irradiated targets require a theoretical calculation of the temperature variation in the surface layer. For metals, this task was solved by Didenko *et al.* [3] based on the thermal conductivity equation. We performed analogous calculations of the spatial and temporal distribution of the temperature fields in Al_2O_3 for the ion beam processing regimes employed. The results showed that a maximum temperature which developed at the surface is significantly below T = 2327 K, the melting point of corundum. Therefore, no melting or evaporation processes, accompanied by the acoustic wave emission with a high pressure amplitude (die to a recoil momentum transfer [3]), take place on the sample surface.

However, an increase in the temperature above another characteristic level of 1320 K sharply decreases the yield strength of Al_2O_3 as a result of the appearance of additional secondary slip systems [6]. Therefore, the grain refinement and the radiation strengthening of corundum can be explained by the plastic deformation process. As indicated above, the intensity of the $(32\bar{5}4)$ diffraction peak appearing at a depth beyond the ion projected range increases with the intensity of the C ion beam processing. According to Pavlov *et al.* [7], the ion irradiation generates acoustic waves with the pressure amplitude proportional to the ion beam current density. As follows from the results of our theoretical calculations [8], a high-power C^+ ion beam pulse in the early stage (20–30 ns) also generates acoustic waves with a pressure amplitude 2–3 orders of magnitude higher than that developed by other ion beam treatments. The irradiation-induced stresses lead to the rotation of the polycrystalline grains in the course of the plastic deformation, which gives rise to the intensity of the X-ray diffraction from the $(32\bar{5}4)$ plane system. Note that the implantation of the B^+ and Ar^+ ions also led to a considerable increase in the microhardness (Table 2), although neither X-ray diffraction nor optical metallography showed evidence of significant changes in the surface layer structure. Only a slight broadening of the diffraction maxima from a 1-μm-thick surface layer was observed in these samples.

It was established [5, 9] that a change in the mechanical properties of materials irradiated to a dose of 10^{14}–10^{15} cm^{-2} was due to the defect formation. The accumulation of the radiation defects and implanted impurity in the target gives rise to stresses favoring plastic deformation and leading to an increase in the dislocation density. This is accompanied by strengthening of the material by a dislocation mechanism. Subsequent irradiation process takes place in the radiation-strengthened material and the accumulation of additional stresses leads to a redistribution of the dislocation density in the bulk and at the grain boundaries. This redistribution is accompanied by relaxation leading to a decrease in H_μ (Table 2, $\Phi = 2 \times 10^{15}$ cm^{-2}). It should be noted that ion doses gained in the case of high-power ion beam treatment at a low current density (j = 40–60 A/cm^2) do not produce strong heating of the sample surface and correspond to small densities of implanted ions. In this case, it is difficult to indicate a

Table 2. Microhardness H_μ (kgf/mm^2) of α-Al_2O_3 irradiated with B^+ and Ar^+ pulsed ion beams

Ion type	Irradiation dose, cm^{-2}				
	0	6×10^{13}	2×10^{14}	10^{15}	2×10^{15}
B^+	2250	3500	4000	4900	4500
Ar^+	2250	3200	4000	4500	3900

dominating mechanism of the surface strengthening. In any case, however, the process of plastic deformation must play a decisive role in the ion beam modification of the surface of ceramic materials.

REFERENCES

1. E. I. Zorin, P. V. Pavlov, and D. I. Tetel'baum, *Ion-implantation Doping of Semiconductors* (Énergiya, Moscow, 1975).
2. *Ion Implantation*, Ed. by J. K. Hirvonen (Academic, New York, 1980; Metallurgiya, Moscow, 1985).
3. A. N. Didenko, A. E. Ligachev, and A. E. Kurakin, *Influence of Charged Particle Beams on Metal and Alloy Surface* (Énergoatomizdat, Moscow, 1987).
4. I. G. Romanov, I. N. Tsareva, and L. A. Krivina, Pis'ma Zh. Tekh. Fiz. **24** (3), 64 (1998) [Tech. Phys. Lett. **24**, 110 (1998)].
5. I. G. Romanov and A. L. Chekanov, Poverkhnost, No. 5, 110 (1993).
6. A. R. Andrievskiĭ and I. I. Spivak, *Strength of Refractory Compounds and Materials Based on Them: Handbook* (Metallurgiya, Chelyabinsk, 1989), p. 367.
7. P. V. Pavlov, Yu. A. Semin, V. D. Skupov, *et al.*, Fiz. Tekh. Poluprovodn. (Leningrad) **20** (3), 503 (1986) [Sov. Phys. Semicond. **20**, 315 (1986)].
8. V. I. Erofeev, I. G. Romanov, and I. N. Tsareva, *Wave Problems of Mechanics: Collection of Scientific Works* (Nizhni Novgorod, 1992), pp. 51–55.
9. A. P. Pavlov, D. I. Tetel'baum, E. V. Kuril'chik, *et al.*, Dokl. Akad. Nauk SSSR **311** (3), 606 (1990) [Sov. Phys. Dokl. **35**, 275 (1990)].

Translated by P. Pozdeev

Technical Physics Letters, Vol. 27, No. 8, 2001, pp. 698–700. Translated from Pis'ma v Zhurnal Tekhnicheskoĭ Fiziki, Vol. 27, No. 16, 2001, pp. 71–75.

Liquid Phase Epitaxy of $Ge_{1-x}Sn_x$ Semiconductor Films

A. S. Saidov, A. Sh. Razzakov, and É. A. Koshchanov

Physical Engineering Institute, Solar Physics Research and Production Corporation, Academy of Sciences of the Republic of Uzbekistan, Tashkent, Uzbekistan

e-mail: atvi@physic.ursci.net

In final form received March 19, 2001

Abstract—Epitaxial layers of $Ge_{1-x}Sn_x$ semiconductor solid solutions on germanium substrates were grown from a limited volume of a tin-based solution melt in a temperature interval from 740 to 450°C. Optimum conditions favoring the growth of crystallographically perfect epitaxial films were established based on the results of the X-ray diffraction and morphological study of the samples. © *2001 MAIK "Nauka/Interperiodica".*

The task of expanding the photosensitivity of semiconductor detectors to the IR spectral range is among the currently important problems in optoelectronics. In this context, study of the possibilities offered by the synthesis of semiconductor solid solutions based on the most thoroughly characterized narrow-bandgap materials, such as Ge and Sn, is certainly of interest. Although the formation of solid solutions based on the Ge–Sn system was considered (by analogy with the Si–Ge system) as theoretically possible, no epitaxial growth of such solid solutions was reported until now.

Below we present the results of an investigation of the epitaxial growth of $Ge_{1-x}Sn_x$ solid solutions from a tin-based solution melt by the method of controlled cooling in a temperature interval from 740–450°C in a hydrogen atmosphere. The samples were grown from a volume of the solution melt confined between two substrates. The process was terminated when the solution melt was removed from the gap by means of centrifugation. The substrates were ⟨111⟩-oriented germanium wafers of the acceptor conductivity type possessing a resistivity of 40 Ω cm. The wafers were 50 mm in diameter and had a thickness of 350–400 μm. The solution–melt compositions (Sn + Ge, Sn + Ge + Zn, Sn + Ge + Zn + Se) and the corresponding temperature intervals were selected based on the published data [1] and the results of preliminary experiments.

Compositions of the initial $Ge_{1-x}Sn_x$ solid solutions and the distribution of components in the epitaxial layers grown were studied on a JEOL X-ray microanalyzer. It was found that the x value, as well as the homogeneity of the component distribution both in the depth of the epitaxial layer and in the directions parallel to the crystallization front, depends on the melt composition and the crystallization onset temperature. As the content of zinc (or, the more so, of the sum of zinc and selenium) in the melt increases, the tin content in the solid solution also sharply increased as well. This probably reflects the effect of the third component on the effective distribution coefficients. It was also established that, under otherwise equal conditions and for the same melt composition, an increase in the crystallization onset temperature leads to an increase in the Sn content in the $Ge_{1-x}Sn_x$ solid solution.

We have grown homogeneous mirror-flat epitaxial layers of $Ge_{1-x}Sn_x$ solid solutions from a Ge + Sn + ZnSe solution melt at a crystallization temperature of T_1 = 740°C (x = 0.1) or T = 540°C (x = 0.03). An analysis of the X-ray fluorescence spectra (displaying high-intensity peaks due to germanium and tin at λ = 1244 and 925 mÅ, respectively) before and after sequential layer removal showed that the concentrations of Ge and Sn were constant both in the lateral direction and in the growth direction. The thickness of the epitaxial layers grown on Ge substrates varied from 5 to 35 μm, depending on the gap width d between the substrates and on the growth regime.

The quality of epitaxial $Ge_{1-x}Sn_x$ layers grown on Ge substrates was also dependent of the controlled cooling rate, which was varied between 0.5 and 7.5 K/min. The optimum interval of cooling rate favoring the growth of mirror-smooth $Ge_{1-x}Sn_x$ films was 0.5–1.5 K/min, which corresponded to the crystallization rate (front velocity) of 0.13–0.2 μm/min. In addition, the structure perfection of the semiconductor layers grown depended on the gap width δ between the horizontal substrates. This value could be varied from 0.25 to 2.5 mm with the aid of special graphite spacers. For δ < 0.25 mm, no epitaxial growth took place, probably, because the melt did not wet the substrate surface. The most perfect layers of solid solutions on both upper and lower substrates were grown for δ = 0.65–1 mm. For δ > 0.85 mm, layers of significantly different quality were obtained on the upper and lower substrates: the quality of epitaxial films was always better on the lower substrates than on the upper ones. This was manifested,

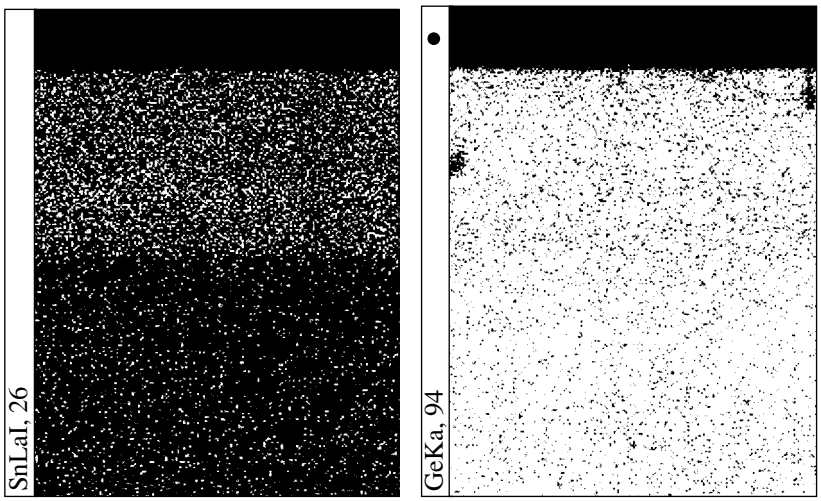

Fig. 1. Scanning micrographs of the transverse cleavages of Ge–$Ge_{1-x}Sn_x$ structures ($x = 0.03$).

in particular, by a difference in the surface dislocation densities. This difference increased with δ. In our opinion, this was explained by the fact that the convective flows dominated over molecular diffusion in the overall mass transfer to the crystallization front [2].

The character of component distribution in the depth of the epitaxial layers was qualitatively assessed by studying the transverse cleavages of Ge–$Ge_{1-x}Sn_x$ structures. An investigation of the scanning micrographs showed evidence of an almost homogeneous distribution of components across the epitaxial film (Fig. 1).

An analysis of the scanning micrographs and the morphological study of $Ge_{1-x}Sn_x$ solid solutions showed that defects appearing at the substrate–film interface depend on the x value. A mismatch between the lattice parameters of the substrate and the first crystallized solid solution layer appears because this layer comprises $Ge_{1-x}Sn_x$ with $x > 0$, while the substrate is made of pure Ge. As the subsequent epitaxial layers are grown, this difference decreases because the difference in x between the adjacent layers is insignificant. Elastic deformation of each completed layer, which serves as a the substrate for the subsequent layer growth, leads to a decrease in the total system energy. After the crystallization of each next layer without changing the lattice constant, this energy is always smaller than that in the initial process stage. By changing the growth regime, it is possible to control the perfection of heterojunctions. It was established that following an increase in the tin content in the $Ge_{1-x}Sn_x$ solid solution above $x > 0.1$, the structural perfection of epitaxial layers sharply deteriorates and even second phase precipitation may take place.

The quality of the crystal structure was assessed and the lattice parameters were determined by X-ray diffraction measurements performed on a DRON-UM1 diffractometer. These measurements were performed on specially prepared samples with a thickness of d = 3–5 μm. The diffraction spectra were obtained by continuous recording using the CuK_α (λ_α = 1.5418 Å) and CuK_β (λ_β = 1.3922 Å) radiations from an X-ray tube operating at 30 kV and 10 mA. The time of exposure was varied within 1–3 h. As can be seen from a typical diffractogram presented in Fig. 2, the positions of peaks from the film and substrate differ insignificantly. This implies that the lattice parameters are close to each other (a_{Ge} = 5.656 Å, $a_{Ge_{1-x}Sn_x}$ = 5.681 Å), while the absence of other peaks in the diffractogram is additional evidence of a single-crystal structure of the epitaxial layers obtained [3].

We have also studied some electrical characteristics of the epitaxial films. Undoped epitaxial layers of the $Ge_{1-x}Sn_x$ solid solutions exhibited electric conductivity of the acceptor type. We determined the specific resis-

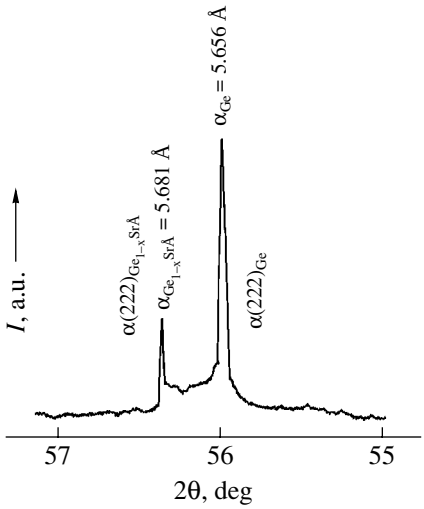

Fig. 2. A typical X-ray diffractogram of the Ge–$Ge_{1-x}Sn_x$ epitaxial heterostructure ($x = 0.03$).

tivity, Hall mobility, and charge carrier concentration at 100 and 300 K to obtain $\rho = 5.33 \times 10^{-3}$ Ω cm, $\mu = 75$ cm^2/(V s), $n = 1.56 \times 10^{19}$ cm^{-3} and $\rho = 4.62 \times 10^{-3}$ Ω cm, $\mu = 110$ cm^2/(V s), $n = 1.23 \times 10^{19}$ cm^{-3}, respectively.

Thus, we have experimentally demonstrated the possibility of growing structurally perfect epitaxial layers of $Ge_{1-x}Sn_x$ solid solutions from a tin-based solution melt on germanium substrates under selected optimum crystallization conditions.

REFERENCES

1. V. M. Andreev, L. M. Dolginov, and D. N. Tret'yakov, *Liquid-Phase Epitaxy in the Technology of Semiconductor Devices* (Sov. Radio, Moscow, 1975), p. 328.
2. A. S. Saidov, É. A. Koshchanov, A. Sh. Razzakov, *et al.*, Uzb. Fiz. Zh., No. 1, 16 (1997).
3. A. S. Saidov, É. A. Koshchanov, and A. Sh. Razzakov, Pis'ma Zh. Tekh. Fiz. **24** (2), 12 (1998) [Tech. Phys. Lett. **24**, 47 (1998)].

Translated by P. Pozdeev

Technical Physics Letters, Vol. 27, No. 8, 2001, pp. 701–704. Translated from Pis'ma v Zhurnal Tekhnicheskoĭ Fiziki, Vol. 27, No. 16, 2001, pp. 76–84.

Chaotic Synchronization in a System of Inductively Coupled Oscillators

É. V. Kal'yanov

Fryazino Branch, Institute of Radio Engineering and Electronics, Russian Academy of Sciences, Fryazino, Moscow oblast, Russia

Received March 7, 2001

Abstract—A system of two inductively coupled chaotic oscillators is considered. Normalized equations of motion for oscillators with arbitrary parameters are derived in the case of a cubic approximation of the nonlinear elements. The results of a numerical analysis of the features of interaction between chaotic coupled nonidentical subsystems are presented and a realistic experiment is described. © *2001 MAIK "Nauka/Interperiodica".*

At present, many researchers are interested in nonautonomous (forced) systems of bistable chaotic oscillators [1–3]. Several papers (see, e.g., [4, 5]) were devoted to the study of interactions between oscillators of this type with resistive and capacitive coupling. However, another widely encountered type of coupling between oscillators—inductive—has remained unstudied. At the same time, we may expect that a system of inductively coupled interacting bistable oscillators exhibit significant features of chaotic behavior. This is related to the type of attractor inherent in each partial subsystem representing a Chua's circuit. As is well known [6], such circuits possesses an attractor structure of the double scroll type, which is caused by the presence of chaotic motions of two types. One of which is determined by the resonance frequency of the oscillation circuit of each subsystem, while the other is determined by a chaotically changing frequency of switching between stable states of subsystems [3]. The possibility of the manifestation of filter properties is related to the fact that the frequency spectra of switching oscillations of the partial subsystems occur beyond the frequency bands of the oscillatory circuits.

Below we will consider a system of two inductively coupled Chua's oscillators with allowance for losses. The normalized equations of motion for the system with arbitrary parameters of the partial subsystems are derived. The results of a numerical analysis are presented and an experiment is described.

The system of coupled Chua's oscillators under consideration differs from that reported in [5] by only an inductive (rather than a resistive or capacitive) coupling between the partial oscillatory circuits being provided. In the analysis of the inductively coupled Chua's oscillators we will assume that each of the two subsystems (i = 1, 2) contains (in the terms and notations of [5]) inductance L_i, resistors R_i and R_{Li}, capacitors C_i and C_{0i}, and a nonlinear element g_i.

Using a cubic approximation of the characteristics of nonlinear elements, normalized equations describing oscillatory processes in the inductively coupled Chua's circuits can be written as

$$\begin{aligned}
\dot{x}_1 &= \alpha_1[y_1 - x_1(1 - \nu_1 + \mu_1 x_1^2)],\\
\dot{y}_1 &= x_1 - y_1 + z_1,\\
\dot{z}_1 &= [\beta_1/(1-k^2)][k_2(y_2 + \rho_2 z_2) - (y_1 + \rho_1 z_1)],\\
\dot{x}_2 &= \gamma_R\alpha_2[y_2 - x_2(1 - \nu_2 + \mu_2 x_2^2)],\\
\dot{y}_2 &= \gamma_R\alpha_0(x_2 - y_2 + z_2),\\
\dot{z}_2 &= [\beta_2/\gamma_R(1-k^2)][k_1(y_1 + \rho_1 z_1) - (y_2 + \rho_2 z_2)].
\end{aligned} \tag{1}$$

Here, variables x_i and y_i reflect voltage variations on the capacitors C_i and C_{0i}, respectively; variables z_i reflect the variation of currents in the inductances L_i. The upper dot indicates differentiation with respect to dimensionless time t related to the real time t^* by the formula $t = t^*(R_1C_{01})^{-1}$. The inductive coupling between the subsystems is characterized by the coupling coefficient $k^2 = k_1k_2$, where $k_i = M/L_i$ are the degrees of coupling and M is the mutual inductance factor. The other parameters in Eqs. (1) are as follows: $\alpha_i = C_{01}/C_i$; $\alpha_0 = C_{01}/C_{02}$; $\beta_i = C_{01}R_1^2/L_i$; $\gamma_R = R_1/R_2$; $\rho_i = R_{Li}/R_i$. Coefficients ν_i and μ_i determine the nonlinear characteristics of active elements in the subsystems.

In practice, the oscillators with chaotic dynamics cannot be identical, since their main feature is a strong dependence of the character of chaotic oscillations not only on the initial conditions, but on any other parameter as well. Even if the elements of the partial oscillators are thoroughly selected, it is unlikely that a difference

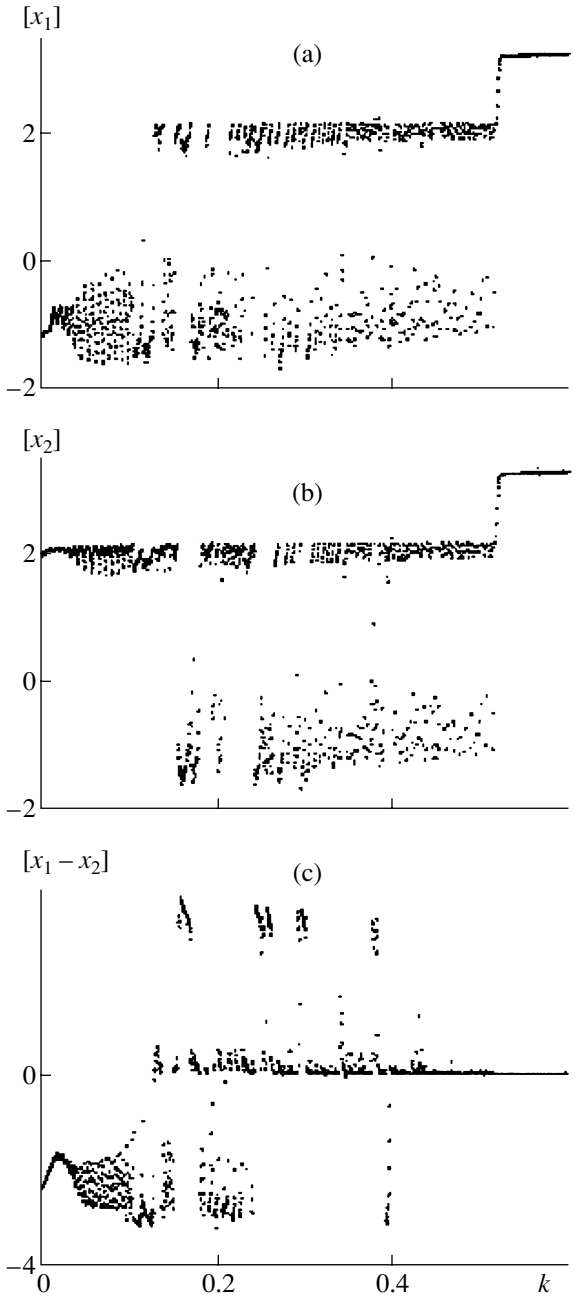

Fig. 1. Bifurcation diagrams illustrating variation of the maximum values of the oscillation processes (a) $x_1(t)$, (b) $x_2(t)$, and (c) the difference $x_1(t) - x_2(t)$ depending on the coupling parameter k.

in chaotic oscillations in the two subsystems can be eliminated under real conditions. For this reason, it was expedient to study Eqs. (1) in application to nonidentical partial subsystems.

For brevity and clarity of consideration of the features of interaction between inductively coupled Chua's oscillators, the numerical analysis was restricted to the case when a difference between the resonance frequencies of subsystems is related to a change in the capacitance C_{02}. This difference is determined by a change in the parameter α_0 that can be conveniently referred to as the "nonidentity" parameter.

The numerical calculations were carried out for various losses in the coupled oscillators. It was assumed that losses are the same in both subsystems ($\rho_1 = \rho_2 = \rho$). The constant parameters were selected as follows: $\alpha_i = 9$, $\beta_i = 14.28$; $\nu_i = 1.25$, $\mu_i = 0.1$. For certainty, the initial conditions in the subsystems are selected equal to $x_1(0) = -0.1$; $x_2(0) = 0.1$; $y_i(0) = z_i(0) = 0$. In the case of nonidentical subsystems under consideration, $k_1 = k_2 = k$ because $L_1 = L_2$.

The numerical calculations were performed by the Runge–Kutta method with a temporal integration step of 0.025. The process of chaotization was studied by considering the time patterns of oscillations, attractors, and oscillation power spectra. Also calculated were the characteristic Lyapunov's indices and bifurcation diagrams. The latter diagrams are very informative in illustrating processes in the systems with chaotic dynamics and especially in coupled chaotic systems.

A special feature in the operation of inductively coupled Chua's oscillators was that, in the absence of losses in the circuits, even very small nonidentity ($\alpha_0 = 1.000001$) was sufficient to prevent the system from mutual chaotic synchronization. At the same time, the chaotic synchronization at this α_0 value is possible in the presence of relatively small losses ($\rho = 0.001$).

Figures 1 and 2 illustrate the process of chaotic synchronization development in a system described by Eq. (1). The bifurcation diagrams in Fig. 1 show a variation of the maximum values of the oscillation processes $x_1(t)$(Fig. 1a) and $x_2(t)$ (Fig. 1b), as well as of the difference $x_1(t) - x_2(t)$ (Fig. 1c) (denoted by $[x_1]$, $[x_2]$, and $[x_1 - x_2]$, respectively), calculated as functions of the coupling parameter k at $\alpha_0 = 0.014$.

The diagram in Fig. 1a shows that no self-excited oscillations are observed in the system at $k < 0.01$. This regime can be considered as "prestart" with respect to the coupling parameter. In this regime, the system of inductively coupled oscillators behaves similarly to a delay trigger. This unusual property of the coupled system is confirmed by its behavior under the action of an applied harmonic signal. The "prestart" regime is manifested by the transformation of external harmonic oscillations into relaxation oscillations. In the calculation of the trigger properties of the system, the external harmonic oscillations were added in the form of $A_s\cos(\omega_s t)$ (A_s and ω_s are the amplitude and frequency of the external forcing action) to the right-hand part of the first equation in system (1). At $k = 0.01$, the system shows bifurcation of the Hopf type and in the interval $k \in [0.01; 0.14]$ it exhibits a period doubling bifurcation according to Feigenbaum, after which a chaotic oscillation regime is established with an attractor of the Roessler type. The chaotic oscillations with an attractor

of the double scroll type exist in the interval of $k \in [0.14; 0.55]$. This is evidenced, in particular, by the presence of two regions in which the $x_1(t)$ maxima exhibit random scattering. At $k > 0.55$, the system features regular oscillations with a large limiting cycle.

Similar bifurcation phenomena are observed for the $x_2(t)$ oscillation process illustrated in the diagram of Fig. 1b. In accordance with the positive initial condition, $x_2(0) = 0.1$, a maximum value of $x_2(t)$ in the trigger regime occurs in the vicinity of a stable state with positive $[x_2]$ value. As the coupling parameter increases, oscillations with an attractor of the Roessler type develop near this $[x_2]$ value.

The diagram of Fig. 1c clearly illustrates the behavior of the system in the region of coupling parameters featuring the mutual chaotic synchronization regime. For completely identical synchronous oscillation processes $x_1(t)$ and $x_2(t)$, the maximum difference value $[x_1 - x_2]$ is zero, as is seen, for example, in the region of $k = \in [0.5; 0.6]$. If the mutually synchronized oscillations are nonidentical, the $[x_1 - x_2]$ value exhibits some scatter relative to the zero level (e.g., in the region of $k \in [0.4; 0.5]$).

Figure 2 illustrates synchronous chaotic oscillations in the system of inductively coupled oscillators with $k = 0.422$. Figures 2a and 2b show the attractors corresponding to the oscillation processes $x_1(t)$ and $x_2(t)$; Fig. 2c shows a projection of the imaging point trajectory onto the $\{x_1, x_2\}$ plane. The attractors illustrate the chaotic character of the interacting oscillations. As can be seen in Fig. 2c, the projection of the imaging point trajectory falls in the vicinity of the $x_1 = x_2$ line, which is evidence of synchronous phase-correlated motion. Deviations of the trajectories from this line is due to nonidentity of the synchronous chaotic oscillations. The band of mutual chaotic synchronization for inductively coupled oscillators increases (as well as that for the resistively and capacitively coupled systems) with increase in the coupling parameter. The system is characterized by a certain synchronization threshold.

A system of inductively coupled Chua's oscillators was experimentally studied using oscillators of the type described previously [5]. The inductive coupling of partial oscillators was provided by including additional coupled inductances L_1^0 and L_2^0 in series with L_1 and L_2. The values of both additional inductances were selected equal to 1 mH. The experiment showed the existence of oscillations in the coupled system in a regime when the same uncoupled partial oscillators do not exhibit excitation and confirmed the possibility of the partial synchronization of the inductively coupled oscillators. A complete synchronization seems to be hindered by significant active losses in the inductive elements and by a relatively large scatter of the real parameters as well as of the nonlinear elements in the partial subsystems.

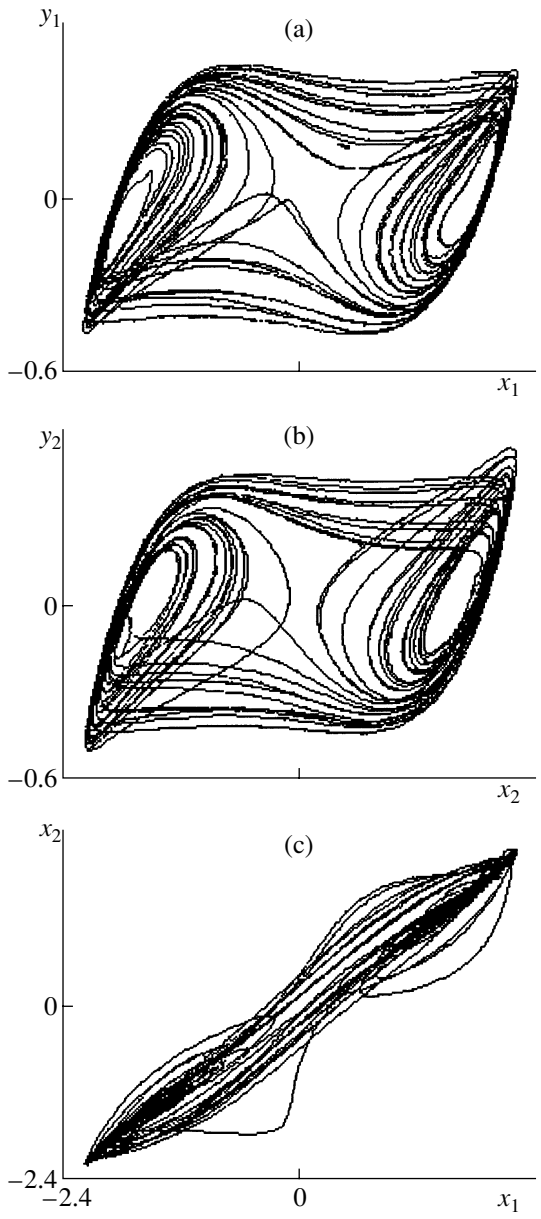

Fig. 2. Oscillations in a system of inductively coupled Chua's oscillators: (a, b) attractors corresponding to the oscillation processes $x_1(t)$ and $x_2(t)$, respectively; (c) a projection of the imaging point trajectory onto the $\{x_1, x_2\}$ plane.

The results of this investigation showed that inductively coupled Chua's circuits may feature chaotic oscillations in a regime when the uncoupled partial oscillators do not exhibit excitation as a result of active losses in the partial circuits. The operation regime of the inductively coupled system can be controlled by varying the coupling parameter so as to pass from trigger to self-sustained oscillation mode. Depending on the degree of coupling, either chaotic oscillations with an attractor of the Roessler type or the chaotic oscillations (synchronous or nonsynchronous) with a double

scroll attractor may be excited. In the case of strong coupling, synchronous regular oscillations corresponding to a simple limiting cycle are possible as well.

Acknowledgments. This study was supported by the Russian Foundation for Basic Research, project nos. 98-02-16722.

REFERENCES

1. V. S. Anishchenko, A. N. Sil'chenko, and I. A. Khovanov, Pis'ma Zh. Tekh. Fiz. **24** (7), 22 (1998) [Tech. Phys. Lett. **24**, 257 (1998)].
2. É. V. Kal'yanov, Radiotekh. Élektron. (Moscow) **44** (3), 315 (1999).
3. É. V. Kal'yanov, Radiotekh. Élektron. (Moscow) **44** (5), 574 (1999).
4. V. V. Astakhov, A. V. Shabunin, and V. S. Anishchenko, Radiotekh. Élektron. (Moscow) **42** (8), 974 (1997).
5. É. V. Kal'yanov and G. N. Kal'yanov, Radiotekh. Élektron. (Moscow) **45** (5), 586 (2000).
6. L. O. Chua, M. Komuro, and T. Matsumoto, IEEE Trans. Circuits Syst. **CAS-33** (11), 1073 (1986).

Translated by P. Pozdeev

Technical Physics Letters, Vol. 27, No. 8, 2001, pp. 705–706. Translated from Pis'ma v Zhurnal Tekhnicheskoĭ Fiziki, Vol. 27, No. 16, 2001, pp. 85–89.

A Study of the $Bi_2Sr_2CaCu_2O_y$ Film Bolometer Response to Constant-Power IR Laser Pulses with a Variable Duty Ratio

S. V. Antonenko, K. V. Bryzgunov, D. P. Korotkov, and S. N. Mal'tsev

Moscow Engineering Physics Institute (Technical University), Moscow, Russia

e-mail: e-creative-group@mtu-net.ru

Received February 12, 2001

Abstract—An optical rod probe technique was developed for the study of a bolometric response of high-temperature superconductor films on solid substrates exposed to IR laser pulses of constant power and variable duty ratio. The IR radiation was produced by a semiconductor laser with an original pump generator. The method proposed was used to study the characteristics of a superconductor bolometer based on a $Bi_2Sr_2CaCu_2O_y$ film on a MgO substrate. It was found that an increase in the pulse repetition rate of the IR laser from 1 to 7 kHz leads to a drop (by a factor of 2.5) in the variable component of the bolometer response amplitude. © *2001 MAIK "Nauka/Interperiodica".*

At present, thermal radiation detectors using bolometers based on high-temperature superconductor films of the YBaCuO system are being extensively studied [1, 2]. Similar to the other types of bolometers using the thermal mechanism of detection, these devices, offer either a high sensitivity at a low operation speed or vice versa. Nevertheless, in some special cases (e.g., in the development of bolometric detectors of modulated radiation), it is interesting to study the operation of bolometers detecting a sequence of optical radiation pulses with equal amplitudes and minimum possible duty ratio (at which the signal pulses can still be resolved).

Previously, the bolometric detectors were most frequently studied using a blackbody radiation source [3, 4] and a mechanical chopper (a rotating disk with a hole segment) as a modulator. This source does not ensure the constancy of the radiation energy during the pulse when the pulse repetition rate is changed. Almost all experiments were performed with a bolometric element placed in vacuum at the end of an optical cryostat, to which the radiation was transmitted via an optical window [5–7]. In such schemes, it is difficult to change the samples and there is a need for the additional collimation and focusing of radiation on the sample.

We have developed a new method according to which radiation is transmitted to a bolometer via a quartz light guide. The thermal detector element, which is fastened to a copper end flange of the optical rod immediately at the light guide output, occurs in a gaseous helium medium. This scheme provides for additional heat removal from the bolometer to the gas phase. In the case of a liquid nitrogen cryostat, this possibility is retained if a gas-filled rod is employed. The bolometer was connected to a measuring electrical circuit according to a traditional four-contact scheme.

A laser radiation source produced a sequence of identical pulses at a wavelength of 850 nm, with a pulse duration of 100 ns, variable (1 to 10 kHz) repetition rate, and a constant pulse power of 100 W. The characteristics of the bolometer response to this pulsed radiation were measured using a Hewlett Packard digital oscillograph with a maximum sensitivity of 1 mV, which was capable of signal averaging over a preset number of measurements (4 to 256 points). The dynamic (variable) signal detection was studied by the oscillograph operating in a constant component cut-off mode.

The bolometer was based on a $Bi_2Sr_2CaCu_2O_y$ film deposited onto a MgO substrate. The film was processed by a laser scribing method to form a 1.1×1.1 mm meander pattern (11 periods with a cut width of 5 μm), after which silver contacts were applied by thermal deposition in vacuum. The films exhibited a superconducting transition in the region of 84–95 K.

Oscillograms of the bolometer response were measured first at a laser pulse repetition rate of 2 kHz at various temperatures in the entire interval of the superconducting transition. The maximum response was observed at 92 K; all subsequent measurements were carried out at this temperature. It must be noted that a change in the bolometer resistance (the working point drift) caused by the laser heating at a repetition frequency of 2 kHz increased during the first 30 s of the laser operation, a total drift amounting to about 5% of the superconducting transition height. The curves of the variable component of the bolometer response amplitude versus pulse repetition rate were measured in the range from 1 to 7 kHz.

The results of these measurements showed that the variable component of the bolometer response amplitude exhibits a drop with increasing repetition rate of

1063-7850/01/2708-0705$21.00 © 2001 MAIK "Nauka/Interperiodica"

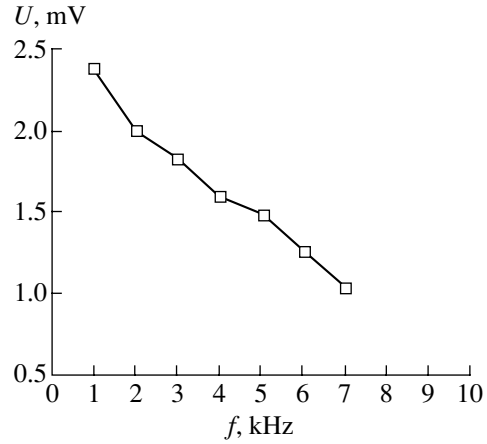

Fig. 1. A plot of the amplitude of the variable bolometer response component versus laser pulse repetition rate.

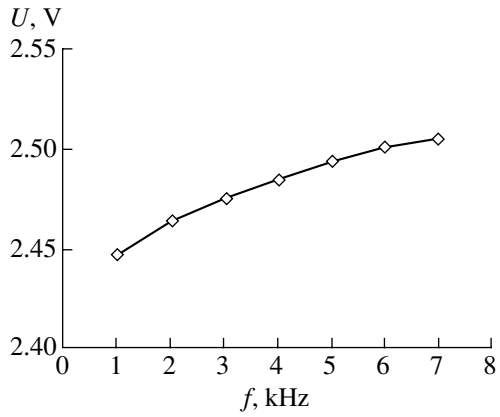

Fig. 2. A plot of the amplitude of the constant bolometer response component versus laser pulse repetition rate.

the laser pulses. A typical plot of this dependence is presented in Fig. 1. We have also studied the dependence of the constant component of the response voltage on the pulse repetition rate. As the repetition rate increases, the working point of the bolometer exhibited a nonlinear variation (Fig. 2). However, as noted above, the characteristic time of this process is on the order of a few dozens of seconds. Since the working point does not leave the linear region of the superconducting transition characteristic, it is possible not to introduce a system of thermal compensation during measurements of the variable response component.

The proposed experimental scheme may be useful for studying the action of a modulated IR laser radiation upon various high-temperature superconductor bolometers operating in the pulse repetition frequency range from 1 to 10 kHz.

Acknowledgments. The authors are grateful to the Hewlett Packard Company (Russian Office) for kindly providing a digital oscillograph for the experiment.

This study was supported by the Federal Targeted Program “Integration,” project no. A0133.

REFERENCES

1. I. Aboudihab, A. Gilabert, *et al.*, Supercond. Sci. Technol. **7** (2), 80 (1994).
2. D. C. Jurbergs, J. Zhao, and J. T. McDevitt, Appl. Phys. Lett. **69** (5), 688 (1996).
3. A. I. Khrebtov, M. B. Krayukhin, A. Yu. Klimov, *et al.*, Prib. Tekh. Éksp., No. 2, 162 (1993).
4. A. Bottiglione, M. Epifani, *et al.*, J. Appl. Phys. **74** (1), 704 (1993).
5. H. Neff, W. Schaube, J. Laukemper, *et al.*, J. Appl. Phys. **77** (9), 4580 (1995).
6. F. A. Hegmann, R. A. Hughes, and J. S. Preston, Appl. Phys. Lett. **64** (23), 3172 (1994).
7. S. V. Antonenko, K. V. Bryzgunov, and D. P. Korotkov, in *Proceedings of the XXXII Conference on Low Temperature Physics, 2000*, p. 191.

Translated by P. Pozdeev

Technical Physics Letters, Vol. 27, No. 8, 2001, pp. 707–708. Translated from Pis'ma v Zhurnal Tekhnicheskoĭ Fiziki, Vol. 27, No. 16, 2001, pp. 90–94.

High-*Q* Adjustable Superconducting High-Frequency Circuit

E. A. Vopilkin, A. E. Parafin, S. A. Pavlov, L. I. Ponomarev, A. Yu. Ganitsev, A. S. Zhukov, V. V. Vladimirov, A. G. Letyago, and V. V. Parshikov

Institute for Physics of Microstructures, Russian Academy of Sciences, Nizhni Novgorod, Russia

e-mail: vopilkin@ipm.sci-nnov.ru

Received March 13, 2001

Abstract—The possibility of creating a high-*Q* ($Q \sim 10^5$) superconducting HF circuit mechanically adjustable in a broad frequency range was studied. The device comprises two planar single-coil structures based on YBaCuO superconducting films. The component coils were deposited onto lanthanum aluminate, neodymium gallate, or strontium titanate substrates. © *2001 MAIK "Nauka/Interperiodica".*

The high quality of electronic devices based on high-temperature superconductor (HTSC) films is determined by their low surface resistance R_s [1, 2]. Resonators, filters, and other devices based on HTSC films of the YBaCuO system usually operate in a gigahertz frequency range [3]. However, the region of lower (HF) frequencies also requires high-*Q* filters [4, 5]. Withers *et al.* reported on the nonadjustable circuits with a resonance frequency from 5 to 35 MHz and $Q \sim$ 16 000 obtained by deposition onto lanthanum aluminate substrates. Gao *et al.* [7] obtained a resonator operating at 24.5 MHz with $Q \sim 40\,000$ and proposed a filter composed of three such units. The structure was also based on a lanthanum aluminate substrate.

We have prepared planar single-coil structures using substrates of three types—LaAlO, GaNdO, and SrTiO—on which the YBaCuO films were formed by a laser deposition technique [8]. The films had a thickness of $d \sim 150$ nm, a critical temperature of $T_c \geq 88$ K, and a critical current density of $j_c \sim 1$ MA/cm^2 (short bridge). The HTSC coil pattern was obtained by photolithography; the films were etched in a 1% aqueous phosphoric acid solution.

Figure 1 shows the topology of the inductance coil and capacitor areas forming a planar single-coil circuit. Each flat coil has 20 turns, with an HTSC strip width of 60 μm and a strip spacing of 40 μm. The capacitor areas were 4.6×4.6 and 5×8.6 mm in size. The lateral size uncertainty during the pattern etching was 2–5 μm for each edge.

The adjustable circuit (Fig. 1) comprises a system of two substrates with coil patterns on the inward surfaces facing each other. The circuit resonance frequency variation is provided by changing the spacing *X* (capacitance) between the substrates. The minimum possible distance to which the substrates could be moved is determined by the accuracy of the driving mechanism and by the surface curvature.

The circuit characteristics were determined using an SK4-59 spectrum analyzer. The circuit was probed with coupling loops. The coupling coefficient could be varied by changing the loop positions and mutual orientation. The coefficient of transfer from a transmitting to receiving loop in the entire adjustment range of the circuit was maintained at a level of 20 dB. The power of the oscillator loaded on the transmitting loop was 50 dB mW. The results of measurements of the resonance frequencies and unloaded *Q* values of single-coil structures on various substrates are presented in the table. As can be seen from these data, the resonance characteristics significantly depend on the permittivity and loss tangent of the substrate material. A difference between the *Q* values of about 15000 obtained in this study and reported in [6] and the value of 40000 [7] is probably related to features in the substrate preparation.

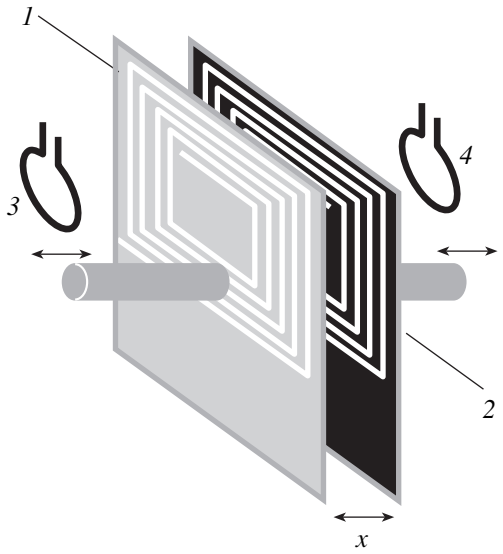

Fig. 1. A schematic diagram of the adjustable circuit: (*1*, *2*) substrates with HTSC films; (*3*, *4*) coupling loops; (*X*) spacing between films.

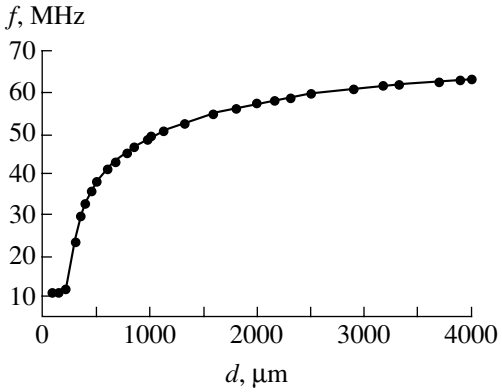

Fig. 2. A plot of the resonance frequency of the adjustable circuit versus plate spacing.

The measured inductance of each coil was about 3.5 μH, from which we infer that the intrinsic capacitance of a planar coil structure on lanthanum aluminate or neodymium gallate was about 1.5 pF. The adjustable circuits were composed of single-coil structures based on neodymium gallate with parameters close to those presented in the table. During the measurements, the substrates were immersed into liquid nitrogen and freeze-fastened onto quartz holders. The distance between holders was controlled with the aid of a micrometric screw and measured using a Micron-1 instrument to within one micron. Figure 2 shows an experimental plot of the resonance frequency f_r of the adjustable contour versus the distance X between substrates with coils. The maximum frequency is 63 MHz; a minimum frequency of 12 MHz corresponds to the substrates touching each other.

As the frequency decreases, the rate of the frequency adjustment grows. We may estimate this rate by assuming that it is determined primarily by a change in capacitance between the capacitor areas ($C \sim 1/X$). A maximum frequency of the adjustable circuit being close to that of the single planar coil, we may assume that the system capacitance at a maximum substrate spacing is much smaller than the intrinsic capacitance of the coils. At a frequency equal to half of the maximum, the derivative can be estimated by the formula $df/dX \approx (0.6 f_{max} C_0)/(\varepsilon\varepsilon_0 S)$, where C_0 is the intrinsic capacitance of a planar coil, ε is the permittivity of liquid nitrogen, S is the effective area of a capacitor formed by the central and side areas of planar coils connected in series. This estimate yields a value on the order of 30 Hz/Å. An experimental value of the capacitor variation rate was about 10 Hz/Å. The rate of the frequency variation being very high, creation of the adjustable filter requires high-precision mechanics driving the substrates.

Characteristics of high-Q resonance circuits on various substrates

Substrate	f_r, MHz	Δf_r, kHz	Q
LaAlO	68.6	5	1.4×10^4
GaNdO	67.1	0.75	89.5×10^4
SrTiO	8.4	3	2.8×10^4

In our system, the Q measurements at small distances between the substrates were hindered by mechanical oscillation. In order to determine the low-frequency Q, we used a nonadjustable circuit composed of two planar coils separated by a pure NdGaO substrate with a thickness of $d = 0.5$ mm. The quality factor of this circuit was 68000 at a resonance frequency of 6.88 MHz.

REFERENCES

1. F. S. Thomson, R. R. Mansour, S. Ye, *et al.*, IEEE Trans. Appl. Supercond. **8** (2), 85 (1998).
2. M. Rolfes, Superconductor Industry, 24 (Winter 1995).
3. G.-C. Liang, D. Zhang, C.-F. Shih, *et al.*, IEEE Trans. Appl. Supercond. **5** (2), 2652 (1995).
4. L. I. Ponomarev, A. Yu. Ganitsev, V. V. Parshikov, *et al.*, Antenny, No. 3 (2000).
5. L. I. Ponomarev and A. Yu. Ganitsev, Antenny, No. 1 (40) (1998).
6. R. S. Withers, G.-C. Liang, B. F. Cole, *et al.*, IEEE Trans. Appl. Supercond. **3** (1), 2450 (1993).
7. Erzhen Gao, Shapur Sahba, Hui Xu, *et al.*, IEEE Trans. Appl. Supercond. **9** (2), 3066 (1999).
8. E. A. Vopilkin, S. A. Pavlov, A. N. Panin, *et al.*, Pis'ma Zh. Tekh. Fiz. **26** (8), 83 (2000) [Tech. Phys. Lett. **26**, 352 (2000)].

Translated by P. Pozdeev